UNIVERSITÉ LAVAL

Probability of detection analysis for infrared nondestructive testing and evaluation with applications including a comparison with ultrasonic testing

Thèse

Yuxia Duan

Doctorat en génie électrique
Philosophiae doctor (Ph. D.)

Québec, Canada

Résumé

La fiabilité d'une technique d’Évaluation Non-Destructive (END) est l'un des aspects les plus importants dans la procédure globale de contrôle industriel. La courbe de la Probabilité de Détection (PdD) est la mesure quantitative de la fiabilité acceptée en END. Celle-ci est habituellement exprimée en fonction de la taille du défaut.

Chaque expérience de fiabilité en END devrait être bien conçue pour obtenir l'ensemble de données avec une source valide, y compris la technique de Thermographie Infrarouge (TI). La gamme des valeurs du rapport de l'aspect de défaut (Dimension / profondeur) est conçue selon nos expériences expérimentales afin d’assurer qu’elle vient du rapport d’aspect non détectable jusqu’à celui-ci soit détectable au minimum et plus large ensuite. Un test préliminaire est mis en œuvre pour choisir les meilleurs paramètres de contrôle, telles que l'énergie de chauffage, le temps d'acquisition et la fréquence. Pendant le processus de traitement des images et des données, plusieurs paramètres importants influent les résultats obtenus et sont également décrits.

Pour la TI active, il existe diverses sources de chauffage (optique ou ultrason), des formes différentes de chauffage (pulsé ou modulé, ainsi que des méthodes différentes de traitement des données. Diverses approches de chauffage et de traitement des données produisent des résultats d'inspection divers. Dans cette recherche, les techniques de Thermographie Pulsée (TP) et Thermographie Modulée(TM) seront impliquées dans l'analyse de PdD. Pour la TP, des courbes PdD selon différentes méthodes de traitement de données sont comparées, y compris la Transformation de Fourier, la Reconstruction du Signal thermique, la Transformation en Ondelettes, le Contraste Absolu Différentiel et les Composantes Principales en Thermographie. Des études systématiques sur l'analyse PdD pour la technique de TI sont effectuées. Par ailleurs, les courbes de PdD en TI sont comparées avec celles obtenues par d'autres approches traditionnelles d’END.

Abstract

The reliability of a Non-Destructive Testing and Evaluation (NDT&E) technique is one of the most important aspects of the overall industrial inspection procedure. The Probability of Detection (PoD) curve is the accepted quantitative measure of the NDT&E reliability, which is usually expressed as a function of flaw size.

Every reliability experiment of the NDT&E system must be well designed to obtain a valid source data set, including the infrared thermography (IRT) technique. The range of defect aspect ratio (Dimension / depth) values is designed according to our experimental experiences to make sure it is from non-detectable to minimum detectable aspect ratio and larger. A preliminary test will be implemented to choose the best inspection parameters, such as heating energy, the acquisition time and frequency. In the data and image processing procedure, several important parameters which influence the results obtained are also described.

For active IRT, there are different heating sources (optical or ultrasound), heating forms (pulsed or lock-in) and also data processing methods. Distinct heating and data processing manipulations produce different inspection results. In this research, both optical Pulsed Thermography (PT) and Lock-in Thermography (LT) techniques will be involved in the PoD analysis. For PT, PoD curves of different data processing methods are compared, including Fourier Transform (FT), 1st Derivative (1st D) after Thermal Signal Reconstruction (TSR), Wavelet Transform (WT), Differential Absolute Contrast (DAC), and Principal Component Thermography (PCT). Systematic studies on PoD analysis for IRT technique are carried out. Additionally, constructed PoD curves of IRT technique are compared with those obtained by other traditional NDT&E approaches.

Table of Contents

List of Tables

List of Figures

List of Acronyms

AANC	Airworthiness Assurance Nondestructive Inspection Validation Center
CFRP	Carbon Fiber Reinforced Polymer
CFT	Continuous Fourier Transform
CNR	Contrast Noise Ratio
DAC	Differential Absolute Contrast
DFT	Discrete Fourier Transform
EOFs	Empirical Orthogonal Functions
ET	Eddy-current Testing
FBH	Flat-Bottom Holes
FFT	Fast Fourier Transform
FPI	Fluorescent Penetrant Inspection
FT	Fourier Transform
GLM	Generalized Linear Model
IRT	Infrared Thermography
LSE	Least Squares Estimation
LT	Lock-in Thermography
MIVIM	Multipolar Infrared Vision – Vision Infrarouge Multipolaire
MLE	Maximum Likelihood Estimates
MPI	Magnetic Particle Inspection
MT	Modulated Thermography
NDI	Nondestructive Inspection
NDT&E	Nondestructive Testing and Evaluation
PCA	Principal Component Analysis
PCs	Principal Components
PCT	Principal Component Thermography
PoD	Probability of Detection

PPT	Pulsed Phase Thermography
PT	Pulsed Thermography
RIM	Range Interval Method
RT	Radiographic Testing
SNR	Signal Noise Ratio
SVD	Singular Value Decomposition
TSR	Thermographic Signal Reconstruction
UT	Ultrasonic Testing
VT	Vibrothermography
WAN	Wallonie Aeronautics Network
WT	Wavelet Transform

Acknowledgements

The last four years have personally been a wonderful learning experience for many reasons and due to many people to whom I owe many thanks.

First of all, I would like to begin by thanking my supervisor Prof. Xavier Maldague. I really appreciate his guidance, encouragement and constant support during my Ph.D. research. I want to thank the members of my thesis committee, Prof. Hakim Bendada, Prof. Cunlin Zhang, and Mr. Marc Genest for taking time in their busy schedule to read this thesis and give me helpful comments.

I would also like to thank all the members of the Laboratory of Computer Vision and Systems, who spread a very friendly atmosphere. I particularly would like to thank Dr. Clemente Ibarra Castanedo for all the helps in my experiments and being patient to discuss about my project.

There was also much help from my friends in Quebec City for which I am grateful. I thank all my friends here, my old friends, and my classmates for filling my life with happiness. All of you have made my stay in Université Laval a happy and invaluable experience in my life.

Since the day I was born I have many reasons to thank my parents. They have given me so much love, supports, encouragements and good wishes.

I thank my husband Jianqiao Meng for all his patience and encouragements. At last, I want to thank our daughter Lingfei Meng, who just arrived this world, for the joy she brings to me.

Introduction

BACKGROUND

For a Nondestructive Testing and Evaluation (NDT&E) method, ideally, defects larger than a certain size can be detected. However, in the real NDT&E process, the situation is more complex. Different flaws of the nominal same size can produce different magnitudes of stimulus response because of the differences in physical properties of the specimens or/and flaws. Repeated inspections of a specific flaw can also produce different response magnitudes because of minute variations in setup and calibration. This variability is inherent in NDT&E process [1]. Furthermore, the interpretation of the response can be influenced by the capability and mental acuity of the inspectors. All these factors contribute to inspection uncertainty and lead to a probabilistic characterization of NDT&E inspection capability and reliability [1].

Probability of Detection (PoD) analysis as a quantitative measure to evaluate the inspection reliability[1] of a NDT&E technique has been established for decades [2, 3]. It is widely used in the traditional NDT&E techniques [1-4], including Ultrasonic Testing (UT), Radiographic Testing (RT), Eddy-current Testing (ET), Fluorescent Penetrant Inspection (FPI) and Magnetic Particle Inspection (MPI). Most of the pioneering work about PoD function which has been expressed as a function of flaw size, for describing the reliability of a NDT&E system, has been carried out in the aerospace industry [5]. In order to ensure the structural integrity of critical components, it was becoming evident that instead of asking the question “What is the smallest flaw that can be detected by a NDT&E method?” it was more appropriate, from a fracture mechanics point of view, to ask “What is the largest flaw that can be missed?”, as there are many flaws larger than the smallest detected that might be missed, thus leading to structure failures [6]. So the main objective of a NDT&E reliability demonstration is to determine the largest flaw that the NDT&E system can miss [7].

---

[1] NDT&E inspection reliability is defined as: “The probability of detecting a flaw in a given size group under the inspection conditions and specified procedures.”

Infrared Thermography (IRT) for NDT&E is a non-invasive and fast inspection technique with the capability to perform remote inspections on large surfaces [8]. Nowadays, IRT has been used as a stand-alone NDT&E method with respect to other NDT&E approaches, especially for the inspection of aircraft composite structures. Recent international NDT&E standards NAS410 (revision 2008) and EN4179 Edition 4, both depict IRT apart from traditional NDT&E techniques [5]. Surprisingly, contrary to traditional NDT&E techniques such as UT and ET for which a significant amount of reliability research has been carried out, a rather limited number of studies on reliability assessment involving active thermography have been published so far [5, 9-14]. Most of previous work about PoD analysis for IRT is carried out by Airworthiness Assurance Nondestructive Inspection Validation Center (AANC) of Sandia National Laboratories. Wayne State University and Marshall Space Flight Center also did some related works. In their studies, bust sonic IRT and optical pulsed IRT are involved. However, there is no systematic study on the PoD analysis for IRT technique. Now is really the time to comprehensively research the reliability and capability of IRT nondestructive inspection systems.

The thesis is based on previous research activities carried out at the Multipolar Infrared Vision – Vision Infrarouge Multipolaire (MIVIM) Canada Research Chair in the field of IRT NDT&E technique. The experiences from PoD analysis of traditional NDT&E techniques are also a good basis for the project. However, some challenges remain to be faced. For response data, it has become a common practice to use ln (â) vs. ln (a) PoD model in the traditional NDT&E reliability demonstration, especially for flaw length as determined by UT. However, our studies show that sometimes Cartesian â vs. ln (a) is a better PoD model for our obtained data set. Generally, in this research, the PoD model is chosen according to the data set rather than experiences, because most of the experiences mentioned in the literature are from PoD analysis of traditional NDT&E methods. As a statistic method, a PoD analysis often requires a large set of sampling data with appropriate distribution over the selected testing range in order to achieve reasonable precision. So the first challenge of the project is that a very large number of samples and detected targets (flaws) are needed. The second challenge is that PoD curve are sensitive to the equipment, experimental parameter setting, post data processing and even the capability of inspector. In order to get a reasonable evaluation of an infrared NDT&E system, all these factors have to be considered to obtain a valid data set.

RESEARCH OBJECTIVES

The main objective of the research is to quantitatively evaluate the inspection reliability and capability for IRT NDT&E technique. The obtained PoD curves will be compared with traditional NDT&E methods, such as ultrasonic C-scanning.

This research will advance the wide acceptation of IRT NDT&E out of laboratory, especially in the aerospace industry, since the reliability and capability of IRT NDT&E system is quantitatively evaluated, as traditional NDT&E approaches. Moreover, NDT&E reliability experiments can also be conducted to optimize a NDT&E system or an inspection procedure. PoD curves obtained from different IRT systems and experimental procedures will help us choose excitation sources (or modes), optimize parameter settings in experiments and the post data processes for a specific inspection object.

ORGNIZATION

The thesis is organized into 7 chapters. As we know, there are different heating sources, excitation forms and data processing methods in infrared thermography techniques. For a set of specimens with specific flaw characteristics, distinct heating and data processing manipulations produce obvious different inspection results. In Chapter 1, three classical active thermographic techniques: optical Pulsed Thermography (PT), optical Lock-in Thermography (LT) and vibrothermography (VT) are reviewed. For optical PT, the common and recently developed data analyzing and processing methods, including Fourier Transform (FT), 1st derivative after Thermal Signal Reconstruction (TSR), Wavelet Transform (WT), Differential Absolute Contrast (DAC), and Principal Component Thermography (PCT) are discussed in detail, since they are of interest for the research.

Chapter 2 describes the PoD analysis methods from response data and hit/miss data. The fundamental concepts such as parameter estimation, confidence bound, false positives (false alarms) are then discussed.

Based on the discussion of Chapter 2, Chapter 3 concentrate on describing the experimental design to obtain valid source data set and the detailed procedures to obtain PoD curves and corresponding confidence bounds of IRT system from response data and hit/miss data.

In Chapter 4, PoD analysis of both continuous response data and hit/miss data are carried out based on the optical PT inspection results of a Carbon Fiber Reinforced Polymer (CFRP) specimen with embedded material simulating delaminations. The effect of various PT data processing methods, including FT, TSR, WT, DAC, and PCT on PoD curves is compared.

In Chapter 5, for a set of aluminum foam material, PoD curves are plotted in order to quantitatively evaluate the two optical thermographic techniques: LT and PT in this application.

PoD analysis results by UT and PT for impact damage of CFRP are presented in Chapter 6. The quantitative comparison shows that PT has higher inspection reliability than UT.

In Chapter 7, a method to extract defects automatically by image segmentation is presented. The PoD curves of manual evaluation and automated segmentation results are compared. False alarm which is an important aspect of reliability evaluation is studied in this chapter.

Chapter 1. A Review of Infrared Thermography for NDT&E

In this chapter, we will review the modern IRT techniques for NDT&E and related data processing methods proposed in the literature.

1.1. Infrared Thermography for NDT&E

The basic approach of the modern thermography for NDT&E is to thermally excite an object by heating (or cooling) it while using an infrared camera to monitor changes of the object's surface temperature. Since subsurface discontinuities may alter the diffusion of the heat, this will affect the cooling behavior of the nearby region on the surface.

Practically any energy source can be used for stimulation purposes, from cold/hot air to optical source, to mechanical oscillations, to eddy current [15]. There are also different heating forms and patterns. Modulated and pulsed heating are among the most popular heating forms. Step heating (SH) is also found in the literature, often referred to as a long pulse excitation [16].

There are three classical active thermographic techniques based on modulated and pulsed excitation modes [17]: optical PT and LT, which are optical techniques applied externally, i.e. the energy is delivered to the surface of the specimen where the light is transformed into heat; and vibrothermography, which uses sonic or ultrasonic waves (pulsed or modulated) to excite surface or subsurface defects internally. In UT the mechanical oscillations injected into the specimen travel in all directions dissipating their energy at the discontinuities in the form of heat, which travels to the surface by conduction. In practice, excitation modes should be chosen according to the physical properties of the specimen and the defect characteristics. These three classical active thermographic techniques are described in details in the next sections.

Practical inspections often require strict capabilities in terms of high Signal Noise Ratio (SNR). As a result, additional processing of the data from the camera is required. Common and recently developed data analyzing and processing methods, especially in PT whose raw data is difficult to handle and analyze because of non-uniform heating and reflection, will be discussed in the following sections.

1.2. Optical Pulsed Thermography (PT)

In optical PT, the specimen surface is submitted to a short heat pulse using a high power optical source. The duration of the pulse may vary from a few ms (~2-15 ms) to several seconds. Absorption of short time pulse energy elevates the specimen surface temperature. As time elapses and heating pulse vanishes, the surface temperature decreases uniformly for a piece without internal flaws. On the contrary, subsurface discontinuities (e.g. porosity, delaminations, disbonds, fiber breakage, inclusions, etc.) change the diffusion of heat flow and produce abnormal temperature patterns at the surface that can be detected with an IR camera, as shown in figure 1.1.

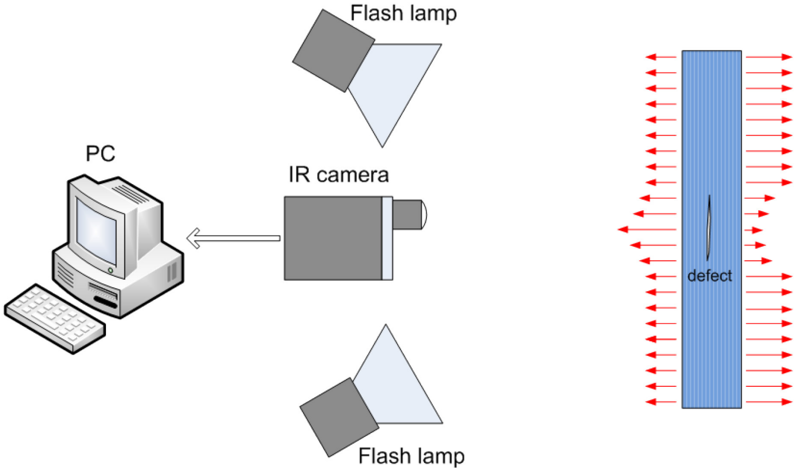

Figure 1. 1. Schematic setup of PT (Reflection Mode).

The specimen is heated from one side while thermal data is collected either from the same side, i.e. reflection mode; or from the opposite side, i.e. transmission mode. Reflection is used when inspecting defects closer to the heated surface, whilst transmission is preferred for detecting defects closer to the non-heated surface (i.e. deeper defects). In general, resolution is higher in reflection and it is easier to deploy given that both sides of the specimen do not need to be accessible. Although deeper defects can be detected in transmission, depth information is lost since thermal waves will travel the same distance whether their strength is reduced by the presence of a defect or not [15].

The Fourier's Law one-dimensional solution for a Dirac delta pulse propagating through a semi-infinite homogeneous material is given by [18]:

$$T(z,t) = T_0 + \frac{Q}{\sqrt{\kappa \rho c \pi t}} \exp\left(-\frac{z^2}{4\alpha t}\right) \tag{1.1}$$

where Q is the energy absorbed by the surface; T_0 is the initial temperature; κ is the thermal conductivity; ρ is the product of density; c is the specific heat; and α is the thermal diffusivity.

Considering the temperature evolution of the inspected surface with time increasing, Eq. (1.1) can be rewritten as (z = 0):

$$T(0,t) = T_0 + \frac{Q}{e\sqrt{\pi \cdot t}} \tag{1.2}$$

where $e = \sqrt{\kappa \rho c}$ is the effusivity, which is a thermal property that measures the material ability to exchange heat with its surroundings.

Data acquisition in PT is fast and allows the inspection of wide area surfaces. However, raw PT data is difficult to handle and analyze because of non-uniform heating or reflections. There are a great variety of processing techniques that have been developed to improve the inspection results. The common and recently developed data analyzing and processing methods will be discussed in detail next.

1.2.1. Fourier Transform (FT)

FT is particularly interesting among the data processing methods since it allows retrieving phase and amplitude data from a PT experiment, which can be thought as being a combination of PT and LT. Analyzing phase data obtained from FT to get improved inspection results in PT is known as Pulsed Phase Thermography (PPT) in the literature [19].

It is well-known that any wave form, periodic or not, can be approximated by the sum of purely harmonic waves oscillating at different frequencies. The Continuous Fourier Transform (CFT) can be expressed as:

$$F(\omega) = \int_{-\infty}^{+\infty} f(t)\, e^{-j\omega t} dt = A(\omega) e^{i\varphi(\omega)} \tag{1.3}$$

where $\omega = 2\pi f$, the FT can be seen as a technique to transform our perception of the signal from a time-based to a frequency-based perspective.

For PPT, the Discrete Fourier Transform (DFT) is used working with sampled signals of PT data [19-22]:

$$F_n = \Delta t \sum_{k=0}^{N-1} T(k\Delta t) e^{-j2\pi nk/N} = \mathrm{Re}_n + \mathrm{Im}_n \tag{1.4}$$

where n designates the frequency increment ($n = 0, 1, \cdots, N$); Δt is the sampling interval; N is the total number of thermograms (infrared images); and Re and Im are the real and the imaginary parts of the transform, respectively.

It should be noted that the sampling interval Δt, is introduced in Eq. (1.4) as a scale factor in order to produce equivalency between CFT and DFT [21]. For NDT applications, Eq. (1.4) is not practical due to lengthy computations. The Fast Fourier Transform (FFT) algorithm [23], available in software packages such as MatLab®, greatly reduces the computation time and is therefore privileged.

From Eq. (1.4), modulus or amplitude A_n, and phase delay ϕ_n, discrete values are available as follows:

$$A_n = \sqrt{\mathrm{Re}_n^2 + \mathrm{Im}_n^2}\,, \qquad \phi_n = \tan^{-1}\left(\frac{\mathrm{Im}_n}{\mathrm{Re}_n}\right) \tag{1.5}$$

By applying FFT on every pixel of the thermogram sequence, the amplitude and phase images of different frequencies will be obtained. However, amplitude images are rarely used in PPT since phase images are more tolerant to non-uniform heating, emissivity variations, surface geometry and reflections from the environment compared to amplitude images [24]. Figure 1.2 shows temperature and phase delay profiles for a defect area and defect free (sound) area.

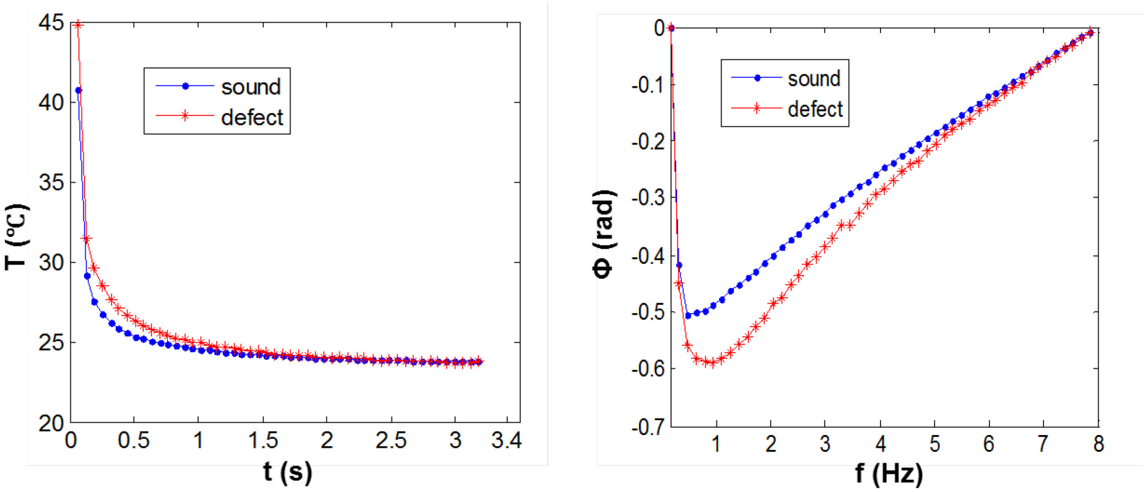

Figure 1. 2. Temperature and phase delay profiles for a defect of 0.2mm depth and 5mm diameter (red line) and sound area (blue line). Data is from a CFRP specimen.

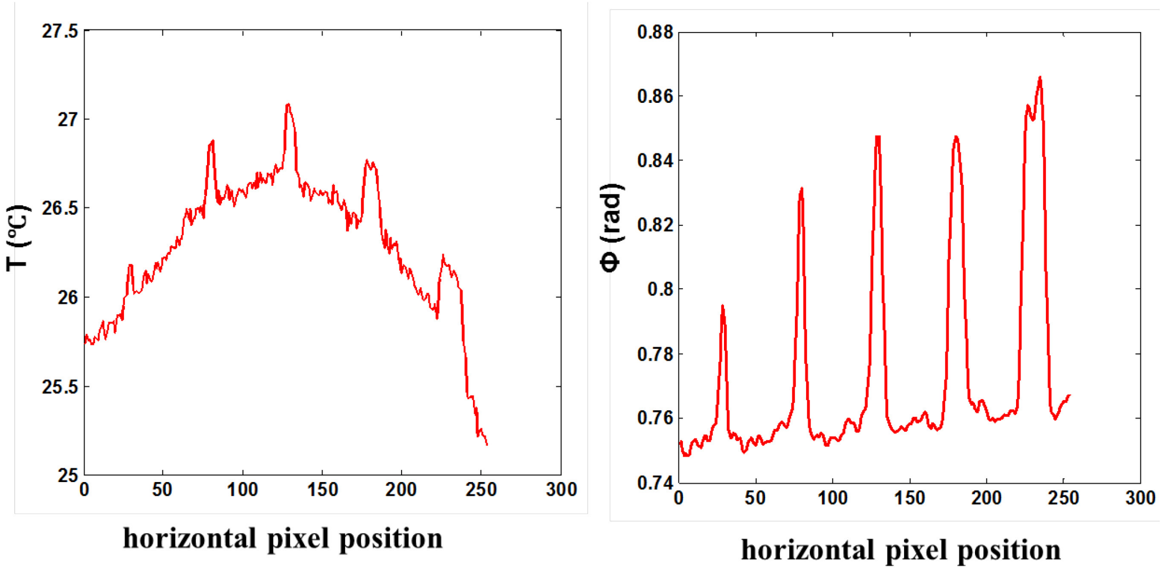

Figure 1. 3. Comparison of raw (left) and phase delay (right) results for a horizontal line through the center row of defects (depth = 0.4mm, different diameters from 3mm to 15mm) in the same CFRP specimen as in figure 1.2.

The ability of a human operator to perceive a defect in an image is related to the signal to background contrast and signal to noise ratio for a certain defect. Figure 1.3 shows a comparison of raw (left) and phase delay (right) results for a horizontal line through the center row of defects (depth = 0.4mm, different diameters from

3mm to 15mm) in a CFRP specimen. As we previously discussed, the non-uniform heating effects and noises (high frequency component) are significantly reduced in phase delay profiles as compared to raw profiles. Besides, the smallest (diameter = 3mm) defect can only be detected by phase data.

In order to obtain the optimum result, two important parameters: sampling rate (f_s), and the acquisition time (t_{acq}), i.e. the maximum truncation window ($w(t)$) need to be determined. Theoretically, the sampling rate should be high enough to increase the available frequency which is given by half the sampling rate $f_{max} = f_s/2$, and capture early thermal changes. The truncation window should be as large as possible to increase frequency resolution and to be able to characterize a wide range of depths, especially deep defects that are detectable only at very low frequencies. However, in practice a compromise have to made between frame rate, acquisition time and storage capacity (N_{max}). It is more convenient to sacrifice time resolution instead of decreasing the size of $w(t)$ to cover a wider range of depths without compromising too much defect detectability. This will guarantee that most defects, deep and shallow, will be detected even if it might not be possible to quantify them at this point. However, there is no advantage in extending the size of $w(t)$ beyond the stabilization time, i.e. when thermal changes are no longer significant. Only significant variations in time domain are of interest on the frequency spectra following the FT. The details about parameters determination in PPT experience can be found in references [25, 26].

The choice of the thermal pulse duration also affects the results. The longer the pulse in the time domain, the more high frequency components are suppressed and the energy is concentrated in the low frequencies (figure 1.4). If defects very near the surface are to be observed, a much shorter heat pulse must be used to keep the high frequency signal components (which however implies the practical problem of depositing enough energy in a very short time to cause a measurable temperature contrast) [27].

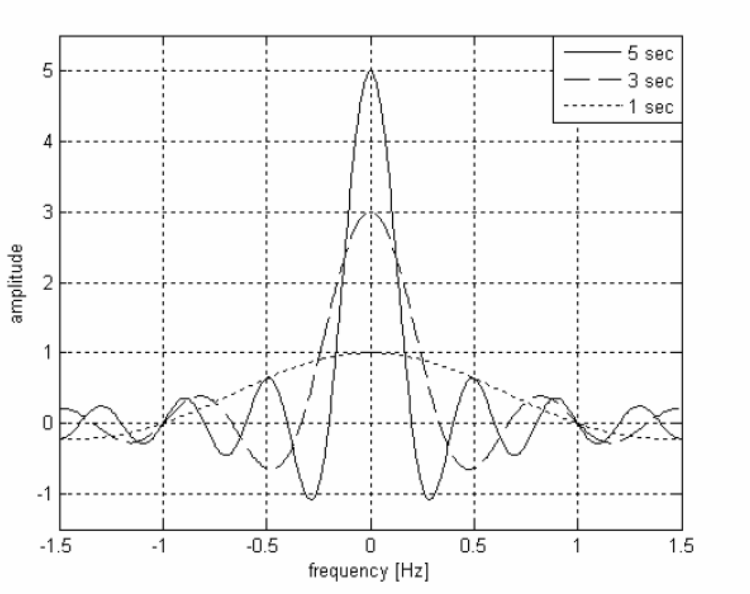

Figure 1. 4. Influence of pulse duration on frequency spectrum [27].

1.2.2. 1st Derivative after Thermographic Signal Reconstruction (TSR)

1st Derivative after TSR is another very useful PT processing technique, which provides a significant improvement in SNR performance as well as enabling a good sensitivity to smaller and deeper defects [28].

As previously discussed (Eq. 1.2), the surface temperature decreases based on one-dimensional solution of the Fourier equation for a Dirac delta function in a semi-infinite isotropic solid can be rewritten as [29]:

$$\Delta T = T(0,t) - T_0 = \frac{Q}{e\sqrt{\pi t}} \tag{1.6}$$

Eq. (1.6) in logarithmic domain can be expressed by:

$$\ln(\Delta T) = \ln\left(\frac{Q}{e}\right) - \frac{1}{2}\ln(\pi t) \tag{1.7}$$

which corresponds to a straight line with slope –0.5 in a log-log scale (figure 1.5).

The one-dimensional approximation recognizes that heat diffuses in all directions, but assumes that the lateral diffusion components more or less cancel in a defect free sample. However, in the presence of an adiabatic subsurface boundary such as a void or a wall, the incident heat flow from the sample surface is impeded, and the one-dimensional description no longer applies locally. In effect, defect detection in PT can be thought of as identification of areas where the one-dimensional assumption breaks down [29-31].

In practice, logarithmic data may vary from ideal one-dimensional behavior for a variety of reasons (e.g. material inhomogeneities, nonlinear camera response or background radiation contributions). Nevertheless, the logarithmic behavior exhibits remarkable consistency, in that pixels representing defect free areas are nearly linear, and pixels corresponding to subsurface defects depart from the near-linear signature at a particular time that is correlated to the depth of the defect [29-31]. Figure 1.5 shows ln(ΔT) dependence of ln(t) for a sound and defect areas. In the log plot, the defect deviates from straight line with slope –0.5 at a particular time (break point).

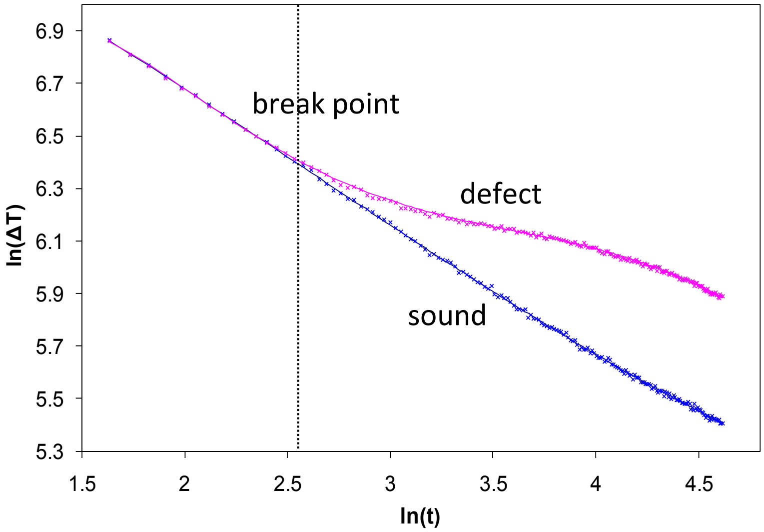

Figure 1. 5. Ln(ΔT) dependence of ln(t) for a sound (blue)and defect areas (red).

A low order expansion is applied on Eq. (1.7) in order to serve as low pass filter that preserves the essential thermal response. In the logarithmic domain, the inclusion of higher orders only replicates noise. It has been found that a 4th (or 5th order) polynomial provides an excellent fit to PT data, which is given as:

$$\ln(\Delta T) = a_0 + a_1 \ln(t) + a_2[\ln(t)]^2 + a_3[\ln(t)]^3 + a_4[\ln(t)]^4 \tag{1.8}$$

With the temperature decrease of each pixel approximated by Eq. (1.7) (or a similar expansion), we can reconstruct the original data:

$$\Delta T = \exp\{a_0 + a_1 \ln(t) + a_2[\ln(t)]^2 + a_3[\ln(t)]^3 + a_4[\ln(t)]^4\} \tag{1.9}$$

If the entire sequence of TSR images is to be stored, it is only necessary to save the polynomial coefficients, regardless of the length of the image sequence. As a result, the TSR method provides a significant degree of data compression. It is also convenient for generating derivative images without additional noise contributions. For each pixel, the time sequence can be differentiated using expression:

1st Derivative: $$\frac{d\ln(\Delta T)}{d\ln(t)} = \sum_{n=0}^{N} n a_n \ln(t)^{n-1} \tag{1.10}$$

2nd Derivative: $$\frac{d^2\ln(\Delta T)}{d\ln(t)^2} = \sum_{n=0}^{N} n(n-1) a_n \ln(t)^{n-2} \tag{1.11}$$

Figure 1.6 shows the comparison of ln(*ΔT*) - ln(*t*) and the corresponding 1st and 2nd derivatives [29]. The initial separation of the sound (blue) and defect (gray) temperature signals is difficult to discriminate in the logarithmic temperature-time plot (left). However, the separation is enhanced in the 1st (center) and 2nd (right) derivatives.

As we previously discussed, the 1st D of TSR process effectively removes temporal noise from the defect signal, so that signal to noise improvement is gained through noise reduction. However, the signal to background contrast is not dramatically improved by the process. In fact, removal of noise components may cause an apparent reduction in signal to background contrast. Far more significant gain in signal to background contrast is obtained when images based on the time derivatives of the TSR signal are considered, as shown in figure 1.7. The derivatives are much more sensitive to small changes in amplitude than the raw signal. However, the low pass filtering action of the TSR process makes them relatively immune to random signal fluctuations [29-31].

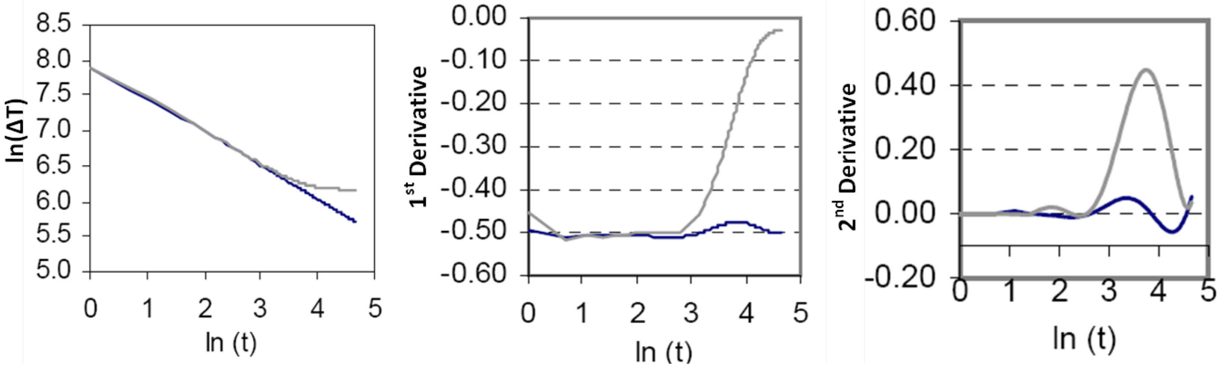

Figure 1. 6. Comparison of ln(ΔT) - ln(t) and the corresponding 1st (center) and 2nd (right) derivatives for sound (blue) and defective (grey) area [29].

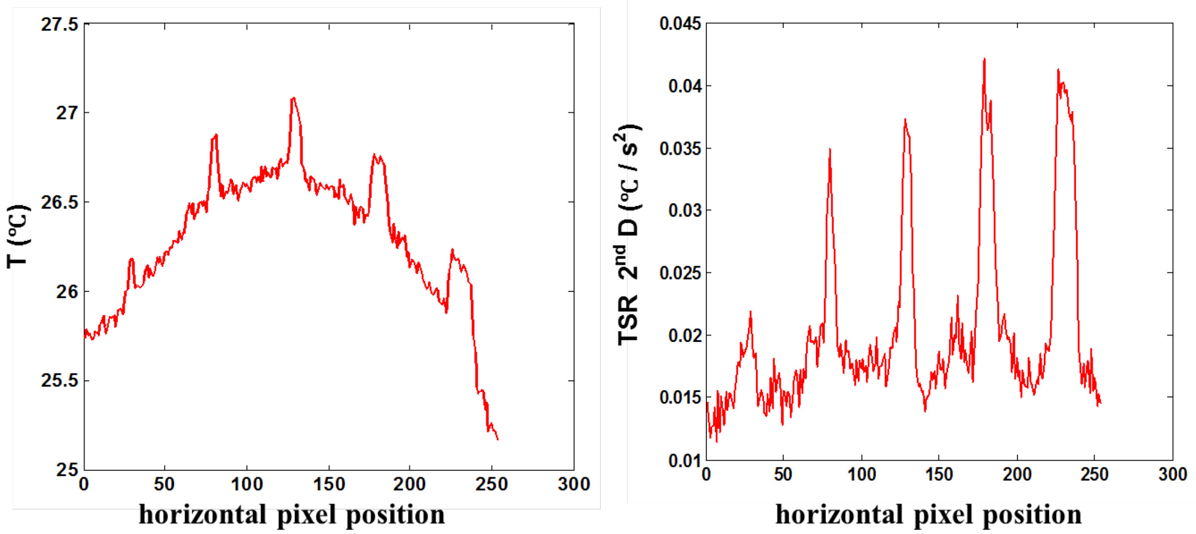

Figure 1. 7. Comparison of raw (left) and TSR 2nd derivative (right) results for a horizontal line through the center row of defects (depth = 0.4mm) in the aforementioned CFRP sample.

The selection of experimental parameters is more intuitive than for PPT: For high conductivity materials and shallow defects choose high sampling frequency and short acquisition time since the time evolution of the surface temperature changes rapidly; for low conductivity materials and deep defects choose low sampling frequency and long acquisition time since the time evolution of the surface temperature changes slowly.

1.2.3. Wavelet Transform (WT)

From the previous discussion about PPT, we can see that, although the inspection results improved considerably by using the FT, the time information, i.e. direct defect depth information is lost (in first approximation the sub-surface defect depth is proportional to the square root of time [32]). In this situation, the blind frequency method is proposed and it is discussed in details in [25]. However, the main problem of using PPT data for defect depth measurement is that two or three experiments may be needed if the range of defect depth is wide, since requirements of experimental parameters are stricter for the purpose of quantitative evaluation.

WT can be seen as an extent of FT since it preserves the time information lost in FT which is directly correlated to the defect depth, while maintaining FT advantageous features. In wavelet analysis, a fully scalable modulated window is used instead of the fixed truncation window used in FT. The window is shifted along the signal and for every position, the spectrum is calculated. Then, this process is repeated many times with a slightly shorter (or longer) window for every new cycle. At the end, the result will be a collection of time-frequency representations of the signal, all with different resolutions [33].

The continuous WT (CWT) is defined as [33]:

$$CWT(s,\tau) = \int_{-\infty}^{+\infty} f(t) \cdot \psi_{s,\tau}{}^{*}(t)dt \qquad (1.12)$$

where $*$ denotes complex conjugation. This equation shows how a function $f(t)$ is decomposed into a set of basic functions $\psi_{s,\tau}(t)$, called the wavelets. The variables s and τ, scale and translation, are the new dimensions after the WT.

The wavelets are generated from a single basic wavelet $\psi(t)$, the so-called mother wavelet, by scaling and translation [33]:

$$\psi_{s,\tau}(t) = \frac{1}{\sqrt{s}} \psi\left(\frac{t-\tau}{s}\right) \qquad (1.13)$$

where $1/\sqrt{s}$ factor is for energy normalization across the different scales.

Complex Morlet wavelet is recommended in reference [34], because it allows not only an excellent qualitative analysis, but also a satisfying quantitative analysis of the depth for the defects observed. The complex Morlet wavelet is defined by [35]:

$$\psi(x) = \sqrt{f_b \pi} e^{i 2\pi f_c x} e^{\frac{x^2}{f_b}} \tag{1.14}$$

where f_c is wavelet center frequency, f_b is bandwidth parameter. The Morlet wavelet is a complex sinusoid within a Gaussian envelope, where the central frequency f_c determines the number of significant oscillations of the complex sinusoid within the Gaussian window [27]. As the mother wavelet can be scaled, a very fine ‘tuning’ of the frequency (or better, ‘pseudo’-frequency) is possible. The relation between the wavelet scale *s* and a pseudo-frequency f_a can be established by the following formula [35]:

$$f_a = \frac{f_c}{s \cdot \Delta t} \tag{1.15}$$

where Δt is sampling period. By choosing the appropriate wavelet frequencies f_b, f_c and scale s, a band-pass like frequency spectrum can be generated which should match or cover the amplitude spectrum of the expected contrast signals.

The Fourier-approach (blind frequency method) was compared with the wavelet-approach based on simulation or experimental data showing a promising potential of the later for defect depth measurements and material characterization in PT [27, 34, 36, 37].

The WT with complex wavelets providing amplitude and phase information can be used in a similar way as the FT used in PPT. Figure 1.8 [37] shows four phasegrams of different translation factors (correlated to defect depths) obtained by WT for a CFRP specimen with an impact damage.

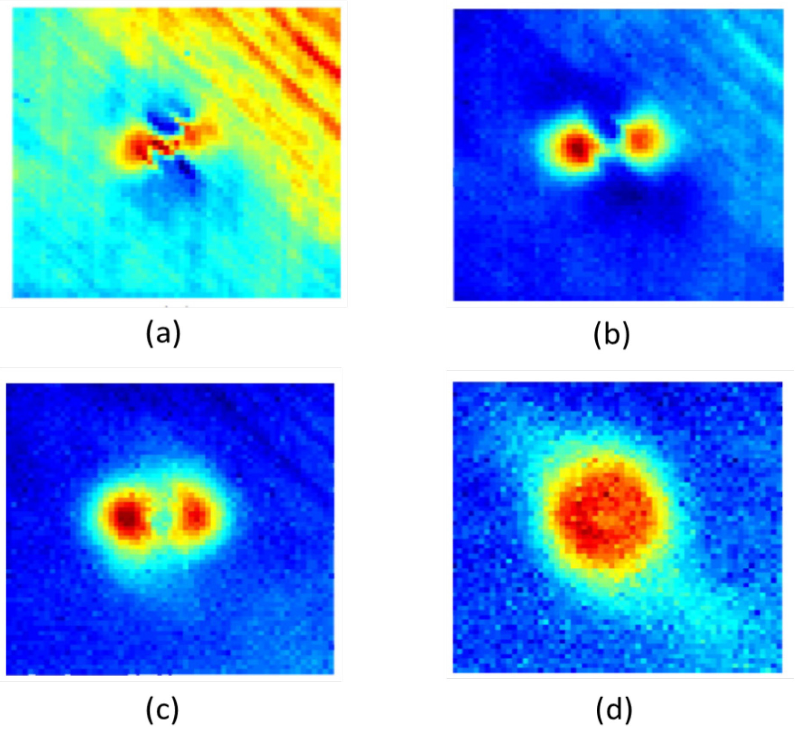

Figure 1. 8. Phasegrams of the WT for four values of translation factor τ: (a) 1.2, (b) 1.8, (c) 2.4, and (d) 3.0 [37].

1.2.4. Differential Absolute Contrast (DAC)

Traditionally, contrast methods require the use of the temperature of a sound area (T_s) where it is known that no defect is present under the surface. The simplest operation called absolute contrast C_a is defined as:

$$C_a(i,j,t) = T_{def}(i,j,t) - T_s(i,j,t) \tag{1.15}$$

where (i,j,t) are the coordinates at time of interest t, and T_{def} is the temperature of a point (i,j), which is known to be located on an area with a defect. Absolute contrast method suffers from two major problems, first the definition of a sound area is not always practical or possible for most industrial applications, and second, the resulting data is strongly affected by non-uniform heating, a problem that is always present at some degrees in thermography NDT&E.

The DAC method has proven effective for managing non-even heating while making local contrast computations [38]. Subjective defect-free-zone definition is no longer necessary. DAC equation is derived from the surface temperature increase based on one-dimensional model of the Fourier equation after an instantaneous Dirac heating pulse is applied, which is given by Eq. (1.6) (see previous discussion):

$$\Delta T = T(0,t) - T_0 = \frac{Q}{e\sqrt{\pi t}}$$

The temperature of the sound area $T_s(i,j)$ at time t' is then given by:

$$\Delta T_s(i,j,t') = \frac{Q(i,j)}{e(i,j)\sqrt{\pi t'}} \tag{1.16}$$

So the surface temperature of the sound area $T_s[i,j]$ at time *t* can be written as:

$$\Delta T_s(i,j,t) = \frac{Q(i,j)}{e(i,j)\sqrt{\pi t}} = \frac{\sqrt{\pi t'}}{\sqrt{\pi t}} \cdot \Delta T_s(i,j,t') = \sqrt{\frac{t'}{t}} \cdot \Delta T(i,j,t') \tag{1.17}$$

where t' is a given value of time ranging from a reference time t_{ref} (see figure 1.9 below), and the time at which the shallowest defect becomes visible t_{def} . Theoretically the surface temperature increase is the same either on defect free or defect area before time t_{def} . So we can perform Eq. (1.17) computations over the entire surface (all locations $[i,j]$) and for the whole temporal sequence) and reconstruct the "ideal" defect free thermogram sequence, which can be expressed as:

$$\Delta T_s(t) = \sqrt{\frac{t'}{t}} \cdot \Delta T(t') \tag{1.18}$$

Considering next that before excitation (the so called cold image) as a surface temperature T_0, then the absolute temperature contrast C_a can be expressed as:

$$C_a(i,j,t) = [T_{def}(i,j,t) - T_0] - [T_s(i,j,t) - T_0] = \Delta T_{def}(i,j,t) - \Delta T_s(i,j,t) \tag{1.19}$$

Finally, the DAC is given as:

$$C_{DAC}(i,j,t) = \Delta T_{def}(i,j,t) - \sqrt{\frac{t'}{t}} \cdot \Delta T(t') \tag{1.20}$$

An appropriate reference time t_{ref}, would be the instant at which heat reaches the surface sample. Nevertheless, as shown on Figure 1.9, this is not known accurately as the heat pulse approximates a square pulse instead of the Dirac pulse assumed. We can reasonably assume though, that t_{ref} is comprised between the beginning and the end of the pulse ($t = 0 < t_{ref} < t_{def}$). In addition, the heat pulse is generally short as compared to the recording time; heat pulse can then be modeled by an instantaneous Dirac pulse [8]. The uncertainty associated with the estimation of t_{ref} forces us to compensate manually or automatically for the error [39].

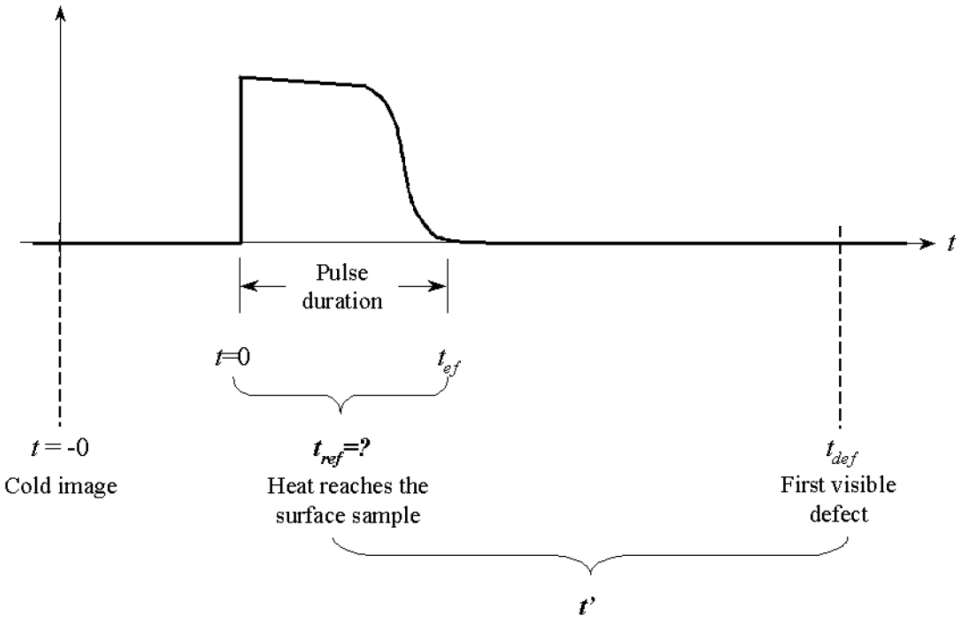

Figure 1. 9. The different times involved on DAC computations are also shown [8].

DAC was applied on a Plexiglas™ sample with 6 holes subjected to a strong non-even heating. The data processing result has proven that DAC is effective against non-uniform heating as is shown in figure 1.10 [39]. Figure 1.10a shows the raw thermogram of a typical sample of Plexiglas™. The corresponding 3D view is seen in figure 1.10b. It is evident from these figures that the sample was subjected to a strong non-even heating as seen on the sharp variation of background intensity values. Figure 1.10c and d, show the thermogram and its 3D view, respectively, after the application of the DAC method. The effect of non-even heating is practically eliminated and defect visibility is strongly enhanced.

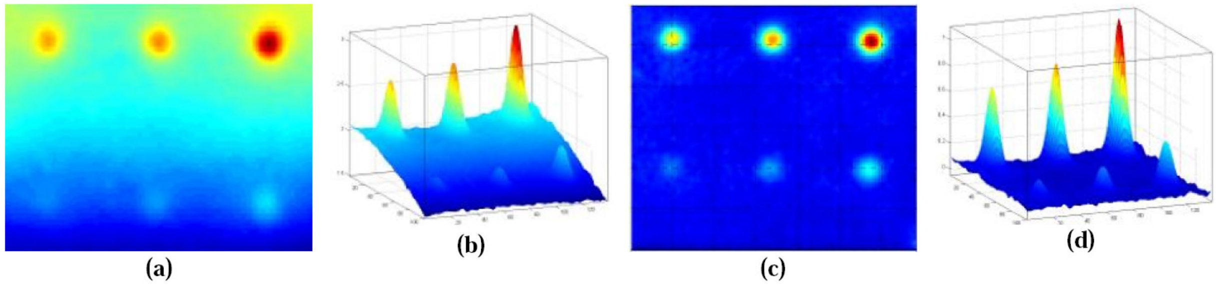

Figure 1. 10. (a) Raw thermogram at 5000 ms, (b) corresponding 3D view, (c) and (d) are the corrected thermogram after the application of DAC method and its corresponding 3D view, respectively [39].

1.2.5. Principal Component Thermography (PCT)

Principal Component Analysis (PCA) used to process thermographic sequences to extract features and reduce redundancy by projecting the thermal response data onto a system of orthogonal components is known as PCT [40].

The PCA is a linear projection technique for converting a matrix ***A*** to a matrix of the lower dimension by projecting ***A*** onto a new set of principal axis. One simple approach to the PCA is to use Singular Value Decomposition (SVD). In general, a matrix ***A*** of the dimension MxN (M＞N) can be decomposed as [41]:

$$\boldsymbol{A} = URV^T \tag{1.21}$$

where U is the eigenvector matrix of the dimension MxN, R is an NxN diagonal matrix with positive or zero elements representing the singular values of matrix ***A***, V^T is the transpose of an NxN matrix.

For PCT, in order to apply the SVD to thermographic data, the 3D thermogram matrix representing time and spatial variations has to be reorganized as a 2D MxN matrix ***A*** [42, 43]. This can be done by rearranging the thermograms for every time as columns in ***A***, as illustrated in Figure 1.11a [43]. Under this configuration, the columns of U represent a set of orthogonal statistical modes known as Empirical Orthogonal Functions (EOFs) that describe the data spatial variations. On the other hand, the Principal Components (PCs), which represent time variations, are arranged row-wise in matrix V^T. The resulting U matrix that provide spatial information can be rearranged as a 3D sequence as illustrated in figure 1.11b [43].

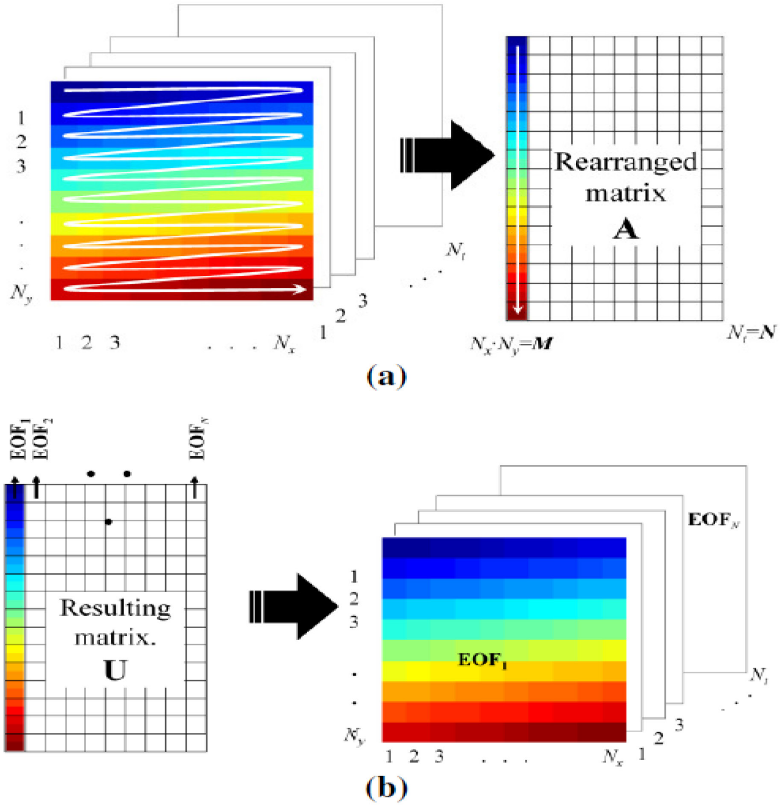

Figure 1. 11. (a) Thermographic data rearrangement from a 3D sequence to a 2D *A* matrix in order to apply SVD; and (b) rearrangement of 2D *U* matrix into a 3D matrix containing the EOFs [43].

Compared with FT that relying on prescribed basis functions (a set of sinusoidal basis functions), PCT method is an eigenvector based transform [41]. It is possible to achieve a compact representation for a complex signal by applying PCT. The first EOF will represent the most characteristic variability of the data; the second EOF will contain the second most important variability, and so on. Usually, 1000 thermogram sequence can be adequately represented with only 10 or less EOFs [42].

Beyond reducing redundancy, PCT is also proposed as a contrast enhancement approach. Experimental verification of PCT approach was carried out on several 50 ply graphite epoxy (Gr–Ep) composite laminate test samples containing circular sections of teflon film embedded at varying depth to simulate delaminations [41]. Figure 1.12 compares the outcomes of PPT, PCT and averaging methods when applied to the raw experimental data. The PPT and PCT methods are noticeably superior to averaging. This is most evident in the case of flaw 4 where averaging fails to yield a convincing flaw indication. Differences between PPT and PCT results are not obvious [41].

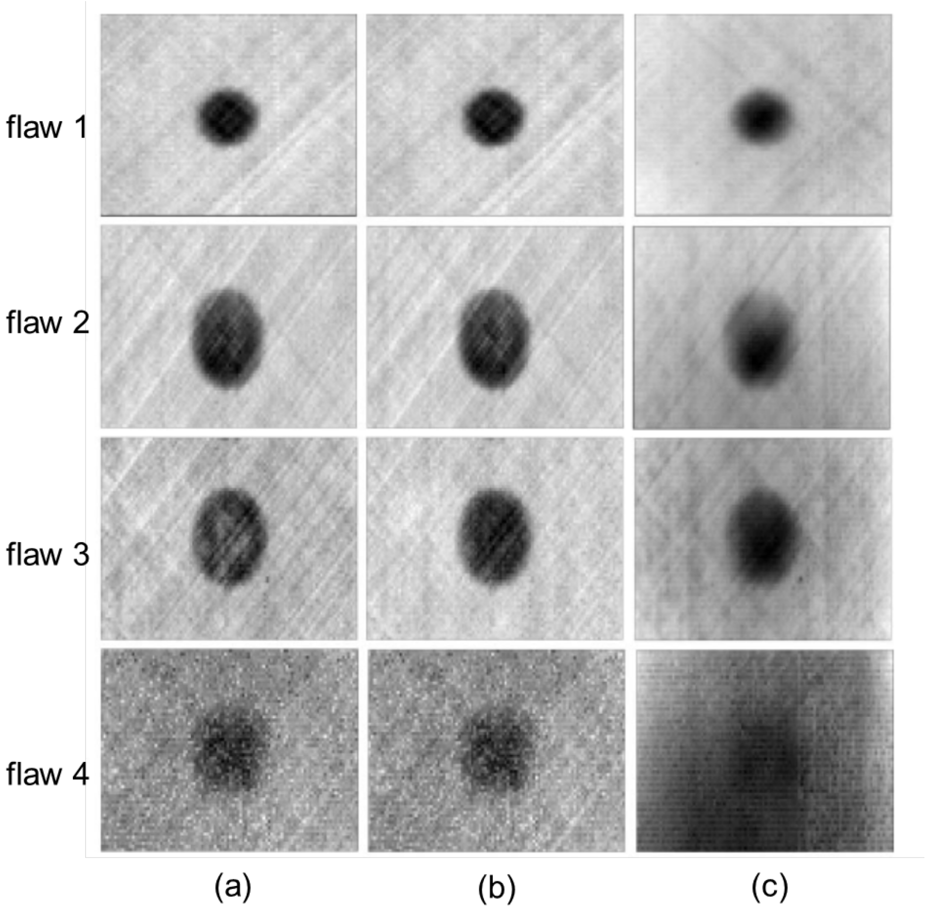

Figure 1. 12. Outcomes of (a) PPT, (b) PCT and (c) averaging methods for 4 flaws with different depths [41].

1.3. Optical Lock-in Thermography (LT)

In optical LT, also known as Modulated Thermography (MT), absorption of modulated optical radiation results in a temperature modulation that propagates as a thermal wave into the inspected component. As the thermal wave is reflected at the defect boundary, its superposition to the original thermal wave causes changes in amplitude and phase of the response signal at the surface, which are recorded at the same time using an infrared camera (figure 1.13) [44].

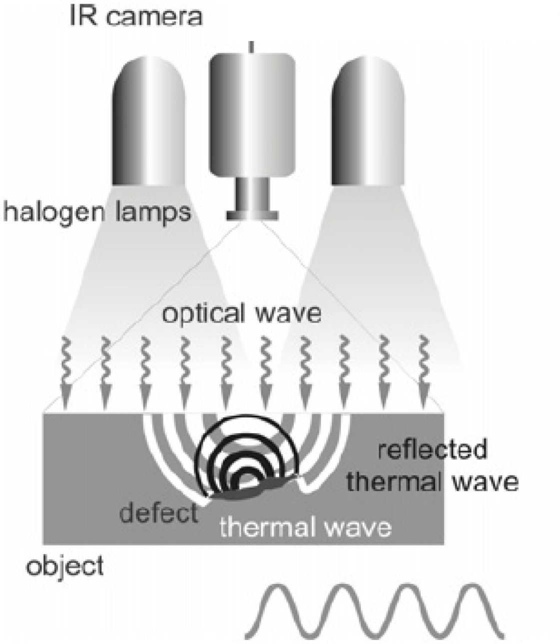

Figure 1. 13. Schematic setup of LT [44].

Sinusoidal waves are commonly used, although other periodic waveforms are possible. Using sinusoids as input has the advantage that the frequency and shape of the response are preserved (i.e. sinusoidal fidelity); only the amplitude and phase of the wave may change [17]. A four point methodology for sinusoidal stimulation can be used to retrieve amplitude and phase [45, 46].

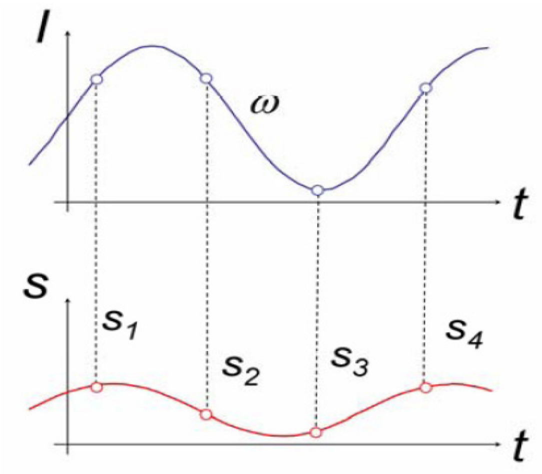

Figure 1. 14. Amplitude and phase retrieval from a sinusoidal thermal excitation [25].

As depicted in figure 1.14, the heating excitation ***I*** have a sinusoidal form, amplitude and phase of response signal ***S*** can be recovered from 4 data points per modulation cycle [34]:

$$A = \sqrt{(S_1 - S_3)^2 + (S_2 - S_4)^2} \tag{1.22}$$

$$\phi = \arctan\left(\frac{S_1 - S_3}{S_2 - S_4}\right) \tag{1.23}$$

where A is the amplitude and ϕ is the phase.

The 4-point methodology is fast but it is valid only for sinusoidal stimulation and is affected by noise. The signal can be de-noised in part by averaging several points instead of a single one and/or by increasing the number of cycles. Another possibility is to fit the experimental data using least squares regression [44] and to use this synthetic data to calculate the amplitude and the phase. These two alternatives however contribute to slow down the calculations. Alternatively, the FT can be used to extract amplitude and phase information from LT data. The FT can be used with any waveform (even transient signals as in PT, see below) and has the advantage of de-noising the signal.

Investigations on amplitude and phase properties indicate that the phase is considerably less sensitive than the amplitude to reflections from the environment, surface emissivity variations and non-uniform heating [45, 46]. This can be seen from Eq. (1.23) due to the ratio involved in the phase calculation.

The Fourier's Law one-dimensional solution describing temperature *T* at time *t* and depth *z* for a periodic thermal wave propagating through a semi-infinite homogeneous material may be expressed as [43]:

$$T(z,\mathrm{t}) = T_0 \exp\left(-\frac{z}{\mu}\right)\cos\left(\frac{2\pi \cdot z}{\lambda} - \omega \cdot t\right) \tag{1.24}$$

where T_0 is the initial change in temperature produced by the heat source, ω is the modulation frequency ($\omega = 2\pi f$, with *f* being the frequency in Hz), λ is the wavelength; and μ is the diffusion length given by [47]:

$$\mu = \sqrt{\frac{2\alpha}{\omega}} = \sqrt{\frac{\alpha}{\pi \cdot f}} \tag{1.25}$$

where $\alpha = \kappa / \rho c$ is the diffusivity of the material, with κ being the thermal conductivity, *ρ* the density, *c* the specific heat. The probing depth *z*, for amplitude images is given by the thermal diffusion length equation $z \approx \mu$ [48], see Eq. (1.25). For the phase, reported values range from 1.5 μ [49] to more than 2 μ [48]. Nevertheless, long inspection time constitute the principal drawback of LT, since a single experiment should be carried out for every inspected depth. An alternative is to use a very low stimulation frequency, but of course this lengthens the inspection time as well.

1.4. Vibrothermography (VT)

Vibrothermography (VT) is also known as ultrasound thermography [50] or thermosonics [51]. The heating mechanism used in VT is the local conversion of elastic energy into heat which occurs preferably due to local friction losses caused by the relative motion of boundaries in a crack. Heat then travels from the local friction by conduction to the surface where an IR camera can capture the defect signature. Hence, VT is very useful for the detection of cracks, delaminations or loose rivets.

The common approach in VT is to use a coupling media such as a piece of fabric, water-based gels or aluminum, between the transducer and the specimen to reduce losses. There are basically two configurations for VT that can be sought as analog to optical methods described above. The first configuration is burst VT, and the second one is lock-in (also called amplitude modulated) VT.

It should be noted that VT with a fixed carrier frequency close to a resonance frequency of the sample can lead to a strong standing wave pattern which might appear as a superposed temperature pattern hiding defects. One method to solve this problem is simply repeating the acquisition at a different frequency. The other is using ultrasonic frequency modulation either in lock-in or burst VT [52]. The idea of the latter is to cover a range of ultrasonic frequencies, instead of only one, since it is not always possible to predict the right frequency for a particular application. The frequency modulated VT is sometimes called broadband or chirp waveform excitation VT in literature [53].

The burst, lock-in and broadband VT experimental configurations are shown in figure 1.15 [44].

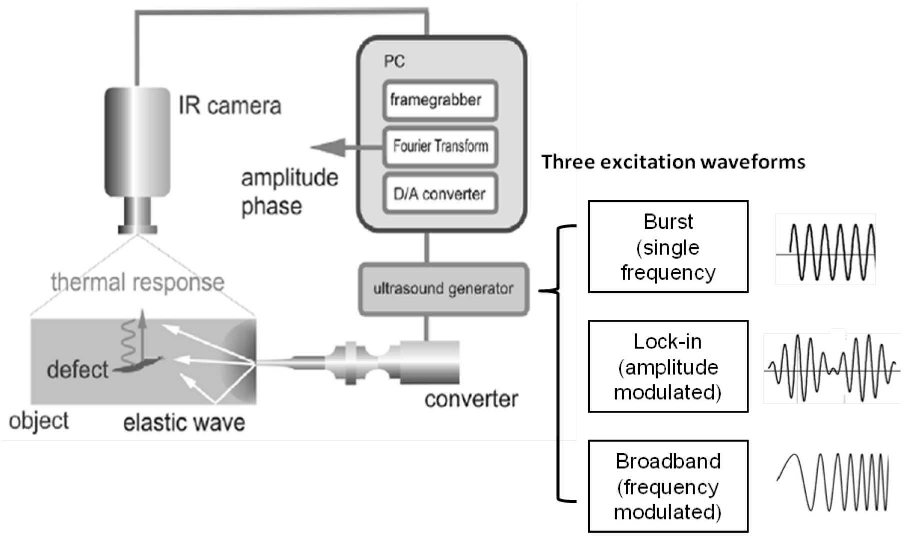

Figure 1. 15. Burst, lock-in and broadband VT experimental configurations [44].

VT has proven more effective than optical thermography to inspect some types of defects, e.g. micro cracks, even though there is lack of quantitative studies. On the contrary, it does not perform very well in some other cases in which application of optical thermography is straightforward, e.g. water detection. It should be emphasized that VT and optical excitation thermography complement each other since they are based on different physical mechanisms.

Chapter 2. Fundamentals of Probability of Detection (PoD) Analysis

PoD analysis as a quantitative measure to evaluate the inspection reliability of a NDT&E technique has been established for decades. It is widely used for traditional NDT&E techniques. In this chapter, fundamentals of PoD analysis are described.

2.1. PoD Curves

PoD curves are the generally accepted method for characterizing and quantifying nondestructive inspection capability and reliability [1, 7]. It is usually expressed as a function of defect size (or other variables). Defect size at 90% PoD with a 95% degree of confidence which is abbreviated as $a_{90/95}$, is a particular value of interest, as shown in figure 2.1 [54]. At Airbus, the aircraft structure has to be designed in such a way, that missing of defects < $a_{90/95}$ is tolerable [55].

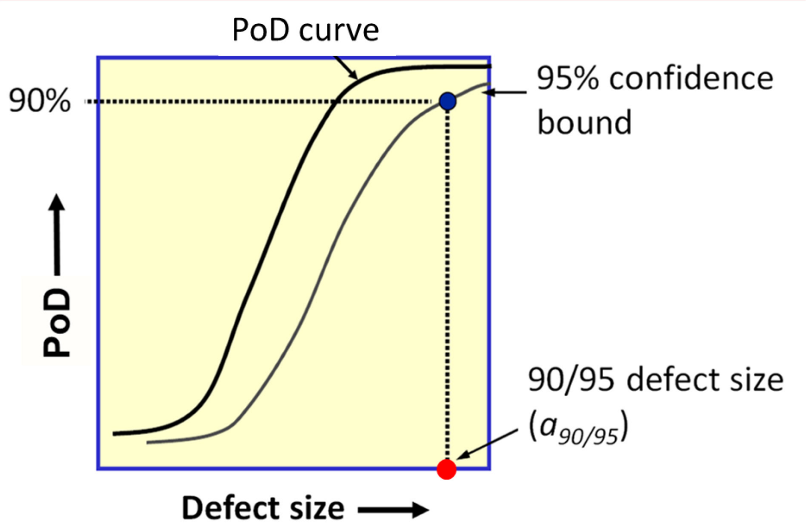

Figure 2. 1. Schematic of PoD curve and corresponding 95% confidence bound [54].

PoD curves are usually estimated from data taken from inspections. Normally the quantitative stimulus responses $\hat{a}$ are recorded as inspection results. Sometimes, inspection results are recorded only in terms of whether or not a flaw was found. Commonly, 1 indicates a flaw was found; 0 indicates a flaw was no found. Data of this nature are called hit/miss data (also called binary data). The PoD function can be formulated either by the quantitative response data ($\hat{a}$ vs. a data) or the hit/miss data. The flaw size a (or other variables) should be uniformly spaced on a Cartesian scale over an appropriate range, which is the recommended practice [7]. It should be noted that if a flaw is so large that it is always found (or saturates the recording device) or so small that it is always missed (or produces a signal which is obscured by the system noise), it provides only limited information about the PoD function.

2.2. PoD(a) from Response Data

As the quantitative NDT&E system is influenced by factors beyond our control, flaws of same size can produce different responses, which can be associated with a probability density $g_a(\hat{a})$. In general, the correlation function between $\hat{a}$ and a can be expressed as follows:

$$\hat{a} = \mu(a) + \varepsilon \tag{2.1}$$

where $\mu(a)$ is the mean of $g_a(\hat{a})$ and ε is a random error accounting for the differences between the measured and true responses. In practice, it is often assumed that ε is normally distributed with zero mean and constant (independent of flaw size a) standard deviation σ_ε. $g_a(\hat{a})$ is then the normal density function with mean $\mu(a)$ and standard deviation equal to σ_ε.

In addition, a decision threshold $\hat{a}_{dec}$ must be set in such a way that, for every flaw size a, if the response signal exceeds this threshold, the system will register a flaw detection. Hence the PoD as function of flaw size can be expressed as follows [1]:

$$PoD(a) = P\{\hat{a}(a) > \hat{a}_{dec}\} = \int_{\hat{a}_{dec}}^{+\infty} g_a(\hat{a})\,d\hat{a} \tag{2.2}$$

Figure 2.2 illustrates the Eq. (2.2), in which the shaded area under the density functions (bell curves) represents the PoD [1]. The source data are plotted in figure

2.2, a linear relationship between *â* and *a* with normal distributed deviations is satisfactory here.

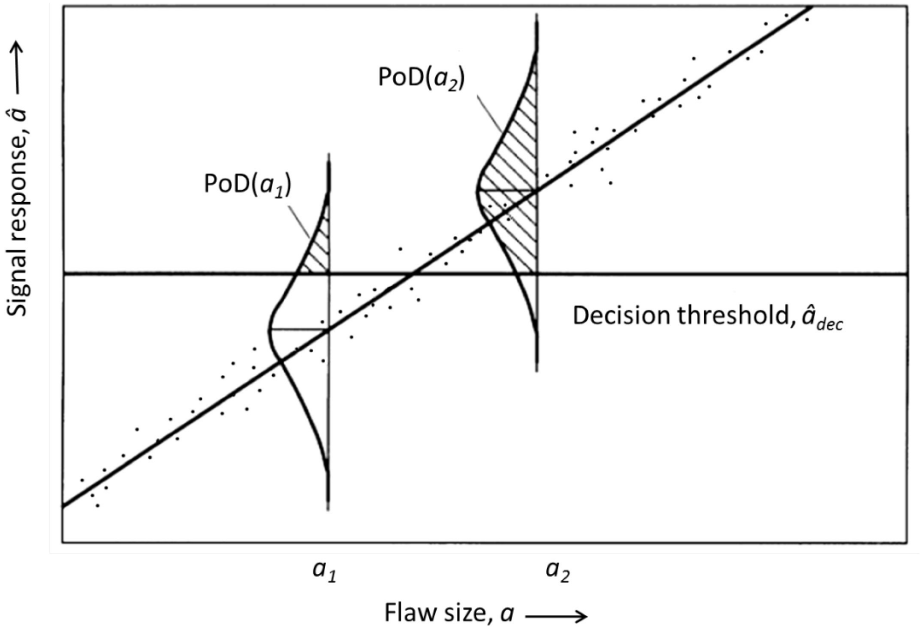

Figure 2. 2. Schematic of PoD calculation from *â* versus *a* relation [1].

In practice, an analysis of response *â* versus size *a* (or other variables) has to be implemented first. Observe the plot of *â* vs. *a*, *â* vs. ln(*a*), ln(*â*) vs. *a*, and ln(*â*) vs. ln(*a*) and choose the best model to fit the data, which can be described well by a straight line and with a variance approximately constant [7]. It has become a common practice to assume that there is a linear relationship between ln(*â*) and ln(*a*) with normal distribution deviations. This model can be expressed by:

$$\ln(\hat{a}) = c + d \cdot \ln(a) + \varepsilon \tag{2.3}$$

where the intercept, *c*, and slope, *d*, are the parameters to be estimated, ε is the normal distribution with zero mean and constant standard deviation, σ_ε .

Assuming that the *â* vs. *a* relation is modeled by Eq. (2.3), the PoD(*a*) function is calculated by setting the decision threshold $\hat{a}_{dec}$, a registration is made if $\hat{a} \geq \hat{a}_{dec}$. The PoD function is then given by [56]:

$$PoD(a) = \Pr ob\left(\hat{a} \geq \hat{a}_{dec}\right) = \Phi\left(\frac{c + d \cdot \ln(a) - \ln(\hat{a}_{dec})}{\sigma_{\varepsilon}}\right) \tag{2.4}$$

where $\Phi(\cdot)$ is a cumulative log normal distribution function.

Eq. (2.4) is often expressed in terms of a mean and a standard deviation, which is written as:

$$PoD(a) = \Phi\left(\frac{\ln(a) - \mu}{\sigma}\right) \tag{2.5}$$

Eq. (2.5) is a cumulative log normal distribution function with mean and standard deviation of log flaw size given by:

$$\mu = \frac{\ln(\hat{a}_{dec}) - c}{d}, \quad \sigma = \frac{\sigma_{\varepsilon}}{d} \tag{2.6}$$

The parameter *c*, *d* and σ_{ε} can be estimated by maximum likelihood (which will be discussed in section 2.3) to provide the best fit to the data set.

2.3. PoD(a) from Hit/Miss Data

Ordinary linear models are used in PoD analysis from response data which are assumed that the observed responses vary continuously and are unbounded. But hit/miss data are neither - the observed outcomes are bounded and discrete, having only 0 or 1 as possible values. For response data, the random error between the observed responses and the model predictions has a continuous, Gaussian (normal) distribution. However, for binary data, the random error between outcomes and model predictions is decidedly non-normal (it's binomial) and so treating it as Gaussian would produce inaccurate and unreliable parameter estimates [7].

Generalized Linear Models (GLM) overcome this difficulty by transforming the data pairs of PoD and flaw size into a linear domain, where the transformed probability can be modeled as an ordinary polynomial function, linear in the explanatory variables (*a* or log(*a*)), and so is a generalized linear model. There are four transform functions (also called link functions). These are the log-odds (logistic or logit function), the log-normal *(*probit function), the complementary log-log link function (often called Weibull by engineers), and the loglog link function [7].

log-odds (logit) link $\ln(p_i/(1-p_i)) = f(X)$

log-normal (probit) link $\Phi^{-1}(p_i) = f(X)$

cloglog link $\ln(-\ln(1-p_i)) = f(X)$

loglog link $-\ln(-\ln(p_i)) = f(X)$

Here $f(X)$ is any appropriate algebraic function which is linear in the explanation variable. For example, $f(X) = \beta_0 + \beta_1 \ln(a)$. $\Phi(\cdot)$is the normal cumulative density function (cdf). *p_i = PoD*(a_i) is the PoD of the i_{th} defect size, a_i.

Using the four link functions we can model PoD(*a*) as:

log-odds (logit) $PoD(a) = \dfrac{\exp(f(X))}{1+\exp(f(X))}$

log-normal (probit) $PoD(a) = 1 - \Phi(f(X))$

cloglog link $PoD(a) = 1 - \exp(-\exp(f(X)))$

loglog link $PoD(a) = -\exp(-\exp(-f(X)))$

The choice of link and use of a logarithmic transform on size can have a large influence on the value for $a_{90/95}$ (The defect size for which a 90% PoD is reached at 95% confidence level). For the symmetric data set, the PoD link functions should be symmetric, either the log-odds or the log-normal. Actually, the log-odds and log-normal PoD curves are similar in practice [50, 57]. In the many situations when the data are skewed to the right, taking the log of size will produce a nearly symmetric data set. Thus the use of a right-skewed link (the loglog link) is very infrequent. In some situations the data are left-skewed and using a symmetric link function penalizes the inspection performance for larger cracks due to lack-of-fit for the smaller cracks. In those situations the left-skewed complementary loglog link function, cloglog, can provide adequate results [7].

2.4. Parameter Estimation

Berens and Hovey presented two approaches for estimating the parameters of the PoD model, the Range Interval Method (RIM) and the Maximum Likelihood Estimates (MLE) [58].

The RIM has been used to estimate the parameters in the PoD analysis from hit/miss data. To implement the RIM, the whole data set is divided into ***t*** intervals of equal length. The PoD is calculated for each interval as being the ratio of defects detected to the total number of defects in that interval, this gives ***t*** data points. The ***t*** data pairs of PoD and defect size are transformed into a linear domain and a linear regression is performed on the data pairs in order to obtain the intercept and slope parameters [57]. PoD curves obtained from the RIM are very sensitive to assumptions made in the execution of the curve fitting algorithm [59], thus the RIM is not recommended.

The MLE technique is used in most applications to find estimates of the parameter of PoD models. Likelihood is “the probability of the data.” It is proportional to the probability that the experiment turned out the way it did. So some PoD model parameters are more likely than others because they explain the inspection outcome better than other values. We choose the “best” parameters, i.e. those that maximize the likelihood.

Let X_i represent the outcome of the i_{th} inspection and $f(X_i;\theta)$ represent the probability of obtaining X_i, where $\theta = (\theta_1, \theta_2, \ldots \theta_k)'$ is the vector of the *k* parameters in the probability model. For example, in a hit/miss experiment, X_i would be 0 or 1 with probability p_i. The likelihood, *L*, of a specific result is given by the likelihood function:

$$L(\theta) = \prod_{i=1}^{i=n} f(X_i;\theta) \tag{2.7}$$

For a given outcome of the experiment, X_i is known and Eq. (2.7) is a function of θ. The maximum likelihood estimate is the value, $\hat{\theta}$, which maximizes $L(\theta)$. For the models considered here, it is more convenient to work with the *ln(L(θ))* [1]:

$$\ln\left(L(\theta)\right)=\sum_{i=1}^{i=n}\ln f\left(X_i;\theta\right) \tag{2.8}$$

which is also maximized at $\hat{\theta}$. The maximum likelihood estimates are given by the solution of the *k* simultaneous equations:

$$\frac{\partial \ln\left(L(\theta)\right)}{\partial \theta_i}=0, \qquad i=1,\cdots,k \tag{2.9}$$

Any standard computational method, such as the Newton-Raphson iterative procedure [60], can be used to find the solutions to Eq. (2.9). Because iterative techniques converge to local maxima, the solution to Eq. (2.9) may be sensitive to the initial values. For the hit/miss data, a set of initial values based on the method of moments has been found to be useful in the literature [61].

It should be noted that MLE corresponds to the well-known Least Squares Estimation (LSE) if the experimental errors have a normal distribution. Let Y_i represent the response to the variable x_i, given that a linear relationship between Y and x with constant normal distribution $\varepsilon \sim N\left(0,\sigma^2\right)$ has proved satisfactory, which can be expressed as:

$$Y_i=a+bx_i+\varepsilon \tag{2.10}$$

The likelihood function is given as:

$$\begin{aligned}L(a,b)&=\prod_{i=1}^{n}\frac{1}{\sqrt{2\pi}\sigma}\exp\left\{-\frac{1}{2\sigma^2}(Y_i-a-bx_i)^2\right\}\\&=(\sqrt{2\pi}\sigma)^{-n}\exp\left\{-\frac{1}{2\sigma^2}\sum_{i=1}^{n}(Y_i-a-bx_i)^2\right\}\end{aligned} \tag{2.11}$$

Let:

$$Q(a,b)=\sum_{i=1}^{n}(Y_i-a-bx_i)^2 \tag{2.12}$$

Then:

$$\max_{a,b} L(a,b) \Leftrightarrow \min_{a,b} Q(a,b) \tag{2.13}$$

From Eq. (2.11), (2.12) and (2.13) we can see that maximizing $L(a,b)$ i.e. MLE is equivalent to minimizing $Q(a,b)$ i.e. LSE, which means that we are trying to find the straight line to which the squares of vertical deviations are as small as possible (shown as figure 2.3). However, LSE tends to differ from MLE, especially for data that are not normally distributed. When this occurs, MLE should be preferred to LSE. So in PoD analysis MLE is recommended, especially when the sample size is small.

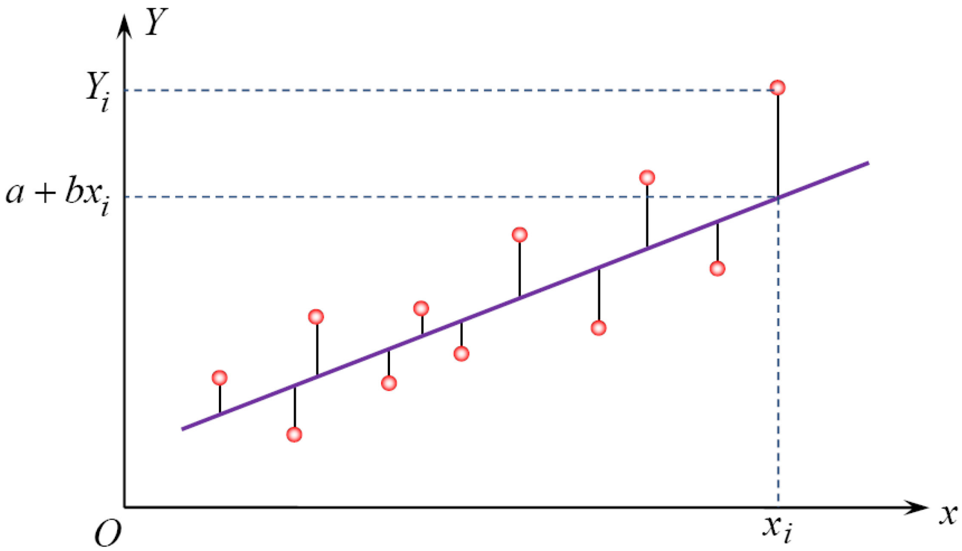

Figure 2. 3. Sketch map of least squares evaluations.

Now we continue with the description of MLE for normal distributed data, let:

$$\begin{cases} \dfrac{\partial Q}{\partial a} = -2\sum_{i=1}^{n}(Y_i - a - bx_i)^2 = 0 \\ \dfrac{\partial Q}{\partial b} = -2\sum_{i=1}^{n}(Y_i - a - bx_i)x_i = 0 \end{cases} \tag{2.14}$$

Then we will get a set of equations:

$$\begin{cases} na + \left(\sum_{i=1}^{n} x_i\right) b = \sum_{i=1}^{n} Y_i \\ \left(\sum_{i=1}^{n} x_i\right) a + \left(\sum_{i=1}^{n} x_i^2\right) b = \sum_{i=1}^{n} x_i Y_i \end{cases} \tag{2.15}$$

By solving Eq. (2.15), we obtain the MLE of *a* and *b*:

$$\begin{cases} \hat{b} = \dfrac{n\sum_{i=1}^{n} x_i Y - \left(\sum_{i=1}^{n} x_i\right)\left(\sum_{i=1}^{n} Y_i\right)}{n\sum_{i=1}^{n} x_i^2 - \left(\sum_{i=1}^{n} x_i\right)^2} = \dfrac{\sum_{i=1}^{n}(x_i - \overline{x})(Y_i - \overline{Y})}{\sum_{i=1}^{n}(x_i - \overline{x})^2} \\ \hat{a} = \overline{Y} - \hat{b}\overline{x} \end{cases} \tag{2.16}$$

And the MLE of mean $\mu(x)$ and deviation σ^2 for normal distributed data:

$$\begin{gathered} \hat{\mu}(x) = \hat{a} + \hat{b}x \\ \hat{\sigma}^2 = \frac{1}{n}\sum_{i=1}^{n}(Y_i - \hat{a} - \hat{b}x_i)^2 = \frac{Q_e}{n} \end{gathered} \tag{2.17}$$

where Q_e is residual sum of squares also known as sum of squared errors of prediction which is a measure of the discrepancy between the data and an estimation model.

2.5. Confidence Bound

For the models being used in NDT&E reliability studies, the maximum likelihood estimated parameters have asymptotically joint normal distribution with means given by the true parameter values, θ_i, and the variance-covariance matrix defined by [1]:

$$V = I^T \tag{2.18}$$

where I is the information matrix whose elements I_{ij} are the expected (*E*) values [1]:

$$I_{ij} = -E\left[\frac{\partial^2}{\partial\theta_i\partial\theta_j}\log f\left(X_i;\theta\right)\right], \qquad i,j = 1,\cdots,k \tag{2.19}$$

In practice, the maximum likelihood estimate $\hat{\theta}$ is substituted for θ in Eq. (2.19). A procedure developed by Cheng and Iles [62, 63] can be used to place lower confidence bounds on the PoD(*a*) function. Such bounds are calculated from the variance-covariance matrix of the estimates and reflect the sensitivity of the experiment to both the number and sizes of flaws in the experimental specimens. The assumed PoD(*a*) model is a cumulative log normal distribution function with parameters $\theta = (\mu,\sigma)'$. For distribution functions defined by location and scale parameters (as is the case of the log normal distribution), the information matrix can be written in the form:

$$I(\mu,\sigma) = \frac{n}{\sigma^2}\begin{bmatrix} k_0 & -k_1 \\ -k_1 & k_2 \end{bmatrix} \tag{2.20}$$

where *n* is the number of defects in the experiment. The lower one-sided confidence bound of the PoD(*a*) function is given by:

$$PoD_\alpha(a) = \Phi(\hat{z} - h) \tag{2.21}$$

where $\Phi(\cdot)$ is the standard cumulative normal distribution, α denotes the confidence level and:

$$\hat{z} = \frac{\ln(a) - \hat{\mu}}{\hat{\sigma}} \tag{2.22}$$

$$h = \left\{\frac{\gamma}{nk_0}\left[1 + \frac{(k_0\hat{z} + k_1)^2}{k_0k_2 - k_1^2}\right]\right\}^{0.5} \tag{2.23}$$

where *n* is the number of defects in the experiment, γ is obtained from table 3-1 for the number of defects in the experiment.

Table 3- 1. Value of γ for lower confidence bounds on the PoD(a) function [1].

Sample Size		20	25	30	40	50	60	80	100	∞
Confidence level, %	90	3.903	3.884	3.871	3.855	3.846	3.839	3.831	3.827	3.808
	95	5.243	5.222	5.208	5.191	5.180	5.173	5.165	5.159	5.138
	99	8.401	8.376	8.359	8.338	8.325	8.317	8.306	8.300	8.273

Commonly, the $a_{90/95}$ magnitudes, i.e. the size of the flaw for which the 95% lower confidence bound crosses the 90% PoD level, is determined. It is guaranteed that flaw size of $a_{90/95}$ will be detected with 90% probability where only 5% might fall outside this confidence limit in case the experiment is repeated.

Except the methodology described above, which is suggested in Metals Handbook [1], another methodology that uses likelihood ratio statistic to define the confidence region can also be found in the literature [56, 64].

2.6. False Positive

False positive (also called false call) is a NDT&E system response which is interpreted as having detected a flaw when none is present at the inspected location. It is important to determine the potential for false positives in experiments, because a PoD estimate has little utility if it is accompanied by an unacceptable false positive rate. The unflawed inspection sites used to estimate the false positive rate need not be a separate specimen. If a specimen presents several locations which might contain flaws, each location may be considered an inspection site. To be considered as such, the sites should be independent, that is, knowledge of the presence or absence of a flaw at a particular site cannot influence the inspection outcome at another site.

According to Military Handbook 2009 [7], to allow for an estimate of the false positive rate, the specimen set should contain at least three times as many unflawed inspection sites as flawed sites.

Chapter 3. PoD Analysis for IRT Technique

In this chapter, first we will present the experimental design to obtain valid source data set for PoD analysis of IRT system. After that, we will concentrate on describing the procedures to obtain PoD curves and corresponding confidence bounds for the quantitative response data and hit/miss data taken from IRT system.

3.1. Experimental Design

The source data is the basis of PoD analysis. No PoD demonstration can be correct for biased, inadequate or erroneous data [65]. In order to obtain a valid data set, the experiment must be well designed and the following aspects should be considered before performing NDT&E reliability experiments for IRT system.

1) Since the results are significantly influenced by the specimens, the test specimens should reflect the structure characteristics that IRT process will encounter in real life applications with respect to geometry, material, surface condition etc. The specimens should be inspected under conditions that are as close as possible to real conditions.

2) Pay attention to the factors that introduce variability into the inspection and control these factors according to your specific application or research purpose, if possible. The important factors that may significantly influence the statistical properties of the obtained data for IRT system are as follow:

- Differences in physical properties of flaws of nominally identical sizes, such as depth, thermal diffusivity, etc.
- The basic repeatability of the response magnitude when a specific flaw is independently inspected by a single inspector using the same equipment and inspection procedure.
- The human factors that induce variability in the experimental operation, data processing and results interpretation process.
- Differences introduced by changes in inspection hardware, such as infrared camera, lens, excitation source.

- Equipment calibration or correction, such as temperature calibration, non-uniform correction and focus adjustment of a given infrared camera.
- Parameter setting in the inspection procedures, such as acquisition time and frequency, excitation energy and duration time, etc.
- Changes in test environment.

All these controlled or uncontrolled factors must be addressed explicitly in every IRT reliability experiment [7].

For the application purpose of PoD analysis, the designed experiment should be representative of its application. So either these important factors must be typical of the application or random samples must be chosen from the population of interest and repeated inspections performed for these factors [7]. For example, if a single inspector is used to characterize an IRT inspection, it must be assumed that this inspector is typical of all the inspectors in the group. An alternative might be to choose a random sample of inspectors from the population eligible to conduct the inspection and have each of the selected inspectors perform the experiment. The methods of accounting for these factors are important aspects of the statistical design of NDT&E reliability experiment.

3) Ensure that there is a sufficient number of flaws to implement PoD analysis. At least 40 flaws are present in experiment whose results recorded in the form of "*a* vs. *â*", and at least 60 flaws whose results recorded in the form of hit/miss is recommended in military Handbook 2009 [7]. Increasing the number of flaws increases the precision of the estimates, so the test set should contain as many flawed specimens as economically feasible. The designed flaw sizes (or other variables) should be uniformly spaced on a Cartesian scale in the range over which the PoD function is rising. If the response signal of a flaw is so large that found (or saturates the recording device) or so small that it is always missed (or produces a signal which is obscured by the system noise), it provides only limited information about the PoD function [6]. This requires us to have some basic knowledge about

the inspection capability of the IRT technique for a given material and certain defect characteristics before the design of a test specimen set.

4) Unlike other NDT&E techniques, a follow-up data processing is often implemented after IRT inspections. As we have previously discussed, effective data processing methods can significantly improve the inspection results. In this study, several data processing methods will be used, such as TSR, FT, and WT discussed previously. All the variables associated with the data processing procedures (for example: order of polynomial fit used in TSR, sampling frequency and truncation window used in FT, wavelet type and center frequency of a mother wavelets used in WT, etc.) should be explicitly addressed. Besides, common image processing functions, such as image resizing, brightness and contrast adjusting, color enhancement, image de-noising and the selection of region of interest, should also be considered.

5) Like other image based NDT&E techniques, one additional step is to collect hit/miss calls from inspectors in order to obtain binary data set. The infrared images after data processing will be presented to one or several inspectors who are not familiar with the specimens and their hit/miss decisions will be collected. Alternatively, we will extract defects automatically by image segmentation to obtain binary result.

It should be noted that when the PoD(*a*) function decreases with increasing flaw size, it is usually an indication that the NDT&E reliability experiments are poorly designed. And when the lower confidence limit decreases with increasing flaw size, notwithstanding an acceptable PoD (*a*) function, it is usually associated with unreasonable values of the mean and standard deviation.

3.2. Procedures of PoD Analysis from Response Data

The procedure of PoD analysis from response data for infrared thermography NDT&E is shown in figure 3.1. A flaw of size *a* (or other variables, such as depth and aspect ratio) causes a signal response, after related data processing (DAC, TSR, FT and WT etc.), we obtain a new quantitative response data $\hat{a}$ (maximum thermal contrast, thermal changing contrast, phase contrast etc.). The statistical distribution of the response signals with respect to the flaw size *a* (or other variables) yields a certain PoD curve.

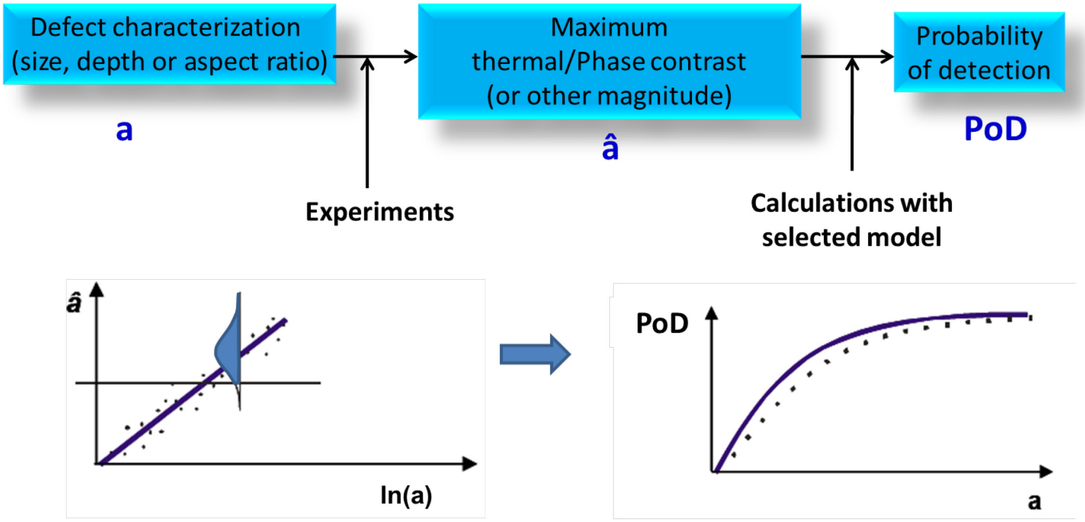

Figure 3. 1. The procedure of PoD analysis from response data for IRT NDT&E.

The following steps are the detailed procedures to obtain a PoD curve from *â* vs. *a* data, where *â* is the quantitative response and *a* is the variable related to defect characteristic.

1. Plot source data and choose the best model

It has become a common practice to assume that there is a linear relationship between ln(*â*) and ln(*a*) with normal distributed deviations. However, our studies indicate that sometimes Cartesian *â vs*. ln(*a*) is a better model for the obtained data set (One such example will be given in Chapter 4.). Then the model can be expressed as:

$$\hat{a} = \beta_0 + \beta_1 \cdot \ln(a) + \varepsilon \qquad (3.1)$$

where the intercept, β_0, and slope, β_1, are the parameters to be estimated, ε is the normal distribution with zero mean and constant standard deviation, σ_ε.

2. Determine decision threshold $\hat{a}_{dec}$, recording threshold $\hat{a}_{th}$ and saturation limit $\hat{a}_{sat}$.

For the image based NDT&E techniques, the decision threshold $\hat{a}_{dec}$ can be determined by observing the source data plots and obtained images. The abnormities should be evident in the images if the corresponding quantitative responses exceed the decision threshold.

For some data sets, it is necessary to set signal recording threshold $\hat{a}_{th}$ and saturation limit $\hat{a}_{sat}$. Once a value is chosen as the saturation limit $\hat{a}_{sat}$, the measurements greater than this value will be considered indeterminable. Similarly, measurements lower than the signal recording threshold $\hat{a}_{th}$ commonly considered as noises are also indeterminable [1]. These censored values will be treated independently in the data regression and parameter estimation process.

3. Parameter estimates

The Maximum Likelihood Estimates (MLE) will be used to find parameter estimates of a PoD model in this project, since it can be applied to smaller data set and can give equivalent answer for large sample size.

Assuming that the source data is modeled by Eq. (3.1), the following is the parameter estimation process which is based on the principle of maximizing the likelihood of the observed data. In order to give more general analysis in which some of the â values are censored at the recording threshold and saturation limit, the likelihood function is partitioned into three regions [51]:

- Region R, for which response values are recorded;
- Region T, for which only a maximum value is known (the response values below the signal recording threshold cannot be recorded);
- Region S, for which only a minimum value is known (the response values above the saturation limit cannot be recorded).

Then, the log of the likelihood function can be expressed as [1]:

$$\begin{aligned}
&\ln[L(\beta_0,\beta_1,\sigma_\varepsilon)] \\
&\quad = -r\ln(\sigma_\varepsilon) - \frac{1}{2\sigma_\varepsilon{}^2}\sum_R [Y_i - (\beta_0 + \beta_1 X_i)]^2 \\
&\qquad + \sum_T \ln\Phi_i(\hat{a}_T) + \sum_S \ln[1 - \Phi_i(\hat{a}_S)]
\end{aligned} \tag{3.2}$$

where *r* is the number of flaws for which *â* values are recorded. $\sum\limits_{\mathrm{R}}$ denotes the sum of those recorded *â* vs. *a* data. $\Phi_i(\hat{a}_T)$ is the probability of obtaining a value below the recording threshold for the i_{th} flaw, and $1-\Phi_i(\hat{a}_S)$ is the probability of obtaining an value above the saturation limit for the i_{th} flaw.

The MLE of the parameters *β₀*, *β₁*, and σ_ε is given by the solution to [1]:

$$\begin{cases}
0 = \dfrac{\partial \ln(L)}{\partial \beta_0} = \dfrac{1}{\sigma_\varepsilon}[\sum\limits_R Z_i + \sum\limits_U V(Z_i) - \sum\limits_L W(Z_i)] \\
0 = \dfrac{\partial \ln(L)}{\partial \beta_0} = \dfrac{1}{\sigma_\varepsilon}[\sum\limits_R Z_i X_i + \sum\limits_U X_i V(Z_i) - \sum\limits_L X_i W(Z_i)] \\
0 = \dfrac{\partial \ln(L)}{\partial \sigma_\varepsilon} = \dfrac{1}{\sigma_\varepsilon}[-r + \sum\limits_R Z_i^2 + \sum\limits_U V(Z_i) - \sum\limits_L Z_i W(Z_i)]
\end{cases} \tag{3.3}$$

where:

$$Z_i = \frac{Y_i - (\beta_0 + \beta_1 X_i)}{\sigma_\varepsilon},\ Y_i = \hat{a}_i,\ X_i = \log(a_i)$$

$$V(Z_i) = \frac{\varphi(Z_i)}{1-\Phi(Z_i)} \tag{3.4}$$

$$W(Z_i) = \frac{\varphi(Z_i)}{\Phi(Z_i)}$$

where *φ(z)* represents the density function of standard normal distribution and $\Phi(Z)$ represents the standard cumulative normal distribution function.

Standard numerical methods, such as the Newton-Raphson iterative procedure can be used to find the solutions to the above partial differential equations group, Eq. (3.4). Excellent choices for the initial estimates of iterative procedures are the intercept, slope, and standard deviation obtained from a standard regression analysis of only those values for which a valid response was recorded [1].

4. Calculate PoD function

Substitute the estimated parameters $\hat{\beta}_0$, $\hat{\beta}_1$ and $\hat{\sigma}_\varepsilon$ from *â vs*. log(*a*) model into the following relationship equations:

$$\hat{\mu} = \frac{\hat{a}_{dec} - \hat{\beta}_0}{\hat{\beta}_1}, \quad \hat{\sigma} = \frac{\hat{\sigma}_\varepsilon}{\hat{\beta}_1} \tag{3.5}$$

Then we will obtain the PoD function, which is expressed as:

$$PoD(a) = \text{Prob}(\hat{a} \geq \hat{a}_{dec}) = \Phi\left(\frac{\ln(a) - \hat{\mu}}{\hat{\sigma}}\right) \tag{3.6}$$

where $\Phi(\cdot)$ is a cumulative log normal distribution function.

5. Calculate confidence bounds

The detailed calculation steps of confidence bounds are given in the ASM Handbook (volume 17) [1]. Once the variance-covariance matrix of $\hat{\mu}$ and $\hat{\sigma}$ are determined, the confidence bounds can be obtained. The list below is the five-step confidence bounds calculation process.

- The elements of information matrix *I* for the estimates are obtained by using Eq. (2.19).
- The variance-covariance matrix of $\hat{\beta}_0$, $\hat{\beta}_1$, and $\hat{\sigma}_\varepsilon$ is obtained by inverting the information Matrix, see Eq. (2.18).
- The variance-covariance matrix of the estimates of $\hat{\mu}$ and $\hat{\sigma}$ is calculated based on a first-order Taylor series expansion of the Eq. (3.5) that relates

$\hat{\beta}_0$, $\hat{\beta}_1$ and $\hat{\sigma}_\varepsilon$ to $\hat{\mu}$ and $\hat{\sigma}$ (The detailed description of this step is given in the ASM Handbook (volume 17) [1].

- The information matrix of $\hat{\mu}$ and $\hat{\sigma}$ is obtained by inverting the variance-covariance $V(\hat{\mu},\hat{\sigma})$, see Eq. (2.18).
- The calculated values are substituted into Eq. (2.21) obtain the confidence bounds.

3.3. Procedures of PoD Analysis from Hit/Miss Data

The following steps are the detailed procedures to obtain a PoD curve from hit/miss data.

1. Determine link function

As previously discussed in Chapter 2, there are four link functions (also called transform functions), from which the data pairs of PoD p_i and flaw size a_i (or other variable) are transformed into a linear domain. And the choice of link function and the use of a logarithmic transform on size can have a large influence on the $a_{90/95}$ value (The defect size for which a 90% PoD is reached at 95% confidence level). Although previous experience shows that log-odds distribution may be the best fits for hit/miss data [6]. However, the link function finally should be chosen according to the obtained data set, especially for IRT technique, since the previous experience is entirely from traditional NDT&E methods. For the symmetric data set, the PoD link functions should be symmetric, either the log-odds or the log-normal. In many situations when the data are skewed to the right, taking the log of size will produce a nearly symmetric data set. Thus the use of a right-skewed link (the loglog link) is very infrequent. In some situations that the data are left-skewed using the complementary loglog link function, cloglog, can provide adequate results [7].

2. Parameter estimates

Take the commonly used model log-odds as an example to depict the procedures of parameter estimates for hit/miss data. Assume that a experiment has produced *k* inspections on each of *n* flaws. Then the likelihood function is given by [1]:

$$L(\mu,\sigma)=\prod_{i=1}^{n}\prod_{j=1}^{\lambda}p_i^{Z_{ij}}(1-p_i)^{1-Z_{ij}} \tag{3.7}$$

where $Z_{th}=0$ or 1 for the j_{th} inspection of the i_{th} flaw producing a miss or a find, respectively, and the probability of detecting a flaw of size a_i is given by:

$$p_i=\frac{\exp(\alpha+\beta\ln(a))}{1+\exp(\alpha+\beta\ln(a))} \tag{3.8}$$

Let

$$\mathrm{h}(a)=\exp(\alpha+\beta\ln(a))=\exp\left[\frac{\pi}{\sqrt{3}}(\frac{\ln(a_i)-\mu}{\sigma})\right] \tag{3.9}$$

where

$$\mu=\frac{-\alpha}{\beta},\quad \sigma=\frac{\pi}{\beta\sqrt{3}}$$

Then

$$p_i=\frac{h(a)}{1+h(a)} \tag{3.10}$$

The log likelihood of Eq.(3.7) is expressed as [1]:

$$\ln L(\mu,\sigma)=\sum_i\sum_j\left[Z_{ij}\ln(p_i)+(1-Z_{ij})\ln(1-p_i)\right] \tag{3.11}$$

The MLE of the parameters μ and σ is given by the solution to:

$$\begin{cases} 0=\dfrac{\partial \ln L}{\partial\mu}=\displaystyle\sum_i\sum_j\left[\frac{Z_{ij}}{p_i}\frac{\partial p_i}{\partial\mu}+\frac{1-Z_{ij}}{1-p_i}(\frac{\partial p_i}{\partial\mu})\right] \\ 0=\dfrac{\partial \ln L}{\partial\sigma}=\displaystyle\sum_i\sum_j\left[\frac{Z_{ij}}{p_i}\frac{\partial p_i}{\partial\sigma}+\frac{1-Z_{ij}}{1-p_i}(\frac{\partial p_i}{\partial\sigma})\right] \end{cases} \tag{3.12}$$

Any standard computational method, such as the Newton-Raphson iterative procedure, can be used to find the solutions to the above partial differential equations group, Eq. (3.12).

Because iterative techniques converge to local maxima, the solution to the equations may be sensitive to the initial values. A set of initial values are recommended in the ASM Handbook (volume 17) [1], which are given by:

$$\mu_1 = X_n - \frac{X_1 p_1}{2} - (0.5)\sum_{i=2}^{n}(X_i - X_{i-1})(p_i - p_{i-1})$$

$$\sigma_1 = \left\{X_n^2 - \frac{p_1}{2}X_1^2 - \mu_1^2 - (0.5)\sum_{i=2}^{n}(X_i^2 - X_{i-1}^2)(p_i - p_{i-1})\right\}^{0.5} \qquad (3.13)$$

where $X_1, \cdots, X_n$ are the ordered values of the natural logs of the flaw sizes and p_i is the observed percentage of detections of the i_{th} ordered flaw size.

3. Calculate PoD function

As previously discussed, for log-odds model, the PoD is written as:

$$PoD(a) = \frac{\exp(f(X))}{1+\exp(f(X))} \qquad (3.14)$$

where

$$f(X) = \alpha + \beta \cdot \ln(a)$$

A mathematically equivalent form of Eq. (3.14) is written as [1]:

$$PoD\,(a) = \left\{1 + \exp - \left[\frac{\pi}{\sqrt{3}}\left(\frac{\ln(a) - \mu}{\sigma}\right)\right]\right\}^{-1} \qquad (3.15)$$

where

$$\mu = \frac{-\alpha}{\beta}, \quad \sigma = \frac{\pi}{\beta\sqrt{3}}$$

Because the log-odds PoD function is practically equivalent to the cumulative log-normal distribution with the same parameters μ and σ (The comparison PoD curves will be given in Chapter 4); The log-normal PoD function with the same parameters μ and σ of Eq. (3.15) can be expressed as:

$$PoD(a) = \Phi\left(\frac{\ln(a) - \mu}{\sigma}\right) \tag{3.16}$$

By substituting the estimated parameters $\hat{\mu}$ and $\hat{\sigma}$ into Eq. (3.15) or Eq. (3.16) we obtain the log-odds PoD function or log-normal PoD function.

4. Calculate confidence bounds

Similar to the calculation of confidence bounds for *â* vs. *a* data, the information matrix ***I*** of $\hat{\mu}$ and $\hat{\sigma}$ need to be calculated for hit/miss data from the following equations [1]:

$$\begin{cases} I_{11} = \dfrac{1}{\sigma^2}\left[\dfrac{\pi^2}{3}\right]\sum_i \dfrac{\mathrm{h}(a_i)}{[1+\mathrm{h}(a_i)]^2} = \dfrac{nk_0}{\sigma^2} \\ I_{12} = I_{21} = \dfrac{1}{\sigma^2}\left[\dfrac{\pi^2}{3\sigma}\right]\sum_i \dfrac{\ln(a_i)\,\mathrm{h}(a_i)}{[1+\mathrm{h}(a_i)]^2} = \dfrac{nk_1}{\sigma^2} \\ I_{22} = \dfrac{1}{\sigma^2}\left[\dfrac{\pi^2}{3\sigma^2}\right]\sum_i \dfrac{(\ln(a_i))^2\,\mathrm{h}(a_i)}{[1+\mathrm{h}(a_i)]^2} = \dfrac{-nk_2}{\sigma^2} \end{cases} \tag{3.17}$$

From Eq. (2.20) to Eq. (2.23) the confidence bounds will be obtained.

Chapter 4. PoD Analysis Based on the Inspection of CFRP Specimen by PT

In this chapter[2], a PoD experimental study was carried out in the framework of a Belgian-Quebec/Canada collaborative research project called ThermoPoD. Experiments were implemented on a Carbon Fiber Reinforced Polymer (CFRP) specimen with embedded material simulating delamination. As it is known, for active IRT, different heating sources (optical or ultrasound), heating forms (pulsed or lock-in) and also data processing methods, such as FT, TSR, WT, DAC, PCT, etc. are of interest. The effect of various data processing methods for PT on PoD curves is compared.

4.1. Introduction

The reliability of a NDT&E technique is one of the most important aspects of the overall industrial inspection procedure. PoD has been utilized for decades as an accepted quantitative measure to evaluate the inspection reliability of a NDT&E technique. Surprisingly, contrary to classical NDT&E techniques such as ultrasonics and eddy current testing for which a significant amount of reliability research has been carried out, a rather limited number of studies on reliability assessment involving active thermography have been published so far [5, 12-14].

PoD analysis, as a statistical method used to estimate the proportion of defects of a given size that can be detected by a particular technique, requires a large amount of samples having defects ranging from non-detectable to minimum detectable sizes and larger. PoD is often used to evaluate the reliability of a particular NDT&E method or a processing technique to detect a certain type of flaw (cracks, delaminations, impact damage, corrosion loss, etc.), at a given depth (or depth range) either manually or automatically.

There are two ways to treat data either as (1) a continuous signal response $\hat{a}$, or as (2)

---

[2] The major content of this chapter has been published in Y. Duan, et al., Journal of Mechanical Science and Technology, vol.26 (7) pp. 1985~1991, 2012 (see Appendix B.1).

a discrete hit/miss response. In the first case, the PoD is obtained from the correlation of variable *â vs. a.* Where *a* denotes defect characterization, such as size, area, aspect ratio, etc. In the second case, data is organized such as a defect is either detected (hit = 1) or not (miss = 0).

In this study, a CFRP specimen with simulated delaminations (Teflon inserts) was inspected by optical PT. Different post-processing routines were performed. The PoD analysis of both continuous response source data and hit/miss source data were studied. Finally, the effects of various data processing methods for PT on PoD curves were compared.

4.2. Experiments and Results

4.2.1. Specimen and Experiment Configuration

Experimental inspections were carried out on a CFRP panel having a total of 25 Teflon square insertions with lateral sizes *D* = 3, 5, 7, 10, and 15 mm, placed between plies at different depths 0.2<*d*<1.8 mm and locations as depicted in figure 4.1.

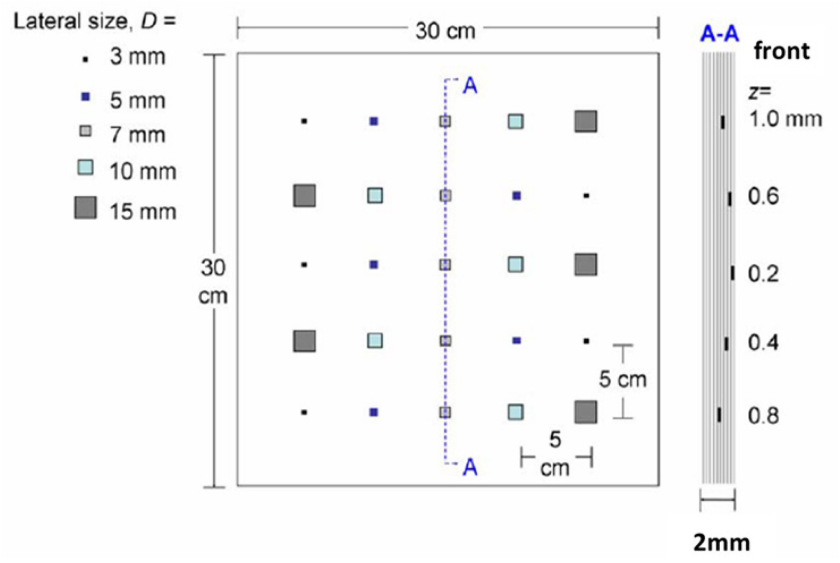

Figure 4. 1. Schematic diagram of specimen design.

The specimen was tested from both sides giving a total 50 inspection targeted sites (flaws with different aspect ratio (Dimension / depth) values, from 3/1.8 to 15/0.2).

The data acquisition was carried out using a Focal Plane Array (FPA) infrared camera (Santa Barbara Focalplane SBF125, 3 to 5 µm), which has a 320×256 pixels array. Two high-power flashes (Balcar FX 60), giving 6.4 kJ each for a 5 ms pulse duration, were used as heating sources in reflection mode. For the front side inspection (defect depth from 0.2 to 1.0 mm), the acquisition frequency used was f_s = 157 Hz and 1000 frames were recorded. For the back side inspection (defect depth from 1.0 to 1.8 mm), the acquisition frequency f_s = 45 Hz was used and 1080 frames were recorded. The small acquisition frequency on the latter case was to ensure sufficient time to detect the deeper defects.

In IRT, the defect depth and size significantly influence the response signal strength. Hence, the PoD curves as a function of aspect ratio were studied.

4.2.2. Inspection Results by Different Data Processing Techniques

Thermal images were acquired before, during and after a short optical pulse was applied on the specimen surface. Even though PT is fast and allows the inspection of extended surfaces [15], raw PT data is difficult to analyze because of non-uniform heating or reflections, as shown in figure 4.2.

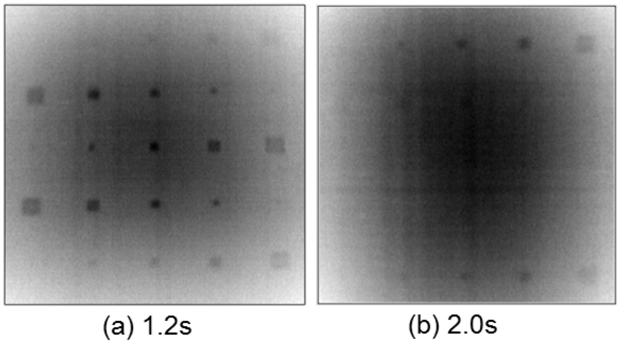
(a) 1.2s
(b) 2.0s

Figure 4. 2. Raw images (a) at t = 1.2s in front side inspection, (b) at t = 2.0s in back side inspection.

There are a great variety of processing techniques that can be employed to improve the defect detection capability. Inspection results obtained by different data processing are presented next.

It should be noted that, before applying various data processing methods, the recorded data were sub-sampled by a factor 4 to increase the data processing speed.

Fourier Transform (FT)

FT is particularly interesting among the data processing methods since it allows retrieving phase and amplitude data from temperature - time history of each pixel. Analyzing phase data obtained from FT to get improved inspection results in PT is known as PPT in literature [19]. In practice, a FFT algorithm available in common data processing software, allows processing the signal more effectively.

Figure 4.3 shows the phase images of different frequencies, which are more tolerant to non-uniform heating, emissivity variations, and environmental reflections compared to amplitude images. Obviously, the non-uniform heating effects and noises (high frequency component) are significantly reduced in phase images as compared to raw images (figure 4.2). Besides, some small defects are only visible on phase images.

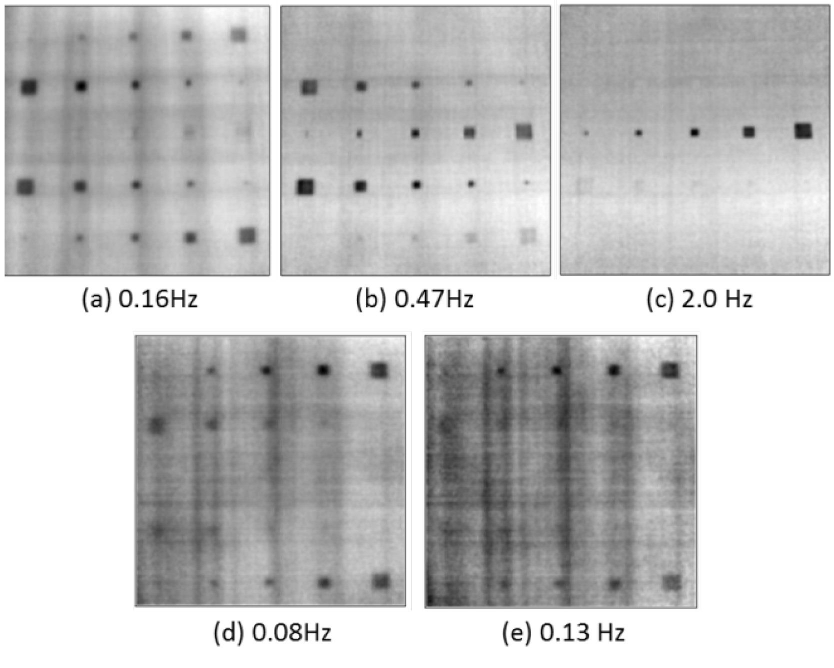

(a) 0.16Hz (b) 0.47Hz (c) 2.0 Hz

(d) 0.08Hz (e) 0.13 Hz

Figure 4. 3. Phase images of different frequencies obtained by FT: (a) - (c) front side inspection, (d) and (e) back side inspection.

Thermal Signal Reconstruction (TSR) and 1st Derivative (1st D)

1st derivative after the TSR is another very useful PT processing technique, which achieves a significant improvement in signal to noise performance as well as providing a good sensitivity to smaller and deeper defects [28]. A low order expansion is applied on temperature - time history of each pixel in order to serve as low pass filter that preserves the essential thermal response. In the logarithmic domain, the inclusion of higher orders only replicates noise that appears in the later, while low orders correspond to the temperature data. It has been found that a 4th (or 5th order) polynomial provides an excellent fit to PT data [29].

The TSR method provides a significant data compression, since it is only necessary to save the polynomial coefficients. It is also convenient for generating time derivative images without additional noise contributions. Actually, the signal to background contrast is dramatically improved after performing 1st derivative of the TSR, as shown in figure 4.4.

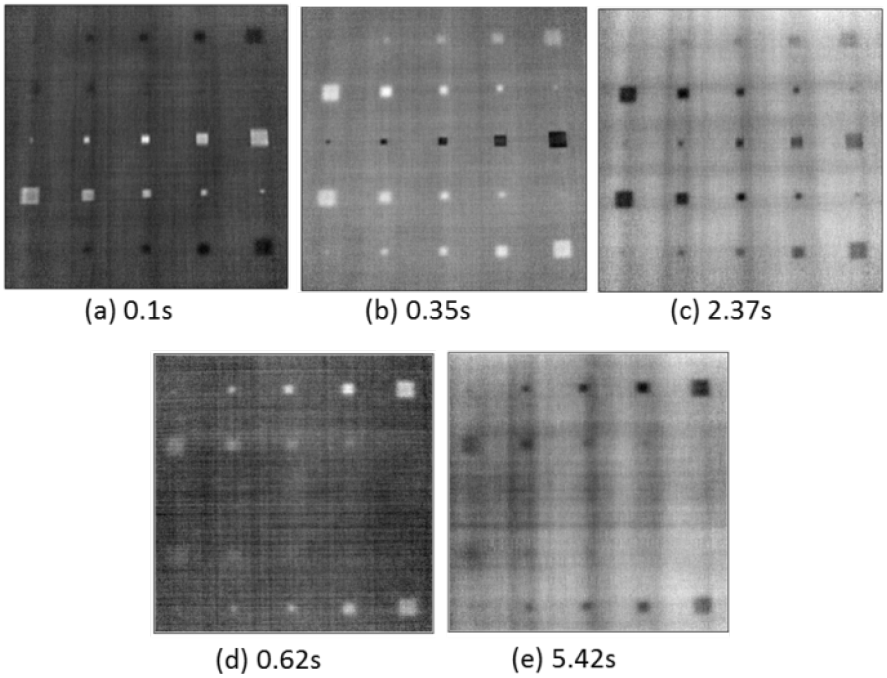
(a) 0.1s
(b) 0.35s
(c) 2.37s
(d) 0.62s
(e) 5.42s

Figure 4. 4. 1st derivative images after the TSR at different times: (a) - (c) front side inspection, (d) and (e) back side inspection.

Wavelet Transform (WT)

WT can be seen as an extent of FT that preserves the time information, which is directly correlated to the defect depth, while it keeps FT interesting features. In wavelet analysis, a fully scalable modulated window is used instead of the fixed truncation window used in FT. The window is shifted along the signal and for every position, the spectrum is calculated. Then this process is repeated many times with a slightly shorter (or longer) window for every new cycle. At the end, the result will be a collection of time-frequency representations of the signal, all with different resolutions [33].

A complex Morlet wavelet, as recommended in literature [34], was selected as the mother wavelet. Figure 4.5 shows the phase evolution of line profile (through 5 defects with same depth of 0.4mm) as function of translation factor *T* (related to observation time) with fixed scale factor *S* (related to frequency) of 200.

Larger scale factors that correspond to stretched wavelets were also used to detect the deeper defects. Figure 4.6 shows the phase images of different translation factor obtained by WT with fixed scale of 500.

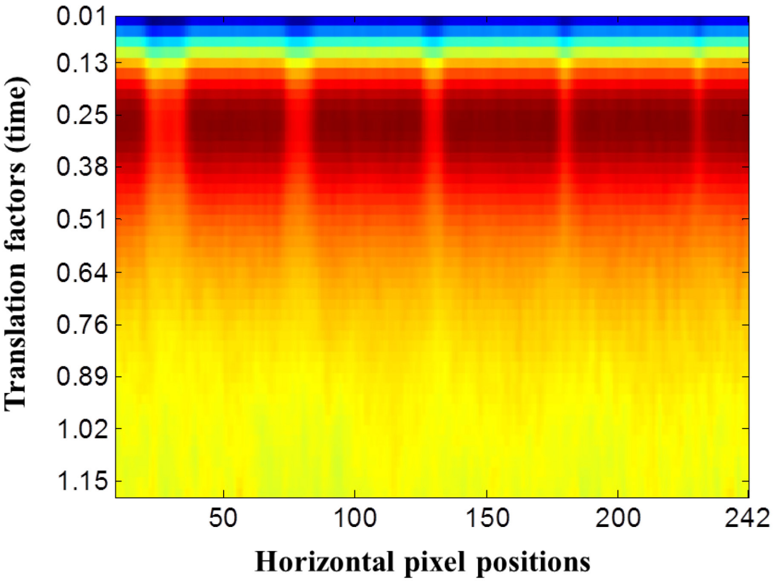

Figure 4. 5. Phase evolution for a horizontal line through the center row of defects (depth = 0.4mm) in translation factor(*S* = 200).

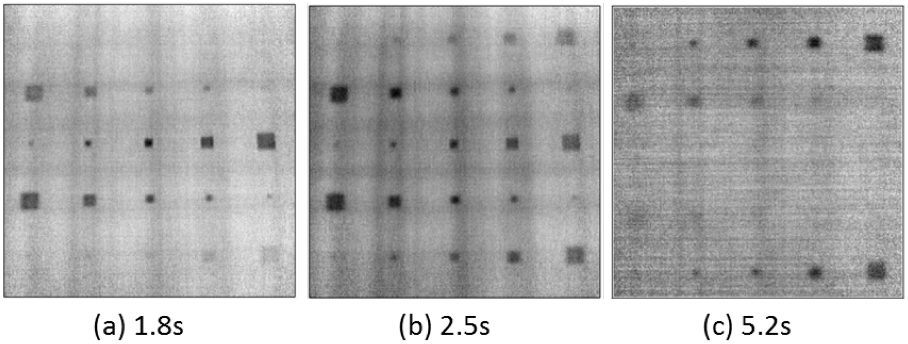
(a) 1.8s (b) 2.5s (c) 5.2s

Figure 4. 6. Phase images of different translation factor (time) obtained by WT with fixed scale factor *S* = 500: (a) and (b) front side inspection, (c) back side inspection.

Differential Absolute Constrast (DAC)

Traditionally, contrast methods require the use of the temperature of a sound area where it is known that no defect is present under the surface. However, it is not always possible to precisely locate such sound area from the raw IR images in advance. In DAC, subjective defect-free-zone definition is no longer necessary.

Theoretically, the surface temperature is the same either on defect free or defect area before the time that the shallowest defect appears [38, 39]. This allows locally predicting the expected sound area temperature at any given time after the heating pulse occurs at any place, especially for the defect areas. In DAC, the temperature evolution of the sound area is not measured. Instead, it is an extrapolation of temperature computed using a 1-D heat transfer model starting from its initial known temperature just right after the heat impulse.

The difference between the extrapolated temperature as it is computed and the temperature as it is actually measured, gives the thermal contrast on the surface. The obtained thermal contrast images have proven that DAC is effective against non-uniform heating, as is shown on figure 4.7.

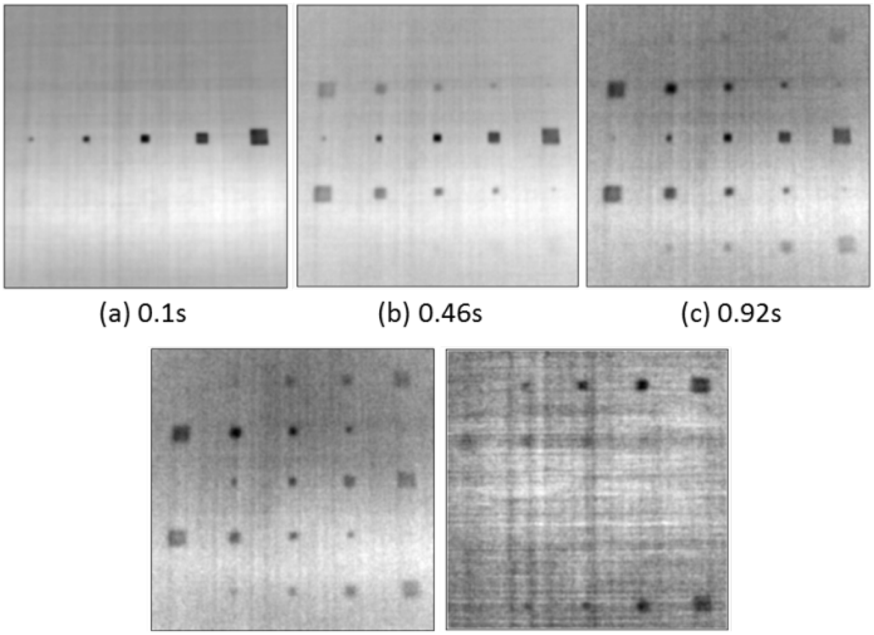

(a) 0.1s (b) 0.46s (c) 0.92s

(d) 1.61s (e) 1.69s

Figure 4. 7. Thermal contrast images at different time obtained by DAC: (a) - (d) front side inspection, (e) back side inspection.

Principal Component Thermography (PCT)

PCT [41] uses SVD to extract the spatial and temporal information from a thermogram matrix. Unlike FT which is relying on a set of sinusoidal basis functions to decompose signal in the temperature-time space to a phase-frequency space, SVD is an eigenvector-based transform that form an orthonormal space.

Assuming data is represented as an M×N matrix $\boldsymbol{A}$ (M>N), then the SVD allows writing [41]:

$$\boldsymbol{A} = URV^T \qquad (4.1)$$

where U represents a set of orthogonal statistical modes known as EOFs describing spatial variations of data [41]. V^T is the transpose of PCs that represent the time variations.

Figure 4.8 shows the first few EOFs obtained after applying PCT for our experimental data.

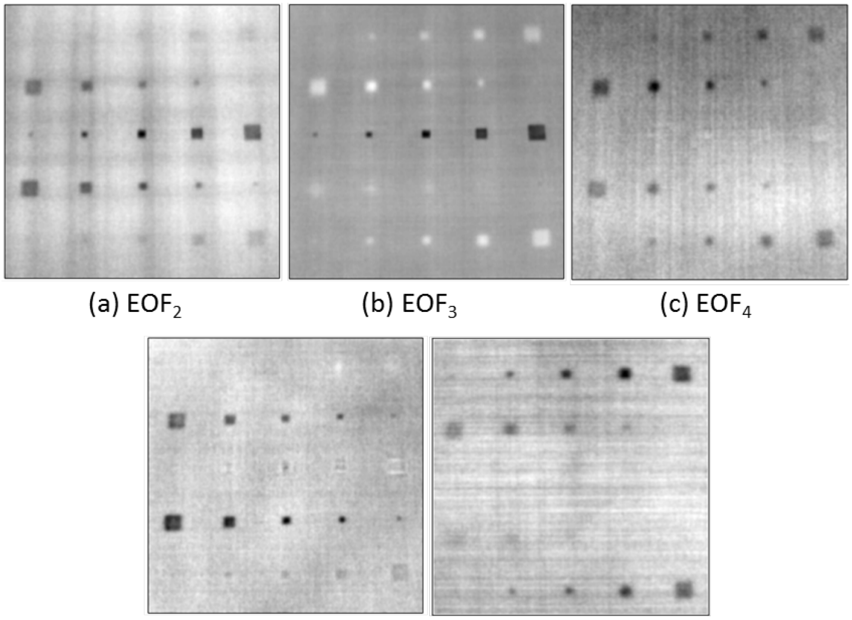

(a) EOF$_2$ (b) EOF$_3$ (c) EOF$_4$

(d) EOF$_5$ (e) EOF$_4$

Figure 4. 8. EOFs obtained by PCT: (a) - (d) front side inspection, (e) back side inspection.

4.3. PoD Analysis Results

4.3.1. PoD Analysis of Continuous Response Data

First, inspection results obtained from FT is analyzed and organized in the correlation of maximum phase contrast φ vs. aspect ratio r, in order to implement PoD analysis.

Considering that inspectors usually determine the defects by comparing the thermal anomalies and their surrounding areas, a square region (13×13 pixels) adjacent to a certain defect was selected as the sound area instead of using an identical sound area.

Figure 4.9 shows the phase contrast profiles for the line of defects at d = 0.4 mm. As can be seen, the defect contrast depends on the size of the defect, but they all can be seen on the same range of frequencies. Similar profiles were obtained for defects at different depths. From those profiles, a data set of φ vs. r was obtained (see Appendix A.1).

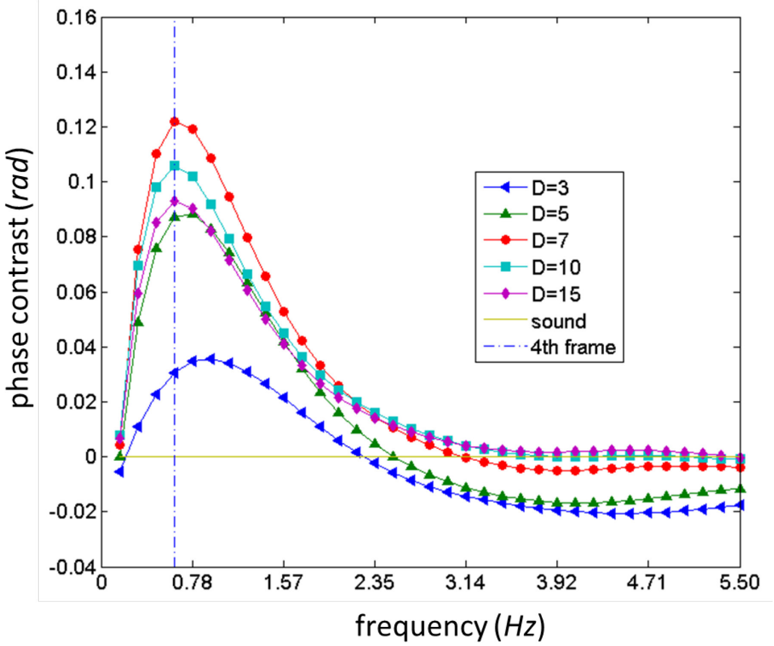

Figure 4. 9. Phase contrast profiles for delaminations at 0.4 mm.

First, an analysis of source data φ vs. r was implemented to choose the best model that can be properly described by a straight line and the variance is approximately constant.

Figure 4.10 shows the four possible models: φ vs. r, φ vs. ln(r), ln(φ) vs. r, and ln(φ) vs. ln(r) for our source data. From these graphs it can be concluded that the φ vs. ln(r) model, shows the most linear correlation although the data is considerably scattered. Hence, a straight line mathematical expression can be used in order to represent this behavior as follows:

$$\varphi = c + d \cdot \ln(r) + \varepsilon \tag{4.2}$$

where φ denotes the maximum phase contrast, r denotes the aspect ratio, c is the intercept, d is the slope, and ε is the normal distribution with zero mean and constant standard deviation σ_ε .

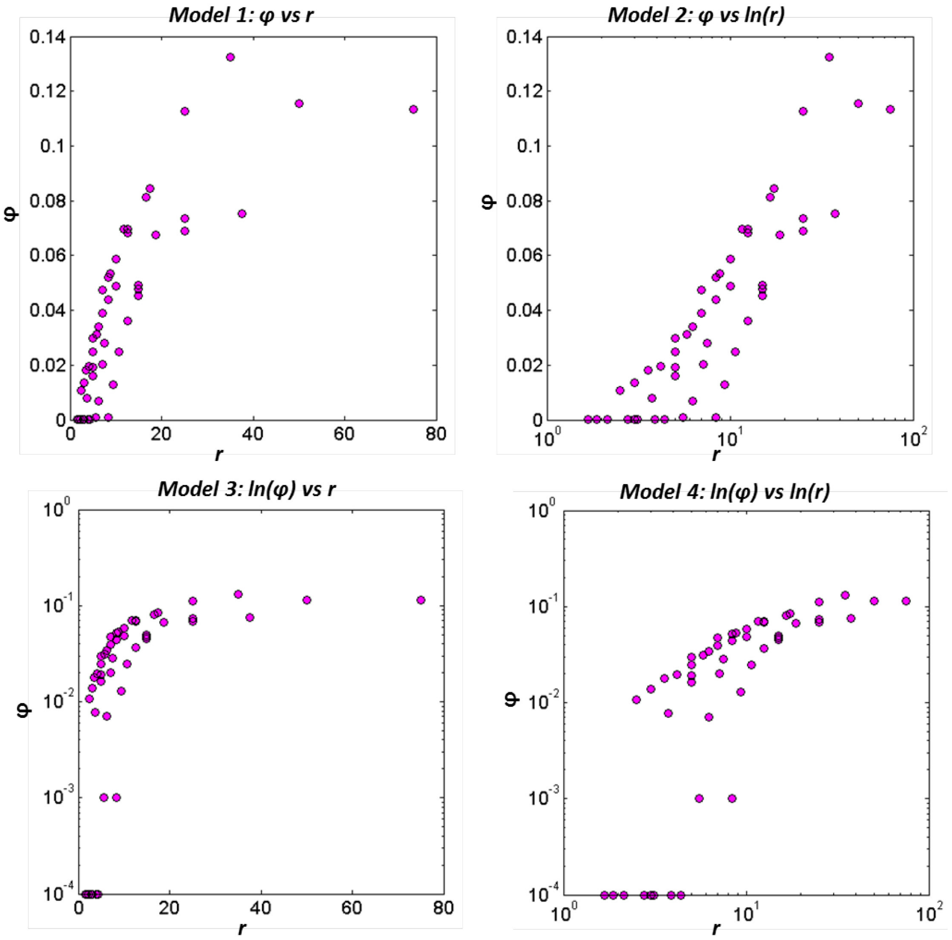

Figure 4. 10. The four possible models that show φ vs. ln(r) is the best model for our data set.

In PoD analysis of a continuous response data set, the PoD function is calculated by setting a decision threshold. Here, the decision threshold φ_{dec} was set as 0.02 rad. This value was decided based on a noise level analysis. The phase contrast greater than 0.02 rad can be considered as defect rather than noise.

The φ vs. ln(r) relation was modeled by Eq. (4.2), for every flaw r, if φ exceeds the decision threshold φ_{dec}, the flaw will be interpreted as detectable. Hence the PoD function was given by [56]:

$$PoD(r) = \text{Prob}(\varphi \geq \varphi_{dec}) = \Phi\left(\frac{c + d \cdot \ln(r) - \varphi_{dec}}{\sigma_\varepsilon}\right) \tag{4.3}$$

where $\Phi(\cdot)$ is a cumulative log normal distribution function.

Eq. (4.3) is often expressed in terms of a mean and a standard deviation to emphasize the connection to distribution function, which is written as:

$$PoD(r) = \Phi\left(\frac{\ln(r) - \mu}{\sigma_\varepsilon}\right) \tag{4.4}$$

Eq. (4.4) denotes a cumulative log normal distribution function with mean and standard deviation of log flaw size given by:

$$\mu = \frac{\varphi_{dec} - c}{d} \quad , \quad \sigma = \frac{\sigma_\varepsilon}{d} \tag{4.5}$$

Six Newton-Raphson iterations were implemented to get the Maximum Likelihood Estimates (MLE) of parematers *c*, *d* and σ_ε. The Least Square Regression (LSR) was also implemented. The MLE regression result and the corresponding 95% prediction bounds, as well as LSR fitting are shown in figure 4.11.

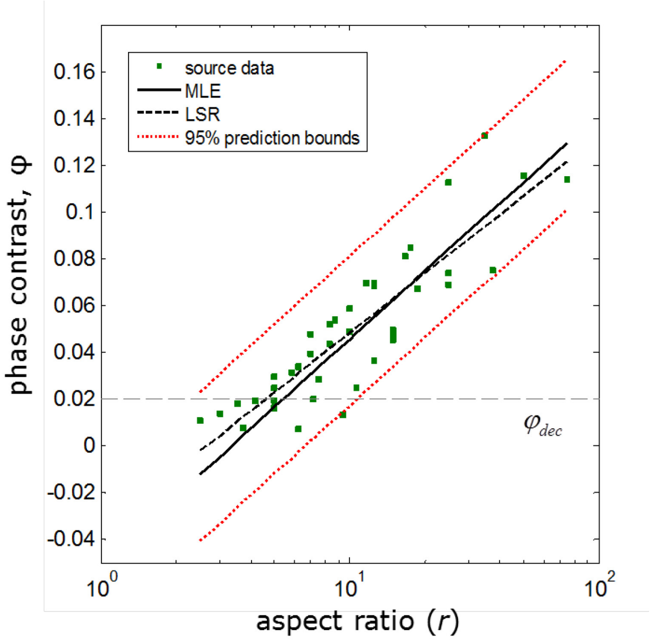

Figure 4. 11. Fitting results by MLE and LSR.

The fitting results by MLE and LSR are obviously different for our data set. As discussed in Chapter 2, MLE is recommended for small sample size data.

The variance-covariance matrix of the estimated parameters was obtained by statistics software. Subsequently, the information matrix was determined, as well as the lower and upper confidence bounds, which were calculated from the equations found in the literature [7]. In this study, MATLAB® software was used to calculate the lower and upper confidence bounds from the variance-covariance matrix.

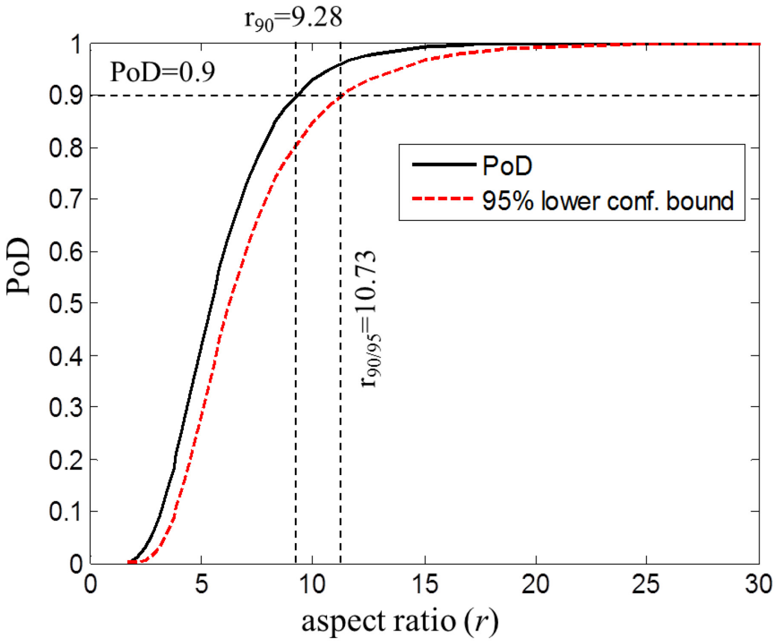

Figure 4. 12. PoD curve and corresponding lower confidence bound (decision threshold is 0.02rad).

Figure 4.12 displays the PoD curve using the function given in Eq. (4.3) and the corresponding 95% lower confidence bound, which yield an r_{90} (the defect aspect ratio with 90% PoD) of about 9.28 and $r_{90/95}$ (the defect aspect ratio for which the 95% lower confidence bound crosses the 90% PoD level) of about 10.73. It is guaranteed that flaws with the aspect ratio $r_{90/95}$ will be detected with 90% probability where only 5% might fall outside this confidence limit in case the experiment is repeated.

For figure 4.12, the decision threshold was set to 0.02 rad. It should be noted that the decision threshold dramatically influence the PoD analysis result. Table 4-1 shows the r_{90} and $r_{90/95}$ values for different decision thresholds. As can be seen from Table 4-1, and as expected, both the r_{90} and $r_{90/95}$ values increase as the decision threshold increases.

Table 4- 1. r_{90} and $r_{90/95}$ values using different decision thresholds.

Decision threshold	r_{90}	$r_{90/95}$
0.010	7.29	8.48
0.015	8.23	9.53
0.020	9.28	10.73
0.025	10.48	12.11
0.030	11.82	13.68

4.3.2. PoD Analysis of Hit/Miss Data

If a single inspector is used to demonstrate the reliability of a NDT process, it must be assumed that this inspector is typical of all the inspectors. An alternative might be to choose a random sample of inspectors from the total pool and have each of the selected inspectors perform the experiment [1]. The PoD result and the false alarm rate could be dramatically different by experienced or inexperienced inspector. So PoD study normally involves multiple inspectors in industry. In this study, the experiments were performed by an experienced inspector who is familiar with the experimental equipment and parameter settings of infrared thermography. The hit/miss source data were obtained from the observation of another experienced inspector who did the data processing and marked defects on the resulting phase images obtained by FT (PPT). One denotes detected, zero denotes not detected. It should be noted that the flaws locations were known to the inspector, which may influence the inspector’s interpretation of flaws detected.

Similarly to the PoD analysis of continuous response data, the first step for PoD analysis of hit/miss (binary) data is choosing the model. There are four models corresponding to four link functions [7]. The log-odds and log-normal models are commonly used in practice, especially for symmetric data sets. The log-odds and log-normal link functions, used to link the binary data to the defect size *a* (or other variables) through the probability of either outcome (1 or 0), can be written as:

log-odds link: $\ln(p_i/(1-p_i)) = f(X)$ (4.6)

log-normal link: $\Phi^{-1}(p_i) = f(X)$ (4.7)

where $f(X)$ is any appropriate algebraic function, which is linear in the explanation variable, for example, $f(X) = \beta_0 + \beta_1 \ln(a)$, $\Phi(\cdot)$ is the normal cumulative density function, $p_i = PoD(a_i)$ is the PoD of the i_{th} defect size, a_i.

Using the two link functions we can model PoD(*a*) as:

log-odds model: $$PoD(a) = \frac{\exp(f(X))}{1+\exp(f(X))} \quad (4.8)$$

log-normal model: $$PoD(a) = 1 - \Phi(f(X)) \quad (4.9)$$

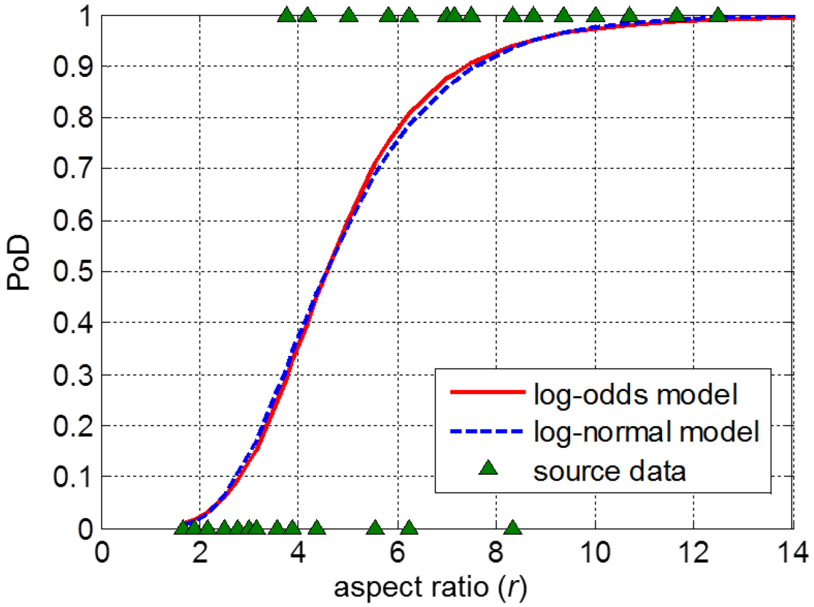

Figure 4. 13. Comparison of log-odds and log-normal PoD curves of hit/miss data set obtained from resulting images after FT.

Because the variance of the transformed function is not constant like it is for an ordinary regression, a special maximum likelihood method was implemented to obtain the estimate parameters: intercept β_0 and slope β_1 [1].

Figure 4.13 compares the log-odds and the log-normal PoD curves of the hit/miss data set organized from the resulting images obtained by FT (PPT). As can be seen in this graph, the log-odds and log-normal curves are very close. For PoD values lower than about 0.5, the log-normal curve estimates defect sizes slightly lower than the log-odds model. On the contrary for PoD values higher than 0.5, the log-normal is slightly higher than the log-odds model, meaning that for a given PoD the corresponding defect size is slightly larger for the log-normal curve than the log-odds.

4.3.3. Effects of Data Processing Routines on PoD

It is not possible to set an identical decision threshold for all different data processing since the magnitudes of the data processing results are different. However, there is no need to set a decision threshold for the PoD analysis of hit/miss data. Hence, the raw thermal images and all the resulting images obtained by different data processing methods, including FT, 1st D of TSR, WT, DAC and PCT were analyzed and compared. Six hit/miss data sets were obtained (see Appendix A.2), similarly to the procedure described for the FT (PPT), for the raw and processed data and used to create the PoD curves.

Table 4-2 shows the summary of the inspection results by non-processed and different data processing techniques.

Table 4- 2. Summary of the inspection results by different data processing manipulations.

Data processing manipulations	Number of inserts detected	Detection rate
Non-processed	19	38%
DAC	30	60%
WT	35	70%
FT(PPT)	36	72%
PCT	38	76%
1st D of TSR	40	80%

Log-odds model was used to plot the PoD curves. In order to compare the effects of data processing methods, the PoD curves from raw data and the data obtained by different data processing manipulations were plotted on the same axis, as shown in figure 4.14.

The 95% lower confidence bounds for each data processing method was also calculated. Table 4-3 shows the defect aspect ratio with 90% PoD (r_{90}) and the defect aspect ratio for which a 90% PoD is reached at 95% confidence level ($r_{90/95}$). It indicates that the inspection results were improved dramatically by any of the data processing manipulations. Moreover, for these experiments, 1st D of TSR and PCT are slightly more effective than other routines for our specimen.

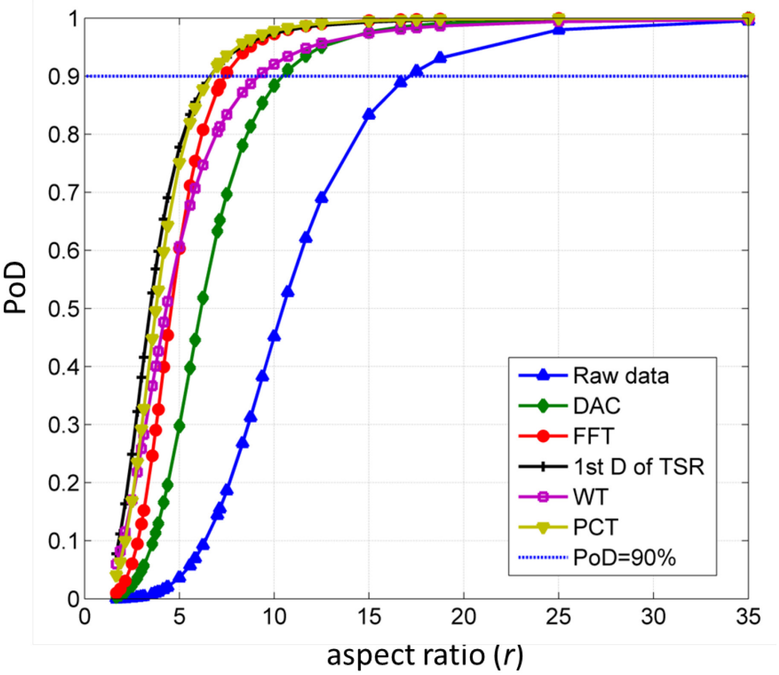

Figure 4. 14. Comparison of PoD curves from different data processing manipulations, including PoD curves of raw data.

Table 4- 3. r_{90} and $r_{90/95}$ values obtained by different data processing manipulations on hit/miss data.

Data processing manipulations	r_{90}	$r_{90/95}$
Non-processed	17.06	30.04
1st D of TSR	6.60	11.50
PCT	6.64	10.91
FT (PPT)	7.37	11.44
WT	9.20	17.63
DAC	10.39	16.93

.

4.4. Summary

A CFRP specimen with embedded delaminations (Teflon inserts) was tested by optical PT. Different data processing routines were implemented to improve the inspection results. PoD analysis of both continuous response data and hit/miss data were carried out based on these results. At last, log-odds model which is commonly used for hit/miss data was chosen to create PoD curves of different data processing routines. It is observed that the inspection results were improved dramatically by any of the data processing manipulations. 1st D of TSR and PCT are slightly more effective than other routines for our specimen.

ThermoPoD researches advance the wide acceptation of infrared thermography NDT out of laboratory, since the reliability and capability of infrared thermography NDT system is then quantitatively evaluated, as traditional NDT approaches. It also allows for standardization and characterization of the data processing applied in the industry for the detection of defect.

Chapter 5. PoD Analysis of Optical LT and PT for Aluminum Foam Material

In this chapter[3], quantitative evaluation of optical thermographic techniques relative to the non-destructive inspection of aluminum foam material is studied. For this purpose, a set of aluminum foam specimens with Flat-Bottom Holes (FBH) was inspected by both optical LT and PT. PoD analysis, as a quantitative method to estimate the capability and reliability of a particular inspection technique, was studied and compared for both optical LT and PT inspection results.

5.1. Introduction

Aluminum foam material combines the advantages of high strength and low weight. Structural efficiencies and relatively low cost makes this material of widespread use in aerospace, marine, and automotive structures [66]. Potential applications of such materials include sound and energy absorption appliances, cores for structural sandwich panels, and electromagnetic wave shields, among many others [67].

Nondestructive Inspection (NDI) studies of aluminum foam material are rarely found in literature except from X-ray inspection [68, 69]. The material has a low overall X-ray absorption because of the large amount of voids inside, which allows large specimens to be inspected by X-ray tomography. X-ray tomography has been proven to be a very powerful tool allowing characterizing the architecture or microstructure of cellular materials [69]. However, each NDI technique has its own strengths and weaknesses. Compared with X-ray tomography, the main advantages of optical excitation thermography are fast inspection rate, security (no harmful radiation involved) and single-side needed (stimulation and inspection on the same side) [70]. In this study, two classical optical thermographic techniques: LT and PT will be employed to inspect aluminum foam material.

The intention of this work is to quantitatively evaluate the capability and reliability of optical LT and PT on the aluminum foam material. PoD curves, as an accepted

---

[3] The major content of this chapter has been published in Yuxia Duan, et al., Journal of Infrared Physics and Technology, vol. 60 pp. 275~280, 2013 (see Appendix B.2).

quantitative measure of the NDI reliability and capability, are plotted to compare the obtained inspection results, by employing either LT or PT approaches.

5.2. Specimens and Inspection Configurations

5.2.1. Specimen Description

Experimental inspections were carried out on a set of aluminum foam specimens having a total of 72 FBH with 12 lateral diameters *D* = 6, 8, 10, 12, 15, 18, 20, 22, 25, 27, 30, and 32 mm. The defect depth *d*, i.e. the distance between the inspected surfaces and the bottoms of the holes, goes from 1 to 6 mm.

In order to assess results, X-ray tomography was performed first for every specimen. Figure 5.1a shows the schematic illustration of one aluminum foam specimen, having 5 FBH with different lateral diameters and same depth *d* = 2 mm. Figure 5.1b and c show the corresponding X-ray tomographic images (2D slides) of the specimen, from which we can see the 5 FBH, as well as the amount of closed cells with non-uniform sizes.

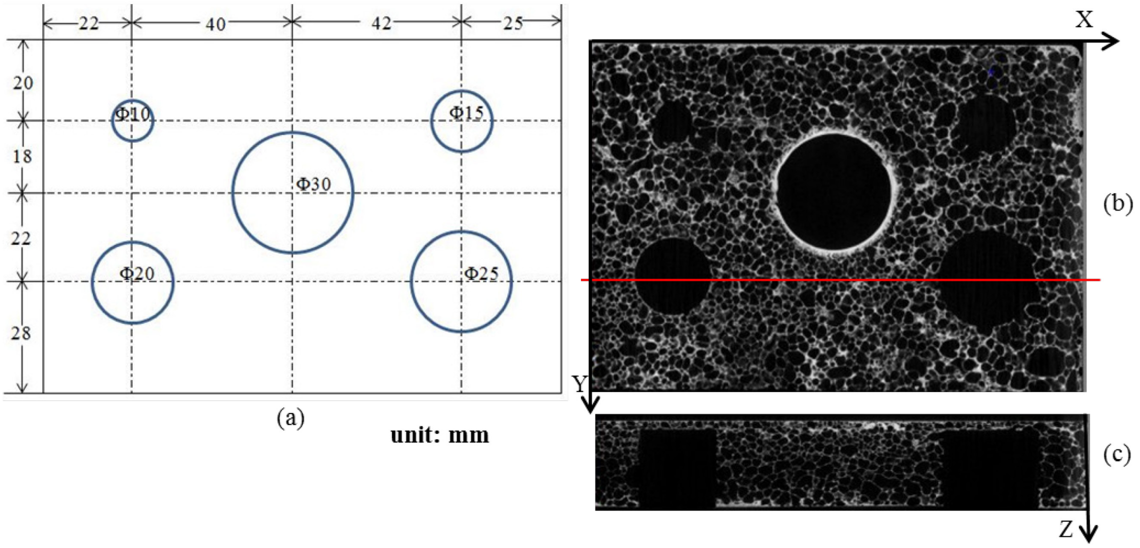

Figure 5. 1. (a) Schematic illustration of one representative specimen with defect depth *d* = 2 mm, (b) X-Y slide tomographic image (Z = 3 mm), and(c) X-Z slide tomographic image of the marked horizontal line.

5.2.2. Inspection Configuration

In optical excitation thermography, the energy is delivered to the surface of the specimen where the light is transformed into heat; while an infrared camera is used to monitor changes of the object's surface temperature. Since the subsurface discontinuities may alter the diffusion of the heat, this will affect the cooling behavior of the nearby region on the surface.

In this study, the optical thermography inspection setup included two OMNILUX PAR64 (1000 watt) halogen lamps, which generated sinusoidal or pulsed thermal waves. The lamps and the infrared camera were located on the same side with respect to the specimen surface, as shown in Figure 5.2. A CEDIP titanium infrared camera was used to detect the thermal wave. Table 5-1 shows the important technical specifications of the CEDIP camera.

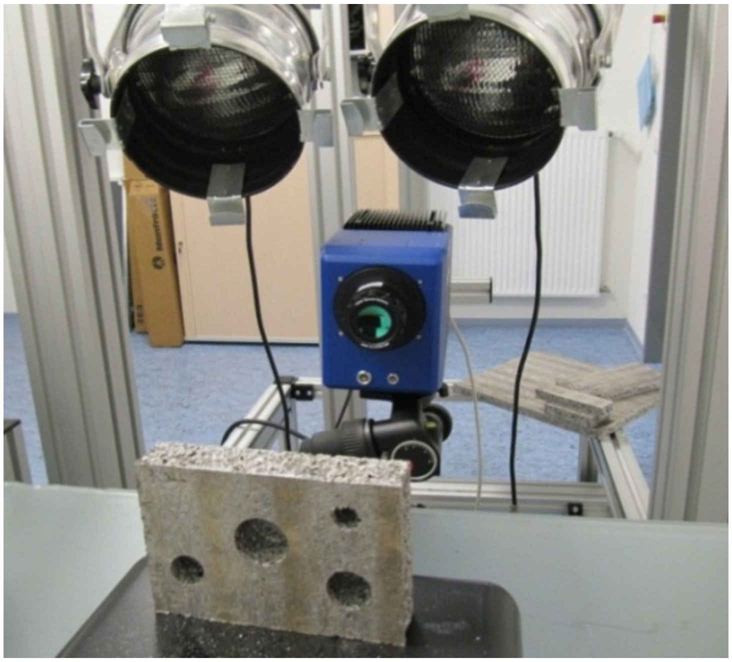

Figure 5. 2. Photograph of the optical thermography system.

Table 5- 1. Technical specification of CEDIP titanium camera.

Technical specification	Explanation/value
Sensor type	MCT
Waveband	3.7 ~ 4.5 μm
Pixel resolution	640 ×512
Pixel raster	15 μm
Thermal sensitivity	< 18 mK
Cooler	Integrated stirling cooler
Max full frame rate	117 Hz
Digital output	14 Bit GigE
Integration time	10 μs ~ 5 ms
Temperature calibration	0° C ~ 160 °C

Lock-in Thermography (LT)

In optical LT, as discussed in Chapter 1 (section 1.3), probing depth heavily depends on the heating frequency; the lower modulation frequency, the deeper penetration. Inspections start at a relatively high excitation frequency at which, depending on the thermal diffusivity of the material, only shallow defects are visible. In order to detect deeper defects, the excitation frequency is gradually decreased until the appropriate value is reached. Preliminary tests indicated that excitation frequencies ranging from 1 down to 0.05 Hz were adequate to completely cover the depth range of interest, from very shallow to 6 mm. The acquisition frame rate was set to 50 Hz. Longer acquisition times are required for the low frequencies to obtain sufficient modulating periods with which to average. Increasing the number of periods aided in reducing the noise level and to improve image Signal Noise Ratio (SNR) and subsequently, defect contrast.

Phase images or phasegrams are analyzed since they are more tolerant to the non-uniform heating, emissivity variations, and environmental reflections compared to amplitude images [15]. Furthermore, as discussed in Chapter 1 (section 1.3) they provide probing capabilities deeper than amplitude images.

One commonly used method to retrieve phase and amplitude is 4-point methodology for sinusoidal stimulation phase [45, 46]. The 4-point methodology is fast but it is valid only for sinusoidal stimulation and is affected by noise. The signal can be de-noised in part by averaging several points instead of a single one and/or by increasing the number of cycles. Another possibility is to fit the experimental data using least squares regression [44] and to use this synthetic data to calculate the amplitude and the phase. These two alternatives however contribute to slow down the calculations. Alternatively, FT can be used to extract amplitude and phase information from LT data. The FT can be used with any waveform (even transient signals as in pulsed thermography, see below) and has the advantage of de-noising the signal. In this study, FT is employed to retrieve phasegram from the raw LT data.

Pulsed thermography (PT)

Two OMNILUX PAR64 (1000 watt) halogen lamps were employed to generate 0.5 seconds long pulse energy. Data acquisition in PT is fast and allows the inspection of extended surfaces.

In order to obtain the optimum results, two important parameters need to be carefully selected: the sampling rate f_s, and the acquisition time t_{acq} [25]. In this work, the acquisition time t_{acq} ranged from 20 to 60 s, while the sampling rate f_s varied from 25 to100 Hz, depending on the depths of the FBH.

As described in Chapter 1 and Chapter 4, there are a great variety of processing techniques that have been developed to improve the inspection results of PT. In this study, data processing methods that will be used in PT includes:

- Pulsed Phase Thermography (PPT) [19], which allows retrieving phase and amplitude data from a PT experience through FFT. This method can be thought as being a combination of PT and LT. In a similar manner as for LT, phase data is commonly analyzed since it is more tolerant to the non-uniform heating and environmental reflections.

- Thermographic Signal Reconstruction (TSR) [31], which provides a significant degree of data compression since only polynomial coefficients are stored. It is also convenient for generating derivative images without additional noise contributions. Furthermore, performing 1st or 2nd time derivatives of the TSR provides a significant improvement in signal to noise performance as well as providing a good sensitivity to smaller and deeper defects [28].

- Principal Component Thermography (PCT) [41], which uses SVD to extract the spatial information described by EOFs and temporal information represented by PCs from a thermogram sequence. This method usually results in high levels of thermal contrast for the subsurface defect.

5.3. Resulting Images Analysis

All of 12 aluminum foam specimens were inspected by the same lab inspector. For LT data, phasegrams were analyzed by an experienced inspector. For PT data, PPT, 1st derivatives of TSR, and PCT data processing techniques were carried out to improve the defect detection capability by the same experienced inspector. Example of resulting images from LT and PT inspection for a specimen with defects of different sizes but the same depth (2 mm), are shown in figure 5.3.

The inspector visually examined the resulting images to give a qualitative evaluation of the appearance of every defect. It should be noted that the inspector knew the real location of every defect, which may influence the inspector’s interpretation. The inspector record the inspection result in terms of whether or not a flaw was found: 1 denotes a flaw was found, 0 denotes a flaw was not found. Subsequently, a set of hit/miss data was obtained, which will be used for the following statistical analysis to obtain the PoD curves (see Appendix A.3). Table 5-2 shows a summary of the LT and PT inspection results.

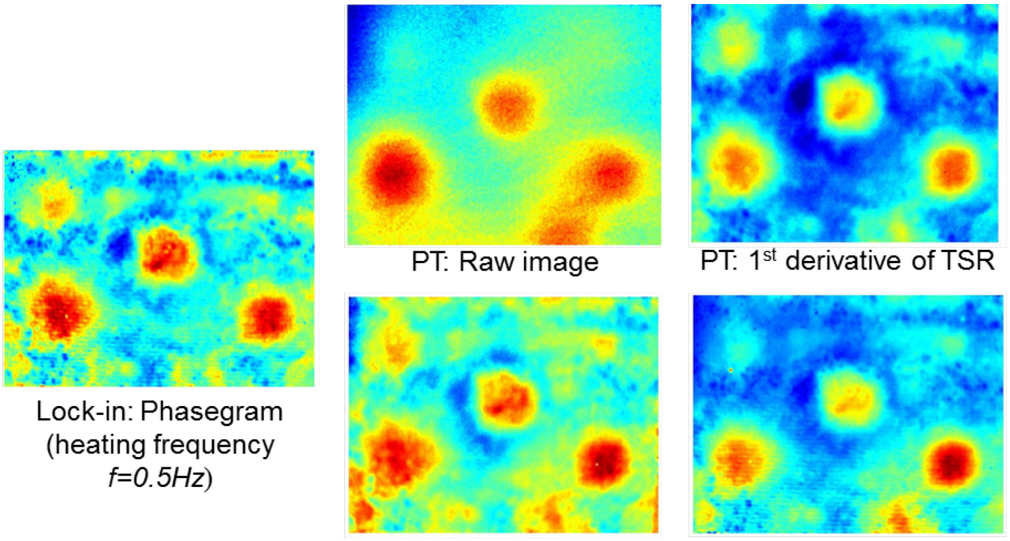
PT: Raw image

PT: 1st derivative of TSR

Lock-in: Phasegram (heating frequency *f=0.5Hz*)

PT: Phasegram after PPT

PT: 2nd frame after PCT

Figure 5. 3. Resulting images obtained from LT and PT for a specimen with defects of different size but the same depth 2 mm.

Table 5- 2. Summary of LT and PT inspection results.

Inspection techniques	**Results images**	**Number of FBH detected**	**Detection rate**
LT	Phasegrams	46	64%
PT	Raw images	40	55%
PT	PPT phasegrams	44	61%
PT	1st derivative of TSR images	50	69%
PT	PCT EOFs	44	61%

5.4. PoD Analysis and Comparison

As we know, defect depth significantly influences the inspection result as well as the defect size detected in thermographic technique. Hence, the PoD curves as a function of aspect ratio *r* (*D/d*) were studied. The log-odds and log-normal models are commonly used to obtain the PoD function. In most cases, the PoD curves from log-odds and log-normal models are quite similar, as discussed in Chapter 4 (section 4.3.2). In this study, the log-normal model is used for PoD analysis, which is usually written as:

$$PoD(r) = \Phi(c + d \cdot \ln(r)) \tag{5.1}$$

Eq. (5.1) is often expressed in terms of a mean and a standard deviation, which is expressed as:

$$PoD(r) = \Phi\left(\frac{\ln(r) - \mu}{\sigma}\right) \tag{5.2}$$

Eq. (5.2) is a cumulative log normal distribution function with mean and standard deviation of log defect aspect ratio given by:

$$\mu = \frac{\ln(r) - c}{d}, \quad \sigma = \frac{\sigma_\varepsilon}{d} \tag{5.3}$$

The parameters *c*, *d* and σ_ε were estimated by maximum likelihood to provide the best fit to the data set.

Figure 5.4 compares the PoD curves of LT and PT. The effects of commonly used data processing methods in PT, including PPT, 1st derivative of TSR, and PCT are compared as well.

Lower confidence bounds at 95% were calculated for each data set to reflect the degree of uncertainty. Table 5-3 shows the defect aspect ratio with 90% PoD (r_{90}) and the defect aspect ratio for which 90% PoD is reached at 95% confidence level ($r_{90/95}$).

As can be seen from table 5-3, the inspection capability of LT is higher than PT without additional processing of raw data, i.e. the r_{90} and $r_{90/95}$ values are lower. However, the inspection results of PT were dramatically improved after data processing. The inspection capability of PT is even higher than the LT after 1st derivative of TSR processing.

It should be noted that due to the material property, analysis of the false positive rate is difficult. X ray results show that the designed minimum defect size is greater than the maximum pore size. A discussion about the size of the voids that can be considered as a defect is necessary before implementing false alarm.

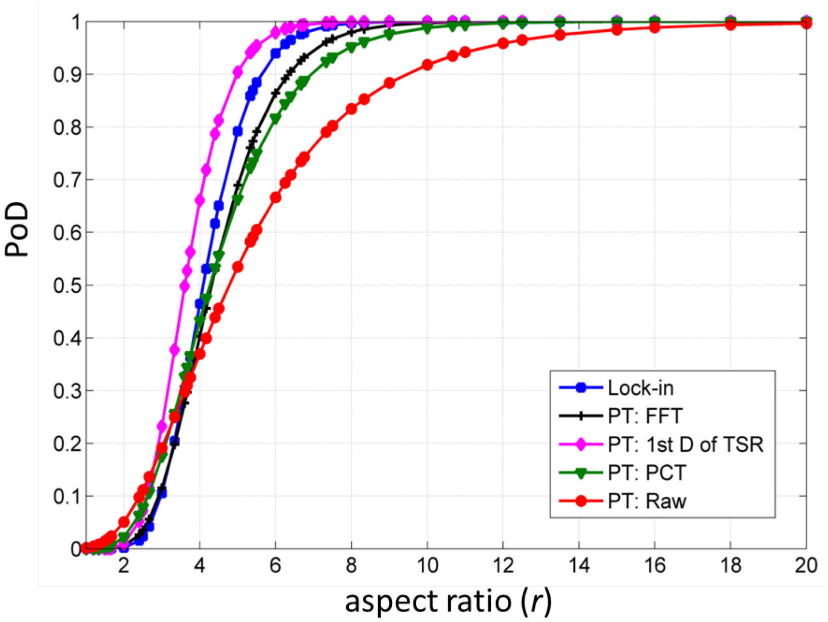

Figure 5. 4. PoD curves of LT and PT with different data processing manipulations, including raw data.

Table 5- 3. r_{90} and $r_{90/95}$ values obtained by LT and PT.

Inspection techniques	**Resulting images**	r_{90}	$r_{90/95}$
LT	Phasegrams	5.5	7.1
PT	Raw images	9.1	14.5
PT	PPT phasegrams	6.2	8.3
PT	1st D of TSR images	4.9	6.3
PT	PCT EOFs	6.7	9.4

5.5. Summary

Optical excitation thermography is an attractive tool for the non-destructive evaluation of aluminum foam material, especially in the cases where X-ray tomography may not be possible, such as inspections of very large areas or accessibility restricted to one side of the sample.

The main advantages of LT are that the directly acquired data is rather easy to handle. However, long inspection time constitutes the principal drawback of LT, since a single experiment should be carried out for every inspected depth. An alternative is to use a very low stimulation frequency, but this approach will only work for FBH, which are thick defects ranging from the initial depth to the total thickness of the sample. In the case of delaminations for instance, several defects could be missing using a very low modulating frequency. Data acquisition in PT is relatively fast. However, raw PT data is commonly difficult to analyze because of the non-uniform heating or reflections. As a result, additional processing of the data is required.

PoD analysis results of LT and PT indicate that post-processing in PT, including PPT, 1st D of TSR and PCT, improved the thermal contrast for the subsurface defect, especially the smaller and deeper defects. As a result, PT and LT provide comparable inspection results.

Chapter 6. PoD Analysis of UT and PT for Impact Damage of CFRP

As it is well-known, there is no such thing as a perfect NDT&E technique. All inspection methods fail in detecting defects or anomalies at some point. UT which is widely used in NDT&E field is not an exception. In this chapter[4], comparative experimental results and PoD analysis results for impact damage of CFRP by UT and optical PT are presented. The quantitative comparion shows that PT has higher inspection reliability than UT in some inspections.

6.1. Introduction

UT is a well established NDT&E technique which has the ability to detect defects or damages in almost all thicknesses of materials. However, it has the distinct disadvantages of being intrinsically slow and requiring a coupling agent [74, 75]. The use of optical PT technique for the NDT&E of aerospace materials has progressively increased in the last few decades. It offers noncontact, rapid detection of subsurface defects [15-17, 76-78]. The main disadvantage of IRT is that it can only detect damage near surface (within≈4mm, depending on material's thermal diffusivity and defects size). However, in order to reduce aircraft weight, advanced alloy plate-like, sandwiched structures and fiber reinforced laminates instead of heave metals are widely used in aircrafts. IRT techniques have proven to be an effective way to detect and, in many cases, to quantify the subsurface defects and damages in some materials.

PoD curve and the corresponding lower confidence bound are often used to evaluate the reliability of a particular NDT&E method. In this work, PoD curves and lower confidence bounds are plotted to compare the obtained inspection results, by employing either UT or PT approaches.

---

[4] Partial content of this chapter has been presented at the 10th International Conference on Quantitative Infrared Thermograpy (QIRT), Québec, Canada, July 27-30, 2010.

6.2. Experiments and Results

The experimental results were provided by the Wallonie Aeronautics Network (WAN) NDT Lab at Gosselies, Belgium. 35 CFRP specimens with thickness from 2.3mm to 4mm were impacted with a metal penetrator. The impact energy ranges from 10J to 36J. Both UT and PT methods are used to inspect the impact damage inside the specimens.

6.2.1. UT Experimental Setup

In this study, through transmission C-scan approach with probes on each side of the CFRP plate is employed, as illustrated in figure 6.1. For every CFRP plate, the inspection routine employed is automated ultrasonic inspection using 0° probes with frequency 5MHz which is selected based on the thickness of the plate. The transducers and the specimen are immersed in water for coupling.

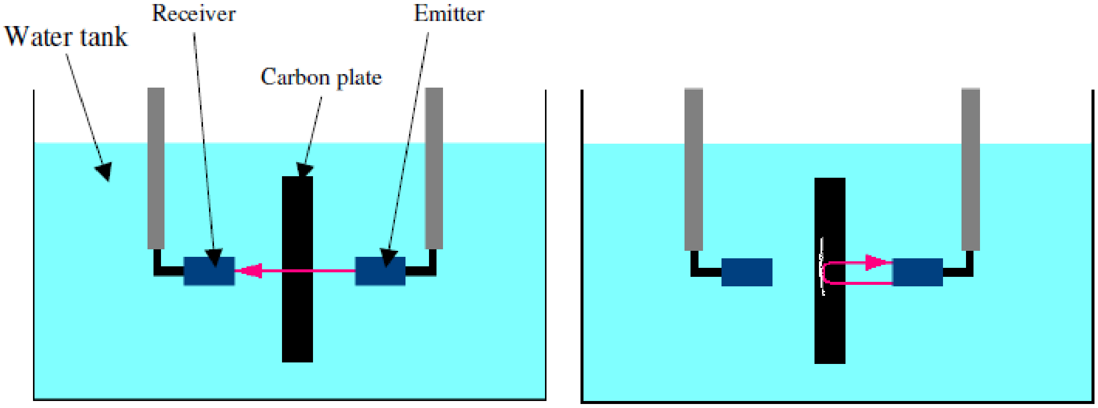

a) Ultrasonic wave pass through the carbon plate with no defect

b) Ultrasonic wave is rebounded by the internal defect in the carbon plate. None or reduced signal is caught by the receiver

Figure 6. 1. UT experimental setup.

The principle of through transmission UT is to catch the signal sent by the emitter with the receiver and to measure its amplitude. The received ultrasonic signal amplitude is more attenuated over the defective zone than on the non-defective zone. In this work, the defect sizes have been limited with 6 dB technique which means that the amplitude measured in the defective zone is at least twice smaller than in the defect free area. The transducers are scanned in a plane parallel to the sample in a rectilinear raster pattern and the measurements are taken with 1 mm index.

6.2.2. PT Experimental Setup

PT inspection setup includes one big halogen lamp (1000 watt), which generates 3 seconds heating pulse and an uncooled microbolometer with waveband 8~12 μm, is used to detect and record the thermal signal. The data acquisition time is set as 30 seconds to ensure sufficient time to detect the deepest impact damage. The lamp and the infrared camera are located on the opposite sides with respect to the specimen surface (transmission mode), as shown in figure 6.2. The distance from lamp to specimen surface is 11 cm. The distance from specimen surface to microbolometer is 15 cm. FFT is applied to the raw thermal sequence to obtain phase images which is more tolerant to non-uniform heating.

Figure 6. 2. PT experimental setup.

6.2.3. Image Analysis

The resulting images are analyzed and recorded by one experienced inspector. Figure 6.3 shows the comparable inspection results of four representative samples by PPT and UT. (a) - (d) are the phase images obtained from PPT, (e) - (h) are the ultrasonic C-scan results. Figure 6.4 shows a worse case scenario for PPT. The 45° oriented defect is well detected by UT , which means that amplitude measured in this area is more than 6dB attenuation. The 45°oriented defect is not detected by PPT, which means that the SNR is less than 2 and thermal abnormity area is less than 4 pixels width. Figure 6.5 shows a worse case scenario for UT. The 0° oriented defect is well detected by PPT, but not detected by UT.

The large defects are not what we are dealing with since they are detectable for both UT and PPT. The focus is on the small defects, for example the 45°oriented defect in figure 6.4 and 0°oriented defect in figure 6.5. Figure 6.6 shows an example of SNR analysis of a phase image and the defect size determination method. When measuring the size of a defect, the specimen width whose real values are known is commonly selected as a reference length.

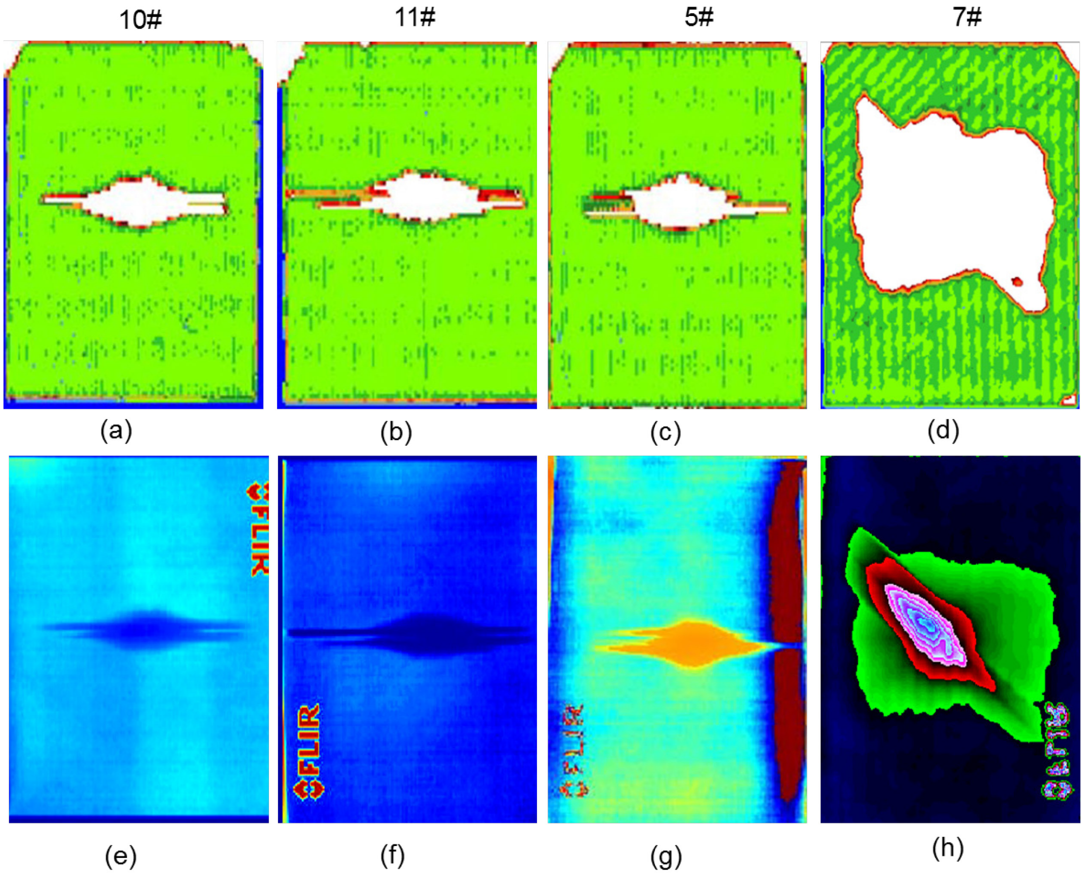

(a) (b) (c) (d)

(e) (f) (g) (h)

Figure 6. 3. Comparable inspection results by PPT and UT: (a) - (d) resulting images by UT, (e) - (h) resulting images by PPT.

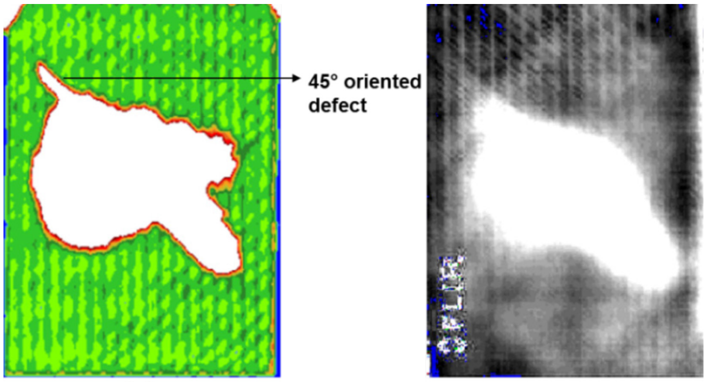

(a) (b)

Figure 6. 4. Worse case scenario for PPT: 45°oriented defect is not detected by PT, (a) resulting image by UT, (b) resulting image by PPT.

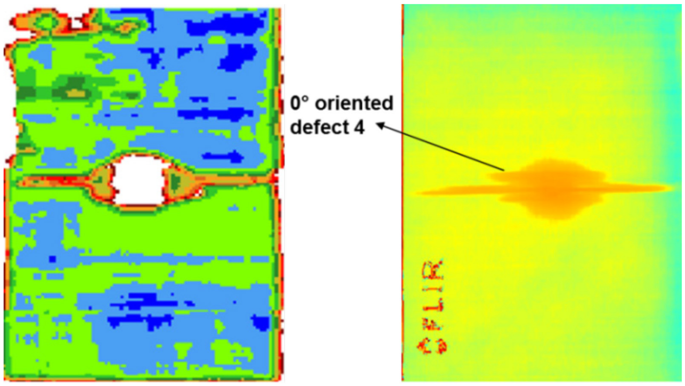

(a) (b)

Figure 6. 5. Worse case scenario for UT: 0°oriented defect is not detected by UT, (a) resulting image by UT, (b) resulting image by PPT.

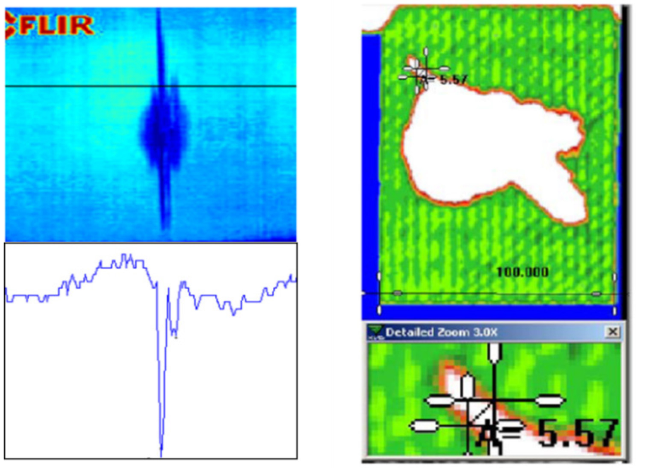

(a) (b)

Figure 6. 6. (a) SNR analysis for a PPT image: SNR = 8 for first peak, SNR = 2 for second peak, (b) example of defect size determination for a UT resulting image.

6.3. PoD Analysis Results

Resulting images obtained by UT and PPT are analyzed and organized into two hit/miss data sets. One denotes detected, zero denotes not detected for the corresponding defect size. Every data set contains 115 pairs of source data (see Appendix A.4). In Chapter 2 four link functions were introduced. It should be noted that the logit (log-odds) model is commonly used in the analysis of binary (hit/miss) data because of its analytical tractability and its close agreement with the cumulative log-normal distribution [1].

In this study, the logit (log-odds) model is used to link the binary data to the size *a* through the probability of either outcome (1 or 0). The logit link function can be written as:

$$\ln(p/1-p) = f(X) = \beta_0 + \beta_1 \cdot \ln(a) \tag{6.1}$$

Because the variance of the transformed function is not constant like it is for an ordinary regression, iteratively reweighted least-squares, a special maximum likelihood method is necessary to estimate the GLM model parameters. With the mh1823 software, Fisher's Scoring algorithm [5] is implemented to obtain the estimate parameter and the variance-covariance matrix. The number of Fisher Scoring iterations is 7 for both UT and PT phase data.

The estimated parameters $\hat{\beta}_0$ and $\hat{\beta}_1$, as well as corresponding variance-covariance matrix for UT data are:

$$\hat{\beta}_0 = \text{-}1.193$$
$$\hat{\beta}_1 = 1.396$$

$$V(\hat{\mu},\hat{\sigma}) = \begin{bmatrix} 0.1993 & -0.1239 \\ -0.1239 & 0.1003 \end{bmatrix}$$

---

[5] In statistics, Fisher's scoring algorithm is a form of Newton's method used to solve maximum likelihood equations numerically.

The estimated parameters $\hat{\beta}_0$ and $\hat{\beta}_1$, as well as corresponding variance-covariance matrix for our PT phase data are:

$$\hat{\beta}_0 = \text{-}2.486$$
$$\hat{\beta}_1 = 2.340$$

$$V(\hat{\mu},\hat{\sigma}) = \begin{bmatrix} 0.4879 & \text{-}0.3438 \\ \text{-}0.3438 & 0.2770 \end{bmatrix}$$

For log-odds model, substitute estimated parameters $\hat{\beta}_0$ and $\hat{\beta}_1$ into Eq. (6.1), we obtained the PoD function:

$$PoD(a) = \frac{\exp(f(X))}{1+\exp(f(X))}$$

(6.2)

where:

$$f(X) = \hat{\beta}_0 + \hat{\beta}_1 \cdot \ln(a) \tag{6.3}$$

As we presented in Chapter 4, the corresponding cumulative log-normal PoD function is expressed as:

$$PoD(a) = \Phi\left(\frac{\ln(a) - \hat{\mu}}{\hat{\sigma}}\right) \tag{6.4}$$

where:

$$\hat{\mu} = \frac{-\hat{\beta}_0}{\hat{\beta}_1}, \qquad \hat{\sigma} = \frac{\pi}{\hat{\beta}_1\sqrt{3}} \tag{6.5}$$

Figure 6.7 compares the log-odds and the log-normal PoD (a) curve fits for UT and PT phase data sets. Obviously, the log-odds and log-normal curve fits are very similar for the data obtained in UT and PPT. At lower values of PoD, less than about 50%, the log-normal curve fit corresponds to a small defect size. But at higher values of PoD, such as the 90% value often used, the log- normal is slightly more conservative, meaning that for a given PoD the corresponding defect size is larger for the log-normal curve fit than the log-odds. Table 6-1 shows the difference between the log-odds and log-normal fits at the 30%, 50% PoD and 90% PoD for UT and PT phase data.

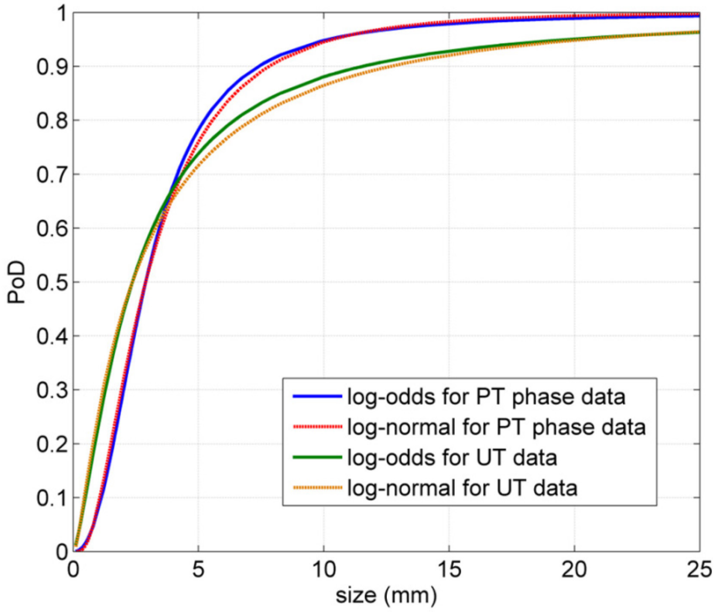

Figure 6. 7. Comparison of log-odds and log-normal PoD curves from UT and PT phase data.

Table 6- 1. A comparison of log-odds and log-normal curve fits.

Technique	**Defect size at 30% PoD (mm)**		**Defect size at 50% PoD (mm)**		**Defect size at 90% PoD (mm)**	
	log-odds	log-normal	log-odds	log-normal	log-odds	log-normal
UT (transmission)	1.27	1.2	2.36	2.36	11.75	12.75
PT (phase data)	2.0	1.92	2.87	2.87	7.40	7.81

Interestingly, from figure 6.7, it is seen that for these specimens, experimental setups and test conditions, PPT leads to detection of smaller size defects than UT at about 65% PoD and higher.

The log-normal PoD curve fits for the data obtained in UT and PPT experiments and their corresponding 95% lower confidence bounds are shown in figure 6.8 and figure 6.9. Obviously, PPT yields smaller a_{90} and $a_{90/95}$ (defect size at 90% PoD with 95% confidence level) values than UT, which indicates PPT has higher inspection capability than UT for the parameters used.

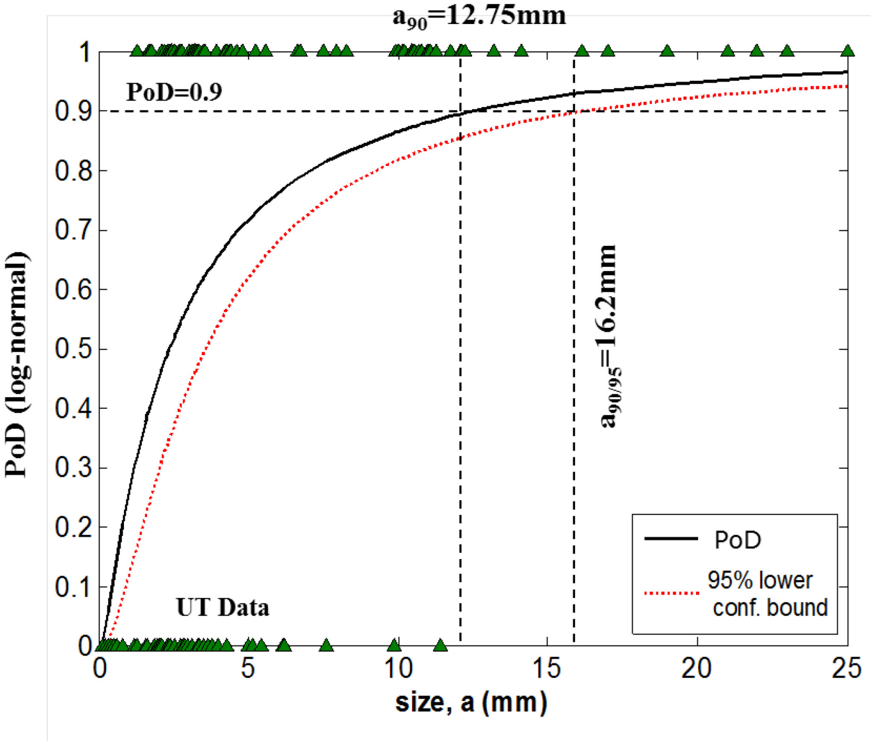

Figure 6. 8. Log-normal PoD curve and the corresponding 95% lower confidence bound for UT data indicate a_{90} value of about 12.75 mm and $a_{90/95}$ value of about 16.2mm for the defect size.

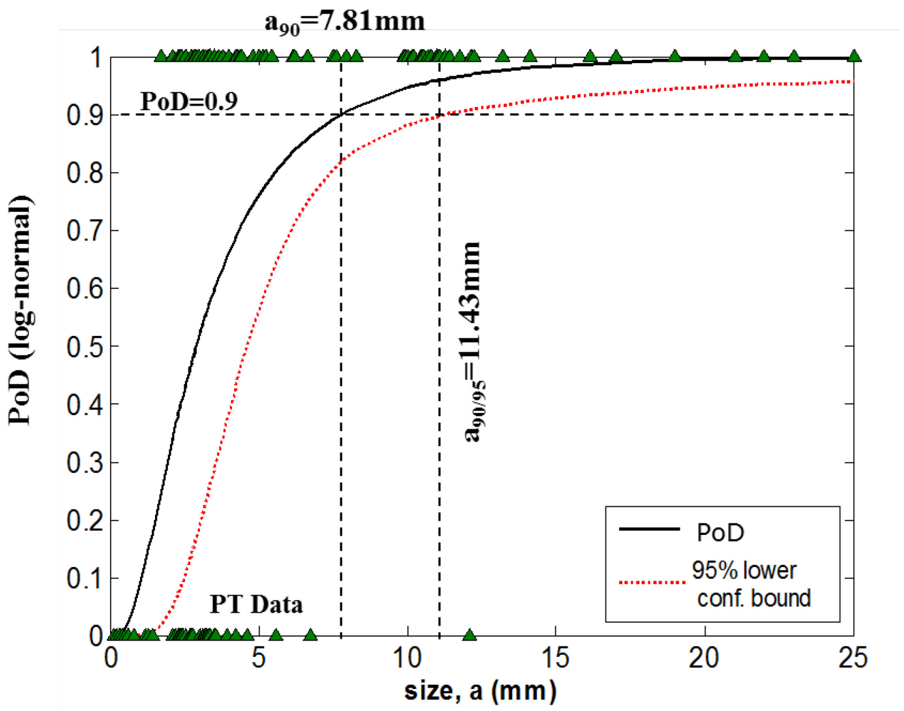

Figure 6. 9. Log-normal PoD curve and the corresponding 95% lower confidence bound for PT phase data indicate a_{90} value of about 7.81 mm and $a_{90/95}$ value of about 11.43mm for the defect size.

6.4. Summary

In this research, the inspection reliabilities for optical PT and ultrasonic C-scan which is widely used in industrial NDT&E, are quantitatively evaluated and compared. PoD curves from optical PT and UT indicate that PT has higher inspection reliability than UT for the parameters used in these inspections. The intent of this research is to advance the wide acceptance of IRT NDT&E techniques out of laboratory, especially in the aerospace industry. Actually, PT can be used as a complement or alternative to UT inspection technology in some practical applications.

Chapter 7. PoD Analysis of Optical PT Images after Automated Segmentation

In the previous chapters, the method used to assess the resulting images to get the hit/miss data is to mark defects on the images by inspector(s). In this chapter[6], a method to extract defects automatically by image segmentation is presented. The images used for segmentation are the raw thermal images and the resulting images obtained by different data processing methods, including FT, 1st D of TSR, WT, DAC and PCT. PoD analysis results after automated segmentation of raw/processed images are compared with the results obtained from manual evaluation. False alarm which is an important aspect of reliability evaluation is also studied.

7.1. Introduction

Recalling from Chapter 4, a CFRP specimen with simulated delaminations (Teflon inserts) was inspected by optical PT. Different post-processing routines were performed, including FT, 1st D of TSR, WT, DAC and PCT. An inspector visually examined the resulting images including the raw PT images to give a qualitative evaluation of the appearance of every defect. The inspector recorded the inspection result in terms of whether or not a flaw was found, and then 6 sets of hit/miss data were obtained. It should be noted that the inspector knows the real location of every defect, which may influence the inspector's interpretation. This finally influences the PoD analysis result. Actually, in the design of a NDT&E reliability experiments, human factor including capability and mental acuity of the inspector is an important aspect that needs to be considered. Sometime, several inspectors instead of one inspector are employed to interpret the response or the resulting image. Compared with thermal image, the segmented image provides visualized information about true defects and false alarms. Analyzing the binary images after automated segmentation would be obviously easier for the inspector.

---

[6] The major content of this chapter has been presented at the 16th International Symposium on Applied Electromagnetics and Mechanics (ISEM), Quebec, Canada, July 31 to August 2, 2013.

7.2. Procedure of Automated Segmentation

In this section, we present an evaluation method dedicated to automatically segment input thermal images. Assume that N raw images have been recorded by the thermal camera as times: t_1, t_2, … , t_N. The evaluation method is applied on input raw images and it is composed of:

- A data processing step aiming into improving the image contrast and reducing the noise, thus improving the defect detection capability [73].
- A segmentation procedure based on the use of the Contrast Noise Ratio (CNR) image instead of the thermal image, this allows removing the fluctuation in values of pixels corresponding to defect [79-81]. In fact, due to the variation in phase, defects appear bright in some frames and dark in other frames. By using the CNR image, all suspicious regions where a gradient in the grey values occur will appear as bright regions. CNR for every pixel in a thermal image is calculated by:

  $$\mathrm{CNR} = \frac{\text{average value over a } 3 \times 3 \text{ pixels area} - \text{average value of reference area}}{\text{standard deviation of the reference area}}$$

  It should be noted that the whole thermal image is selected as the reference area to avoid the subjective selection of defect-free-zone.
- After computing the CNR image, a threshold is computed (Otsu's method [83]) and applied on the pixels of the image. The algorithm assumes that the image to be segmented contains two classes of pixels (e.g. foreground and background) then calculates the optimum threshold separating those two classes so that their combined spread (intra-class variance) is minimal [82-84]. This results in a binary image where pixels are set as 0 (background) and 1 (foreground).
- The last step of the segmentation procedure is the fusion of all the binary images corresponding to the input raw images recorded at t_1, t_2, … , t_N. The number of true defects and false alarms can be simply computed on the resulting final image. The flow-process diagram of the procedure of automated segmentation is shown in figure 7.1.

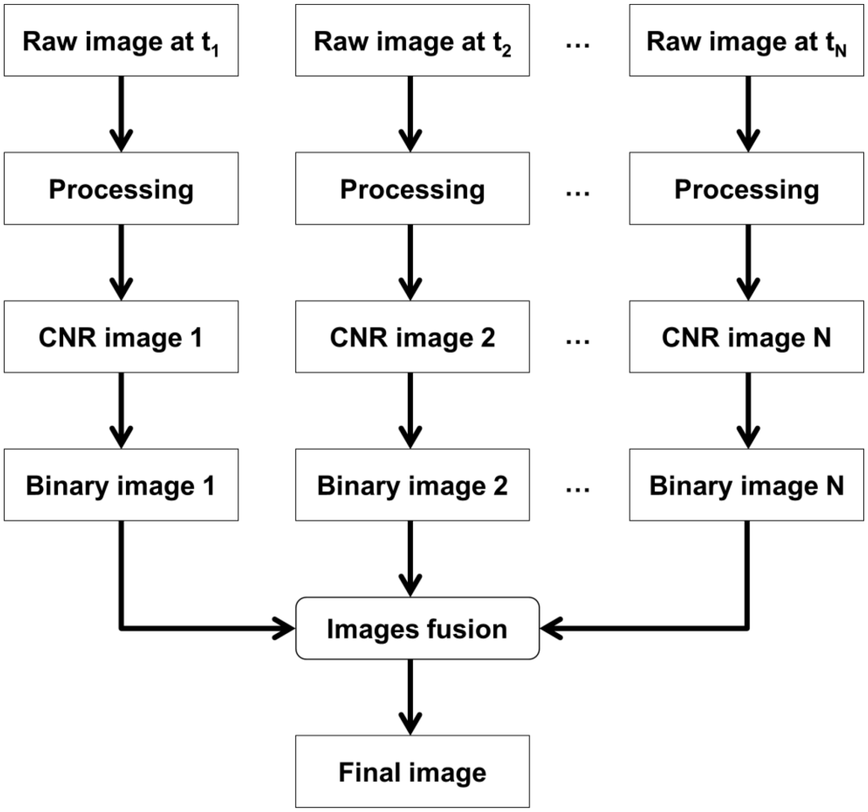

Figure 7. 1. The flow-process diagram of the procedure of automated segmentation.

7.3. Binary Images after Automated Segmentation

The evaluation method is tested on a CFRP specimen including 25 Teflon inserts simulating delamination. Recalling from Chapter 4, the specimen was tested from both sides giving a total 50 inspection targeted sites (flaws with different aspect ratio (Dimension / depth) values, from 3/1.8 to 15/0.2). The experiment configuration and parameters used in the data processing manipulations are as described in Chapter 4. First, the thermal images obtained from 1st D of TSR manipulation which is slightly more effective than other routines (FFT, WT and DAC) for our specimen, are evaluated to automatically segment the defects. The 1st derivative images (front side inspection) at different times obtained by TSR and corresponding automatically segmented images are presented in figure 7.2. The binary fusion image is the result of the segmentation of 1st derivative images at time t_1 = 0.075s, t_2 = 0.1s and t_3 = 0.35s. The fusion image contains 22 true defects and 8 false alarms.

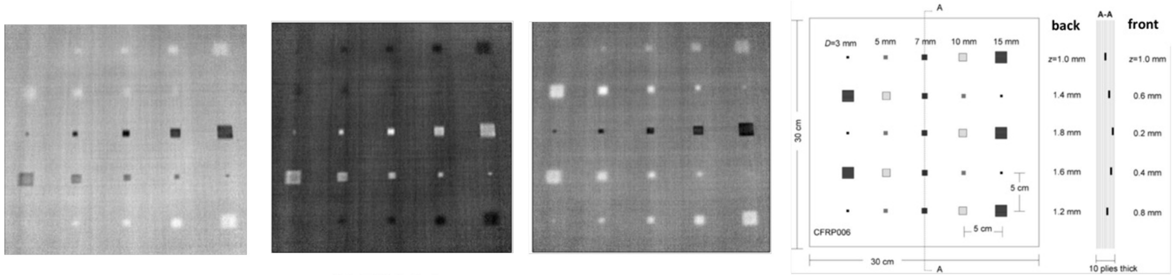

(a) TSR 0.075s (b) TSR 0.1s (c) TSR 0.35s

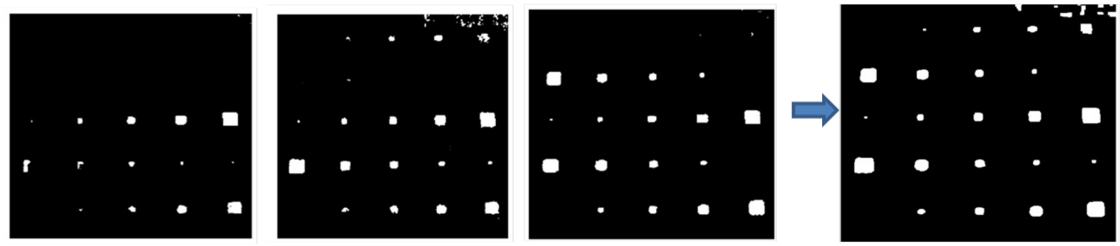

(d) Segmented image 0.075s (e) Segmented image 0.1s (f) Segmented image 0.35s (g) Fusion image

Figure 7. 2. (a) - (c) 1^{st} derivative images (front side inspection) at different times obtained by TSR, (d) - (f) corresponding automated segmentation, (g) fusion image of 3 segmented images.

The fusion images for the raw and resulting images processed by 1^{st} D of TSR, PPT, PCT, WT and DAC are shown in figure 7.3.

7.4. PoD Analysis Results after Automated Segmentation

Table 7-1 shows the rough comparison of manual evaluation and automated segmentation for the inspection results by non-processed and different data processing techniques. The hit/miss source data obtained from automated segmentation which will be used for PoD analysis is in Appendix A. 5.

From table 7-1, it is obvious that the detection rate of manual evaluation is greater than automated segmentation for the same thermal images (raw or after different data processing manipulation). Inspectors familiar with thermal images can identify more defects relying on their experiences.

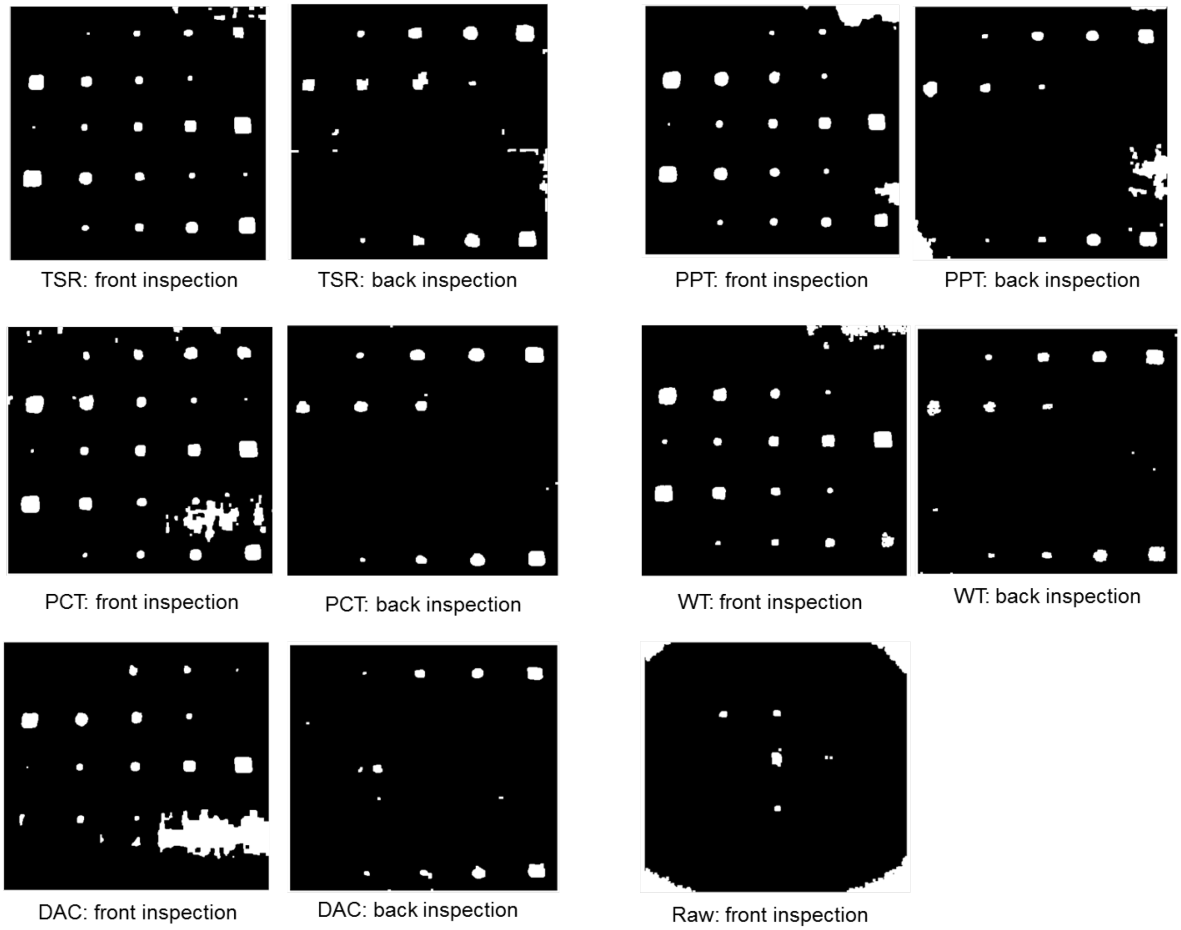

TSR: front inspection
TSR: back inspection
PPT: front inspection
PPT: back inspection
PCT: front inspection
PCT: back inspection
WT: front inspection
WT: back inspection
DAC: front inspection
DAC: back inspection
Raw: front inspection

Figure 7. 3. Fusion images for the raw and resulting images processed by 1st D of TSR, PPT, PCT, WT and DAC.

Table 7- 1. Rough comparison of manual evaluation and automated segmentation.

Data processing	Manual evaluation		Automated segmentation		
	Number of inserts detected	Detection rate	Number of inserts detected	Detection rate	False calls
1st D TSR	40	80%	34	68%	19
PCT	38	76%	33	66%	22
PPT	36	72%	30	58%	14
WT	35	70%	30	58%	10
DAC	30	60%	24	48%	15
RAW	19	38%	5	10%	5

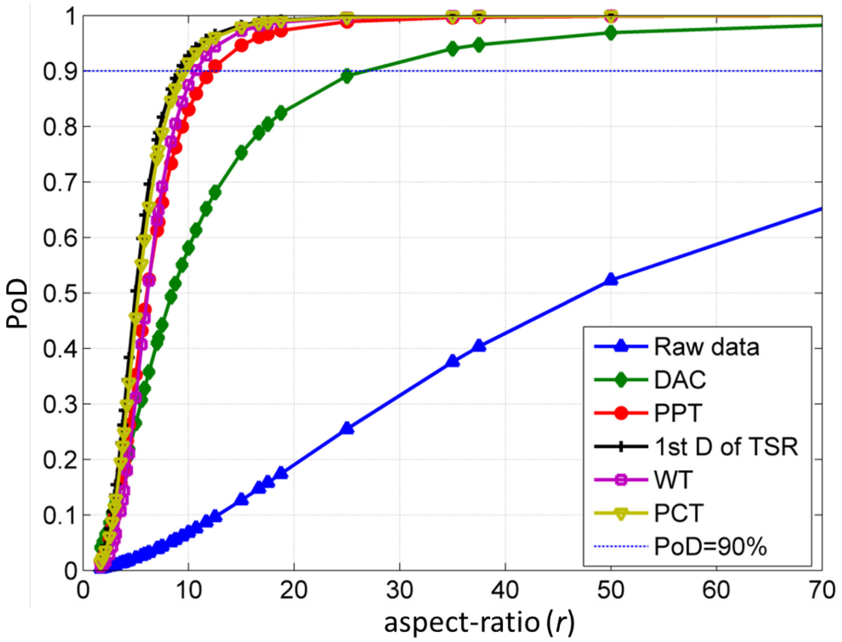

Figure 7. 4. PoD curves of automated segmentation result.

Table 7- 2. r_{90} and $r_{90/95}$ values obtained from manual evaluation and automated segmentation.

Data processing	Manual evaluation		Automated segmentation		
	r_{90}	$r_{90/95}$	r_{90}	$r_{90/95}$	False calls
TSR 1st D	6.60	11.50	9.07	15.39	19
PCT	6.64	10.91	9.51	16.11	22
PPT	7.37	11.44	12.13	22.77	14
WT	9.20	17.63	10.68	17.82	10
DAC	10.39	16.93	26.06	98.84	15
RAW	17.06	30.04	∞	∞	5

Log-odds model was employed to plot the PoD curves of manual evaluation result (as depicted in figure 4.14) and PoD curves of automated segmentation result, as shown in figure 7.4.

The 95% lower confidence bound for each data processing methods were also calculated. Table 7-2 shows the defect aspect ratio with 90% PoD (r_{90}) and the defect aspect ratio for which a 90% PoD is reached at 95% confidence level ($r_{90/95}$). It should be noted that for the raw thermal image the defect aspect ratio with 90% PoD cannot be determined from the PoD curve because only 5 out of 50 defects were identified.

From the table 7-2, we can see the high inspection capability is accompanied by high false call rate. Besides considering inspection capability, the false positive is also an important aspect in NDT reliability demonstration. The balance of the false positive rate and detection sensitivity is one of the most concerns in industry, which should be determined according to the actual application requirement.

7.5 Summary

Both manual evaluation and automated segmentation results prove that using 1st derivative of TSR and PCT are more effective than other routines in this experiment. The detection rate of manual evaluation is greater than automated segmentation for the same thermal images (raw or after different data processing manipulation). Inspectors familiar with thermal images can identify more defects relying on their experiences.

Conclusions and Future Prospects

In this thesis, PoD analysis of both continuous response data and hit/miss data were carried out based on the optical PT inspection results of a CFRP specimen with embedded material simulating delaminations. For continuous response data, it has become a common practice to use *log(â)* vs*. log(a),* in the traditional NDT reliability demonstration, especially for flaw length as determined by ultrasonic NDT. However, we have noted that sometimes Cartesian *â* vs. *log(a)* is a better model for the IRT data set. In this regard, the model should be chosen according to the data set rather than experiences for IRT data, because most of the experiences mentioned in the literature are from PoD analysis of classical NDT methods. In Chapter 4, we presented the quantitative comparison of five commonly used data enhancement techniques, including FT, 1st D of TSR, WT, DAC, and PCT, as well as raw thermal images, by observing PoD curves which provide detailed and intuitive information.

As we know, there are different heating forms and patterns in optical IRT. Pulsed and modulated heating are among the most popular heating forms. In Chapter 5, a new attempt was made to inspect aluminum foam material by optical IRT techniques. PoD curves were plotted to quantitatively evaluate the two optical thermographic techniques: LT and PT, on aluminum foam material. Compared with LT, the experimental results showed that PT with long heating pulse and effective data processing manipulations could achieve comparable and even better results for the material of relatively low thermal conductivity.

The inspection reliability and capability of IRT technique compared with traditional NDT&E methods is an issue of great concern. In Chapter 6, we presented PoD analysis results by UT and PT for a set of CFRP specimen with impact damages. The quantitative comparison showed that PT has higher inspection reliability than UT in some inspections.

In Chapter 7, a method to extract defects automatically by image segmentation was presented. The images used for segmentation were the raw thermal images and the resulting images obtained by different data processing methods, including FT, 1st D of TSR, WT, DAC and PCT. PoD analysis results after automated segmentation of raw/processed images were compared with the results obtained from manual evaluation which were presented in Chapter 4. False alarm which is an important aspect of reliability evaluation was also studied.

Generally, we have done exhaustive study of inspection reliability and capability for IRT NDT&E technique through PoD analysis. Part of the results were compared with traditional NDT&E method ultrasonic C-scanning.

Our work, together with other related experimental works will advance the wide acceptation of IRT NDT&E out of laboratory, especially in the aerospace industry, since the reliability and capability of IRT NDT&E system is quantitatively evaluated, as traditional NDT&E approaches. Moreover, our work is useful for optimizing a NDT&E system and an inspection procedure, such as choosing excitation forms (or modes), parameter settings and the post data processes for a specific inspection object.

There remain some work to do to systematically evaluate the reliability and capability of an IRT system. In the future, we will do more work about the false alarm analysis. In addition, because the probability of detection is sensitive to flaw characteristics, and most available specimens could not simulate the real flaws with accuracy, collecting inspection results of manufactured or service induced defects and implementing the PoD analysis for them is also an important part of my project. However, due to the lack of opportunity to get real defects generated during the manufacturing process or service, we had to leave this for further study.

Summary of contributions

1. **Yuxia Duan**, Stefanie Hübner, Clemente Ibarra-Castanedo, Xavier Maladague, "*Quantitative Evaluation of Optical Pulsed and LT for Aluminum Foam Material*".
   Journal of Infrared Physics and Technology, vol. 60, pp. 275 - 280, 2013.
2. **Yuxia Duan,** Ahmad Osman, Clemente Ibarra-Castanedo, Ulf Hassler, Xavier Maldague, "*A comparative study on manual PoD analysis and automated evaluation of thermography images of composite materials*".
   The 16th International Symposium on Applied Electromagnetics and Mechanics (ISEM), Quebec, Canada, July 31 to August 2, 2013.
3. S. Huebner, U. Hassler, **Y. Duan**, A. Osman, X. Maldague, "*Study of the Influence of Corrosion on Material Properties on Aluminum Foams with Computed Tomography and Thermography*".
   The 4th International Symposium on NDT in Aerospace, Augsburg, Germany on 13-15, November 2012.
4. **Y. Duan**, P. Servais, M. Genest, C. Ibarra-Castanedo, and X. P. V. Maldague, "*ThermoPoD: A Reliability Study on Active IRT for the Inspection of Composite Materials*".
   Presented on International Conference on Materials and Reliability 2011 (ICMR 2011), held in Busan, Korea, Nov. 20-22, 2011 (Invited lecture), and published in Journal of Mechanical Science and Technology, vol. 26 (7), pp. 1985 - 1991, 2012.
5. Reza Shoja Ghiass, **Yuxia Duan**, Kira Peycheva, Xavier Maldague, "*Inspection of Glass Fiber Reinforced Plastic (GFRP) Using Near/Shortwave Infrared and Ultrasound/Optical Excitation thermography*".
   International workshop of Smart Materials, Structures & NDT in Aerospace, 2- 4 November 2011, Montreal, Quebec, Canada.
6. Ibarra-Castanedo C., Servais P., Genest M., **Duan Y.**, Bendada A. and Maldague X., "*Potentials and Limits of Active Infrared Vision for the Non-destructive Assessment of Composites*".
   International Conference on Experimental Mechanics 2010 (ICEM 2010), 29th November -1st December 2010, Legend Hotel, Kuala Lumpur, Malaysia (Invited lecture).
7. P. Servais, C. Ibarra-Castenado, X. Maldague, Y. Gélébart, **Y. Duan**, "*PoD for in Field Thermal Non-destructive Testing of Aircraft Composite Structures*".
   The 10th International Conference on Quantitative IRT, July 27 - 30, 2010, Québec (Canada), pp. 425 - 426.
8. **Yuxia Duan**, Cunlin. Zhang, Xiaoli Li, Naiming Wu, Xavier Maldague, "*IRT and ultrasonic C-scan for nondestructive evaluation of aerospace materials: A comparative study*".

The 10th International Conference on Quantitative IRT, July 27 - 30, 2010, Québec (Canada), pp.713 - 719.

Bibliography

[1] A. P. Berens, “NDE reliability data analysis”, in Metals Handbook, 9th ed., vol. 17, pp. 1389 -1470, Ohio: ASM International, 1989.

[2] W. D. Rummel, “Probability of detection as a quantitative measure of nondestructive testing end-to-end process capabilities”, Materials Evaluation, vol. 56, pp. 29 - 35, 1998.

[3] P. G. Heasler, S. R. Doctor and T. T. Taylor, “Quantifying inspection performance using relative operating characteristic curves”, presented at the International Conference on NDE in the Nuclear and Pressure Vessel Industries, pp. 481, 1990.

[4] C. Müller, M. Elaguine, C. Bellon, U. Ewert, U. Zscherpel, M. Scharmach, B. Redmer, H. Ryden and U. Ronneteg, “POD (probability of detection) evaluation of NDT techniques for Cu-canisters for risk assessment of nuclear waste encapsulation”, ECNDT, pp. 1 - 22, 2006.

[5] P. Servais, C. Ibarra-Castanedo, X. Maldague and Y. Gélé-bart, “Probability of detection for in field thermal non de-structive testing of aircraft composite structures (ABSTRACT)”, the 10th International Conference on Quantitative Infrared Thermography, pp. 245 - 246, Quebec, Canada, July 27 - 30, 2010.

[6] G. Georgiou, “PoD curves, their derivation, applications and limitations ”, Insight - Non-Destructive Testing and Condition Monitoring, vol. 49(7), pp. 409 - 414, July 2007.

[7] US Air Force Aeronautical Systems Center, Military Handbook 2009: Non-Destructive Evaluation System Reliability Assessment (Department of Defence Handbook).

[8] C. Ibarra-Castanedo, F. Galmiche, A. Darabi, M. Pilla, M. Klein, A. Ziadi, S. Vallerand, J. F. Pelletier and X. Maldague, “Thermographic nondestructive evaluation: overview of recent progress”, in SPIE -Thermosense XXV, pp. 450 - 459, 2003.

[9] J. DiMambro, D. M. Ashbaugh, X. Han, L. D. Favro, J. Lu, Z. Zeng, W. Li,G. M. Newaz and R. L. Thomas, “The potential of sonic IR to inspect aircraft components traditionally inspected with fluorescent penetrant and or magnetic particle inspection in the field”, presented at the Review of Progress in Quantitative Nondestructive Evaluation Quantitative, pp. 536 - 543, 2005.

[10] J. DiMambro, D. M. Ashbaugh, C. L. Nelson and F. W. Spencer, “Sonic infrared (IR) imaging and fluorescent penetrant inspection probability of detection (POD) comparison”, Review of Quantitative Nondestructive Evaluation, vol. 26, pp. 463 - 470, 2007.

[11] Y. Guo and F. R. Ruhge,“Comparison of detection capability for acoustic thermography, visual inspection and fluorescent penetrant inspection on gas turbine components”, Review of Quantitative Nondestructive Evaluation, D. O. Thompson and D. E. Chimenti (Eds.), American Institute of Physics, vol. 28, pp. 1848 - 1854, 2009.

[12] J. DiMambro, “Quantitative evaluation of emerging infrared thermography technologies for aerospace applications (Chapter 15)”, in Ultrasonic and Advanced Methods for Nondestructive Testing and Material Characterization, C. H. Chen (Ed.), pp. 349 - 367, 2006.

[13] J. DiMambro, K. A. Rackow, D. P. Roach, S. M. Shepard and T. Ahmed, “A composite honeycomb probability of detection (POD) experiment using an uncooled infrared camera for pulsed thermography”, 49th Annual Air Transport Association (ATA) NDT Forum, Ft. Worth North, TX, USA, October 16 -18, 2006.

[14] A. J. Hodge and J. L. Walker, “Probability of detection study on impact damage to honeycomb composite structure using thermographic inspection”, Proceedings of 40th International SAMPE Technical Conference (ISTC), Memphis, TN - September 8 - 11, 2008.

[15] X. P. V. Maldague, Theory and practice of infrared technology for nondestructive testing, New York: Wiley, 2001.

[16] X. P. V. Maldague, P. O. Moore, Infrared and Thermal Testing, in American Society for Nondestructive Testing : Nondestructive Testing Handbook, vol. 3, Third ed., 2001.

[17] C. Ibarra-Castanedo, M. Genest, S. Guibert, J.-M. Piau, X. P. V. Maldague and A. Bendada, “Inspection of aerospace materials by pulsed thermography, lock-in thermography and vibrothermography: A comparative study”, in SPIE - ThermosenseXXIX, vol. 6541, 2007.

[18] H. S. Carllaw and J. C. Jaeger, Conduction of heat in solids, 2nd ed., Oxford: Clarendon Press, 1986.

[19] X. P. V. Maldague and S. Marinetti, “Pulse phase infrared thermography”, Journal of Applied Physics, vol. 79, pp. 2694 - 2698, 1996.

[20] R. Bracewell, The fourier transform and its applications. McGraw-Hill, USA, 1965.

[21] E. O. Brighman, The fast fourier transform. Englewood Cliffs, N. J.: Prentice-Hall, Inc., 1974.

[22] K. R. Castleman, Digital image processing. Upper Saddle River, N. J.: Prentice-Hall, 1996.

[23] J. W. Cooley and J. W. Tukey, "An algorithm for the machine calculation of complex fourier series", Mathematics of Computation, vol. 19, pp. 297 - 301, 1965.

[24] C. Liu, L. Czuban, P. Bison, E. Grinzato, S. Marinetti and X. Maldague, "Complex-surfaced objects: Effects on phase and amplitude images in pulsed phase thermography", presented at the 12th Asia-Pacific Conference on Non-Destructive Testing, Nov. 2006.

[25] C. Ibarra-Castanedo, "Quantitative subsurface defect evaluation by pulsed phase thermography: depth retrieval with the phase", Ph.D. thesis, Université Laval, 2005.

[26] C. Ibarra-Castanedo and X. P. V. Maldague, "Interactive methodology for optimized defect characterization by quantitative pulsed phase thermogaraphy", Research in Nondestructive Evaluation, vol. 16, pp. 175 - 193, 2005.

[27] G. Zauner, G. Mayr and G. Hendorfer, "Application of wavelet analysis in active thermography for nondestructive testing of CFRP composites", in SPIE - Wavelet Applications in Industrial Processing IV, vol. 6383, 2006.

[28] S. M. Shepard, T. Ahmed, B. A. Rubadeux, D. Wang and J. R. Lhota, "Synthetic processing of pulsed thermographic data for inspection of turbine components", in British Inst. of NDT. vol. 43, pp. 587 - 589, September, 2001.

[29] S. Shepard, J. Lhota, D. Wang, B. Rubadeux and T. Ahmed, "Depth and spatial resolution enhancement using thermographic signal reconstruction", in the 6th Far-East Conference on NDT-FENDT02, pp. 279 - 284, Tokyo, Japan, Oc-tober, 2002.

[30] S. Shepard, J. R. Lhota, B. A. Rubadeux, T. Ahmed and D. Wang, "Enhancement and reconstruction of thermographic NDT data", Proceedings of SPIE, vol. 4710, pp. 531 - 535, 2002.

[31] S. Shepard, J.R. Lhota, B.A. Rubadeux, D. Wang and T. Ahmed, "Reconstruction and enhancement of active thermographic image sequences", Optical Engineering, Vol. 42 (5), pp. 1337 -1342, May 2003.

[32] X. Wang, "Pulse-echo thermal wave imaging of metals and composite", Master Thesis, Wayne State University, 2001.

[33] G. Kaiser, A friendly guide to wavelets, Boston, 1994.

[34] F. R. Galmiche, "Application of wavelet transform for the nondestructive evaluation of materials by pulsed phase thermography", PhD thesis, Université Laval, 2005.

[35] Matlab Wavelet Toolbox- User's Guide Ver.4, Mathworks Inc.

[36] F. Galmiche and X. Maldague, "Depth defect retrieval using the wavelet pulsed phased thermography", in International Conference on Quantitative Infrared Thermography-QIRT 2000, Eurotherm Seminar 64, pp. 194 - 199, Reims, France, 2000.

[37] F. Galmiche, X. Maldague, S. Valler and Jean-Pierre Couturier, "Pulsed phased thermography with the wavelet transform", in AIP Conference-Review of Progress in Quantitative Nondestructive Evaluation, pp. 609 - 616, 2000.

[38] H. D. Benítez, C. Ibarra-Castanedo, A. Bendada, X. Maldague, H. Loaiza and E. Caicedo, "Definition of a new thermal contrast and pulse correction for defect quantification in pulsed thermography", Infrared Physics & Technology, vol. 51, pp. 160 - 167, 2008.

[39] M. Pilla, M. Klein, X. Maldague and A. Salerno, "New absolute contrast for pulsed thermography", Proceedings of 6th International Conference on Quantitative Infrared Thermography, pp. 53 -58, Dubrovnik, Croatia, 2002.

[40] S. Marinetti, E. Grinzato, P.G. Bison, E. Bozzi, M. Chimenti, G. Pieri and O. Salvetti, "Statistical analysis of IR thermographic sequences by PCA", Infrared Physics &Technology, vol. 46, pp. 85 - 91, 2004.

[41] Rajic N, "Principal component thermography for flaw contrast enhancement and flaw depth characterization in composite structures", Composite Structure, vol. 58, pp. 521 - 528, 2002.

[42] C. Ibarra-Castanedo, A. Bendada and X. Maldague, "Thermographic image processing for NDT", in IV Conferencia Panamericana de END Buenos Aires, pp. 1 - 12, October, 2007.

[43] C. Ibarra-Castanedom, D. A. González, F. Galmiche, A. Bendada and X. P. Maldague, "On signal transforms applied to pulsed thermography (Chapter 5)", Recent Research Developments in Applied Physics, vol. 9, pp. 101 - 127, 2006.

[44] J. C. Krapez, "Compared performances of four algorithms used for modulation thermography", presented at the 4th Conference on Quantitative InfraRed Thermography - QIRT, Eurotherm Seminar 60, pp. 148 - 153, Lodz, Pologne, 1998.

[45] D. Wu and G. Busse, “Lock-in Thermography for NonDestructive Evaluation of Materials”, Rev. Gén. Therm, vol. 37, pp. 693 - 703, 1998.

[46] G. Busse, D. Wu, and W. Karpen, “Thermal Wave Imaging with Phase Sensitive Modulated Thermography”, Journal of Applied Physics, vol. 71, pp. 3962 - 3965, 1992.

[47] L. D. Favro and X. Han, “Thermal wave materials characterization and thermal wave imaging”, in Processing and Manufacuring, ASNT TONES, pp. 399 - 415, 1998.

[48] G. Busse and A. Rosencwaig, “Subsurface imaging with photoacoustics”, Applied Physics Letters, vol. 36, pp. 815 - 816, 1980.

[49] R. L. Thomas, J.J. Pouch, Y.H. Wong, L.D. Favro and P.K. Kuo, A. Rosencwaig, Subsurface, “Subsurface flaw detection in metals by photoacustic microscopy”, Journal of Applied Physics, vol. 51, pp. 1152 - 1156, 1980.

[50] A. Dillenz , T. Zweschper and G. Busse, “Progress in ultrasound phase thermography”, in SPIE - The International Society for Optical Engineering, Thermosense XXVIII, pp. 574 - 579, Orlando, FL, 2001.

[51] L. D. Favro, Xiaoyan Han, Ouyang Zhong, Sun Gang, Sui Hua, and R.L Thomas, “Infrared imaging of defects heated by a sonic pulse”, Review of Scientific Instruments, pp. 2418, 2000.

[52] T. Zweschper, G. Riegert, A. Dillenz and G. Busse, “Frequency modulated elastic wave thermography”, in SPIE - TheInternational Society for Optical Engineering, Thermosense XXV, pp. 386 - 391, Orlando, FL, 2003.

[53] S. D. Holland, “First measurements from a new broadband vibrothermography measurement system”, in Review of Quantitative Nondestructive Evaluation, vol. 26, pp. 478 - 483, 2007.

[54] L. Schaefer, “Reliability for NDT Tutorial: POD Basic”, presented at the 4th European-American Workshop on Reliability of NDE, Berlin, Germany, June, 2009, <http://www.ndt.netindex.php?id8311>.

[55] U. Schnars and A. KÜCK, “Application of POD analysis at airbus”, at 4th European-American Workshop on Reliability of NDE, Berlin, Germany, June, 2009.

[56] S. W. Floyd, “The calculation and use of confidence bounds in POD models”, Review of Quantitative Nonde-structive Evaluation, vol. 26, pp. 1791 - 1798, 2007.

[57] D. S. Forsyth and A. Fahr, “An evaluation of probability of detection statistics”, in Airframe Inspection Reliability under Field/Depot Conditions, NATO Research and Technology Organisation, Neuilly-sur-Seine Cedex, France, November, 1998.

[58] A. P. Berens and P. W. Hovey, Characterization of NDE Reliability. New York: Plenum Press, 1982.

[59] A. Fahr, D. Forsyth and M. Bullock, “A comparison of probability of detection (POD) data determined using different statistical methods”, NRC IAR LTR-ST-1947, December, 1993.

[60] A. Ralston, A First Course in Numerical Analysis, McGraw-Hill, 1965.

[61] A. P. Berens and P. W. Hovey, “Flaw detection reliability criteria”, in Methods and Results, AFWAL-TR-84-4022, Air Force Wright-Aeronautical Laboratories, Wright-Patterson Air Force Base. vol. I, 1984.

[62] R. C. H. Cheng and T. C. Iles, “Confidence bands for cumulative distribution functions of continuous random variables”, Technometrics, vol. 25, pp. 77 - 86, February, 1983.

[63] R. C. H. Cheng and T. C. Iles, “One sided confidence bands for cumulative distribution functions”, Technometrics, vol. 32, pp. 155 - 159, May, 1988.

[64] W. Q. Meeker and L. A. Escobar, “Teaching about approximate confidence regions based on maximum likelihood estimation”, The American Statistician, vol. 49, pp. 48 - 53, February, 1995.

[65] J. Brown, “PoD Test”, Materials Evaluation, pp. 421 - 426, April, 2012.

[66] Y. Feng, H. Zheng, Z. Zhu and F. Zu, “The microstructure and electrical conductivity of aluminum alloy foams”, Materials Chemistry and Physics, vol. 78 (1), pp. 196 - 201, 2003.

[67] A. Paul and U. Ramamurty, “Strain rate sensitivity of a closed-cell aluminum foam”, Materials Science and Engineering: A, vol. 281(1-2), pp. 1 - 7, 2000.

[68] J. Banhart, H. Stanzick, L. Helfen, T. Baumbach and K. Nijhof, “Real-time x-ray investigation of aluminium foam sandwich production”, Advanced Engineering Materials, vol. 3 (6), pp. 407 - 411, 2001.

[69] E. Maire, A. Fazekas, L. Salvo, R. Dendievel, S. Youssef, P. Cloetens and J.M. Letang, "X-ray tomography applied to the characterization of cellular materials. Related finite element modeling problems”, Composites Science and Technology, vol. 63, pp. 2431 - 2443, 2003.

[70] X. P.V. Maldague, “Introduction to NDT by active infrared thermography”, Materials Evaluation, vol. 6 (9), pp. 1060 - 1073, 2002.

[71] A. Gleiter, C. Spießberger and G. Busse, “Lockin-thermography with optical or ultrasound excitation”, in: 10th International Conference of the Slovenian Society for Non-Destructive Testing, pp. 447 - 454, Ljubljana, Slovenia, September, 2009.

[72] G. Giorleo and C. Meola, “Comparison between pulsed and modulated thermography in glass–epoxy laminates”, NDT & E International, vol. 35 (5), pp. 287 - 292, 2002.

[73] Y. Duan, P. Servais, M. Genest, C. Ibarra-Castanedo and X. Maldague, “ThermoPoD: A reliability study on active infrared thermography for the inspection of composite materials”, Journal of Mechanical Science and Technology, vol. 26 (7), pp.1985 - 1991, 2012.

[74] R. J. Ball and D. P. Almond, “The detection and measurement of impact damage in thick carbon fiber reinforced laminates by transient thermography”, NDT&E international, vol. 31(3), pp. 165 - 173, 1998.

[75] C. C. Tsao and H. Hocheng, “Computerized tomography and C-Scan for measuring delamination in the drilling of composite materials using various drills”, International Journal of Machine Tools & Manufacture, vol. 45, pp. 1282 - 1 287, 2005.

[76] C. Meola, G. M. Carlomagno, A. Squillace and A. Vitiello, “Non-destructive evaluation of aerospace materials with lock-in thermography”, Engineering Failure Analysis, vol. 13, pp. 380 - 388, 2006.

[77] W. Xun, W. Jin, C. Zhang and J. Shen, “Actuality & evolvement of infrared thermal wave nondestructive imaging technology”, Nondestructive Testing, vol. 26(10), pp. 497 - 501, 2004.

[78] D. Bates, G. Smith, D. Lu and J. Hewitt, “Rapid thermal non-destructive testing of aircraft components”, Composites:Part B, pp. 175 - 185, 2000.

[79] X. Song, B. W. Pogue, S. Jiang, M. M. Doyley, H. Dehghani, T. D. Tosteson, and K. D. Paulsen, “Automated region detection based on the contrast-to-noise ratio in near-infrared tomography”, Applied Optics, vol. 43, pp. 1053 - 1062, 2004.

[80] W. A. Edelstein, P. A. Bottomley, H. R. Hart, and L. S. Smith, Signal, noise and contrast in nuclear magnetic resonance (NMR) imagingJournal of Computer Assisted Tomography, vol.7 (3), pp. 391 - 401, 1983.

[81] T. Varghese and J. Ophir, “An analysis of elastographic contrast-to-noise ratio”, Ultrasound in Medicine & Biology, vol. 24 (6), pp. 915 - 924, 1998.

[82] M. Sezgin and B. Sankur, “Survey over image thresholding techniques and quantitative performance evaluation”, Journal of Electronic Imaging, vol. 13 (1), pp. 146 - 165, 2004.

[83] N. Otsu, “A threshold selection method from gray-level histograms”, IEEE Transaction on System, Man, and Cybernetics, vol. 9 (1), pp. 62 - 66, 1979.

[84] P. Liao, T. Chen and P. Chung, “A Fast Algorithm for Multilevel Thresholding”, Journal of Information Science and Engeering, vol. 17 (5), pp. 713 - 727, 2001.

Appendix A. Source Data for PoD Analysis

A.1. Response Data from PPT for the Inspection of a CFRP Specimen (Chapter 4)

n	dimension (D/mm)	depth (d/mm)	aspect-ratio (r)	maximum phase contrast (Δϕ/rad)
1	3	1.8	1.67	0.0001
2	3	1.6	1.88	0.0001
3	3	1.4	2.14	0.0001
4	3	1.2	2.50	0.0108
5	5	1.8	2.78	0.0001
6	3	1	3.00	0.0001
7	3	1	3.00	0.0137
8	5	1.6	3.13	0.0001
9	5	1.4	3.57	0.018
10	3	0.8	3.75	0.0078
11	7	1.8	3.89	0.0001
12	5	1.2	4.17	0.0195
13	7	1.6	4.38	0.0001
14	3	0.6	5.00	0.0193
15	5	1	5.00	0.0161
16	5	1	5.00	0.0298
17	7	1.4	5.00	0.025
18	10	1.8	5.56	0.001
19	7	1.2	5.83	0.0313
20	5	0.8	6.25	0.0339
21	10	1.6	6.25	0.007
22	7	1	7.00	0.0391
23	7	1	7.00	0.0476
24	10	1.4	7.14	0.0202
25	3	0.4	7.50	0.0282
26	5	0.6	8.33	0.0519
27	10	1.2	8.33	0.0438
28	15	1.8	8.33	0.001
29	7	0.8	8.75	0.0535
30	15	1.6	9.38	0.013
31	10	1	10.00	0.0487
32	10	1	10.00	0.0588
33	15	1.4	10.71	0.0249
34	7	0.6	11.67	0.0698
35	5	0.4	12.50	0.0683

36	10	0.8	12.50	0.0697
37	15	1.2	12.50	0.0363
38	3	0.2	15.00	0.0478
39	15	1	15.00	0.0453
40	15	1	15.00	0.0493
41	10	0.6	16.67	0.0813
42	7	0.4	17.50	0.0845
43	15	0.8	18.75	0.0674
44	15	0.6	25.00	0.0691
45	5	0.2	25.00	0.1126
46	10	0.4	25.00	0.0736
47	7	0.2	35.00	0.1324
48	15	0.4	37.50	0.0752
49	10	0.2	50.00	0.1156
50	15	0.2	75.00	0.1135

A.2. Hit/Miss Data from Different Data Processings for the Inspection of a CFRP Specimen (Chapter 4)

n	ascpt-ratio	raw image	DAC	PPT	1st D TSR	WT	PCT
1	1.67	0	0	0	0	0	0
2	1.88	0	0	0	0	0	0
3	2.14	0	0	0	0	0	0
4	2.5	0	0	0	0	1	0
5	2.78	0	0	0	0	0	0
6	3	0	0	0	1	0	0
7	3	0	0	0	1	0	1
8	3.13	0	0	0	0	0	0
9	3.57	0	0	0	1	1	1
10	3.75	0	0	1	1	0	1
11	3.89	0	0	0	0	0	0
12	4.17	0	0	1	1	1	1
13	4.38	0	0	0	0	0	0
14	5	0	0	1	1	1	1
15	5	0	1	1	1	1	1
16	5	0	0	1	1	1	1
17	5	0	1	1	1	1	1
18	5.56	0	0	0	0	0	0
19	5.83	0	1	1	1	1	1
20	6.25	1	1	1	1	1	1
21	6.25	0	0	0	1	0	1

22	7	0	1	1	1	1	1
23	7	0	1	1	1	1	1
24	7.14	0	1	1	1	1	1
25	7.5	0	1	1	1	1	1
26	8.33	0	1	1	1	1	1
27	8.33	1	1	1	1	1	1
28	8.33	0	0	0	0	0	0
29	8.75	1	1	1	1	1	1
30	9.38	0	0	1	1	0	1
31	10	0	1	1	1	1	1
32	10	1	1	1	1	1	1
33	10.71	0	0	1	1	1	1
34	11.67	1	1	1	1	1	1
35	12.5	1	1	1	1	1	1
36	12.5	1	1	1	1	1	1
37	12.5	0	1	1	1	1	1
38	15	1	1	1	1	1	1
39	15	0	1	1	1	1	1
40	15	1	1	1	1	1	1
41	16.67	1	1	1	1	1	1
42	17.5	1	1	1	1	1	1
43	18.75	1	1	1	1	1	1
44	25	1	1	1	1	1	1
45	25	1	1	1	1	1	1
46	25	1	1	1	1	1	1
47	35	1	1	1	1	1	1
48	37.5	1	1	1	1	1	1
49	50	1	1	1	1	1	1
50	75	1	1	1	1	1	1

A.3. Hit/Miss Data from LT and PT Inspection of a Set of Aluminum Foam Material (Chapter 5)

n	diameter (mm)	depth (mm)	aspect-ratio	lock_in	PT:RAW	PT:PPT	PT:1st D TSR	PT:PCT
1	6	6	1.00	0	0	0	0	0
2	6	5	1.20	0	0	0	0	0
3	8	6	1.33	0	0	0	0	0
4	6	4	1.50	0	0	0	0	0
5	8	5	1.60	0	0	0	0	0
6	10	6	1.67	0	0	0	0	0

7	10	5	2.00	0	0	0	0	0
8	12	6	2.00	0	0	0	0	0
9	8	4	2.00	0	0	0	0	0
10	6	3	2.00	0	0	0	0	0
11	12	5	2.40	0	0	0	0	0
12	10	4	2.50	0	0	0	0	0
13	15	6	2.50	0	0	0	0	0
14	8	3	2.67	0	0	0	0	0
15	12	4	3.00	0	0	0	0	0
16	15	5	3.00	0	0	0	1	0
17	18	6	3.00	0	0	0	0	0
18	6	2	3.00	0	0	0	0	0
19	10	3	3.33	1	0	0	0	0
20	20	6	3.33	0	0	0	1	1
21	18	5	3.60	1	0	0	1	0
22	22	6	3.67	0	0	0	0	0
23	15	4	3.75	0	0	0	0	0
24	12	3	4.00	1	1	1	1	1
25	20	5	4.00	1	1	1	1	1
26	8	2	4.00	0	0	0	0	0
27	25	6	4.17	0	1	1	1	1
28	22	5	4.40	1	1	1	1	1
29	18	4	4.50	0	1	1	1	1
30	27	6	4.50	0	1	1	1	1
31	10	2	5.00	1	0	1	1	0
32	15	3	5.00	1	0	0	1	0
33	20	4	5.00	1	1	1	1	1
34	25	5	5.00	1	1	1	1	1
35	30	6	5.00	1	1	1	1	1
36	32	6	5.33	1	1	1	1	1
37	27	5	5.40	1	1	1	1	1
38	22	4	5.50	1	1	1	1	1
39	12	2	6.00	1	0	0	1	1
40	18	3	6.00	1	1	1	1	1
41	30	5	6.00	1	1	1	1	1
42	6	1	6.00	0	0	0	0	0
43	25	4	6.25	1	1	1	1	1
44	32	5	6.40	1	1	1	1	1
45	20	3	6.67	1	0	0	1	0
46	27	4	6.75	1	1	1	1	1
47	22	3	7.33	1	1	1	1	1

48	15	2	7.50	1	0	1	1	0
49	30	4	7.50	1	1	1	1	1
50	32	4	8.00	1	1	1	1	1
51	8	1	8.00	1	1	1	1	1
52	25	3	8.33	1	1	1	1	1
53	18	2	9.00	1	1	1	1	1
54	27	3	9.00	1	1	1	1	1
55	10	1	10.00	1	0	1	1	1
56	20	2	10.00	1	0	1	1	1
57	30	3	10.00	1	1	1	1	1
58	32	3	10.67	1	1	1	1	1
59	22	2	11.00	1	1	1	1	1
60	12	1	12.00	1	1	1	1	1
61	25	2	12.50	1	1	1	1	1
62	27	2	13.50	1	1	1	1	1
63	15	1	15.00	1	1	1	1	1
64	30	2	15.00	1	1	1	1	1
65	32	2	16.00	1	1	1	1	1
66	18	1	18.00	1	1	1	1	1
67	20	1	20.00	1	1	1	1	1
68	22	1	22.00	1	1	1	1	1
69	25	1	25.00	1	1	1	1	1
70	27	1	27.00	1	1	1	1	1
71	30	1	30.00	1	1	1	1	1
72	32	1	32.00	1	1	1	1	1

A.4. Hit/Miss Data from UT and PPT Inspection for Impact Damage of CFRP (Chapter 6)

n	size (mm)	PPT	UT		n	size	PPT	UT
1	0.10	0	0		**59**	4.20	0	1
2	0.20	0	0		**60**	4.24	1	1
3	0.30	0	0		**61**	4.28	1	1
4	0.40	0	0		**62**	4.29	1	0
5	0.50	0	0		**63**	4.38	1	1
6	0.60	0	0		**64**	4.44	1	1
7	0.80	0	0		**65**	4.44	1	1
8	1.20	0	0		**66**	4.62	0	1
9	1.30	0	1		**67**	4.80	1	1
10	1.40	0	0		**68**	4.98	1	0

11	1.70	1	1	**69**	5.13	1	0
12	2.09	1	0	**70**	5.22	1	1
13	2.11	0	1	**71**	5.42	1	0
14	2.22	0	1	**72**	5.57	0	1
15	2.22	0	1	**73**	6.16	1	0
16	2.27	0	1	**74**	6.20	1	0
17	2.31	1	0	**75**	6.63	1	1
18	2.33	0	1	**76**	6.74	0	1
19	2.36	1	0	**77**	7.50	1	1
20	2.39	1	1	**78**	7.59	1	0
21	2.40	0	1	**79**	7.92	1	1
22	2.40	1	0	**80**	7.95	1	1
23	2.42	0	1	**81**	8.30	1	1
24	2.51	0	1	**82**	9.88	1	0
25	2.54	1	0	**83**	9.94	1	1
26	2.66	0	1	**84**	10.00	1	1
27	2.69	0	1	**85**	10.18	1	1
28	2.71	1	0	**86**	10.20	1	1
29	2.73	0	1	**87**	10.44	1	1
30	2.79	0	1	**88**	10.51	1	1
31	2.80	1	0	**89**	10.54	1	1
32	2.87	1	0	**90**	10.70	1	1
33	2.96	1	0	**91**	10.79	1	1
34	3.02	0	1	**92**	10.96	1	1
35	3.03	0	1	**93**	11.04	1	1
36	3.10	0	1	**94**	11.10	1	1
37	3.10	1	0	**95**	11.26	1	1
38	3.11	1	0	**96**	11.43	1	0
39	3.18	0	1	**97**	11.75	1	1
40	3.20	0	1	**98**	12.09	0	1
41	3.20	1	1	**99**	12.15	1	1
42	3.22	1	1	**100**	12.25	1	1
43	3.24	0	1	**101**	13.20	1	1
44	3.31	0	1	**102**	14.12	1	1
45	3.33	1	0	**103**	16.15	1	1
46	3.33	0	1	**104**	17.00	1	1
47	3.36	1	1	**105**	19.00	1	1
48	3.36	1	0	**106**	21.00	1	1
49	3.37	1	0	**107**	22.00	1	1
50	3.37	0	1	**108**	22.00	1	1
51	3.48	1	0	**109**	22.00	1	1

52	3.50	1	0		**110**	22.00	1	1
53	3.52	0	1		**111**	23.00	1	1
54	3.55	0	1		**112**	23.00	1	1
55	3.64	1	0		**113**	23.00	1	1
56	3.77	1	0		**114**	23.00	1	1
57	3.94	0	1		**115**	25.00	1	1
58	3.97	1	0					

A.5. Hit/Miss Data Obtained from Automated Segmentation (Chapter 7)

n	aspect-ratio	Raw image	1st D TSR	DAC	PPT	WT	PCT
1	1.67	0	0	0	0	0	0
2	1.88	0	0	0	0	0	0
3	2.14	0	0	0	0	0	0
4	2.50	0	0	0	0	0	0
5	2.78	0	0	1	0	0	0
6	3.00	0	0	0	0	0	0
7	3.00	0	0	0	0	0	0
8	3.13	0	0	0	0	0	0
9	3.57	0	1	0	0	0	0
10	3.75	0	0	0	0	0	0
11	3.89	0	0	0	0	0	0
12	4.17	0	1	1	1	1	1
13	4.38	0	0	0	0	0	0
14	5.00	0	0	0	0	0	1
15	5.00	0	1	0	0	0	1
16	5.00	0	1	1	1	1	1
17	5.00	0	1	0	1	1	1
18	5.56	0	0	0	0	0	0
19	5.83	0	1	1	1	1	1
20	6.25	0	1	0	1	1	1
21	6.25	0	0	0	0	0	0
22	7.00	0	1	1	1	0	1
23	7.00	0	1	1	1	1	1
24	7.14	0	1	0	1	1	1
25	7.50	0	1	0	0	0	0
26	8.33	0	1	1	1	1	1
27	8.33	0	1	1	1	1	1

28	8.33	0	0	0	0	0	0
29	8.75	0	1	0	1	1	1
30	9.38	0	0	0	0	0	0
31	10.00	0	1	1	1	1	1
32	10.00	0	1	1	1	1	1
33	10.71	0	1	0	1	1	1
34	11.67	1	1	1	1	1	1
35	12.50	0	1	0	1	1	1
36	12.50	0	1	0	1	1	1
37	12.50	0	1	1	1	1	1
38	15.00	0	1	1	1	1	1
39	15.00	0	1	1	0	1	1
40	15.00	0	1	1	1	1	1
41	16.67	1	1	1	1	1	1
42	17.50	1	1	1	1	1	1
43	18.75	0	1	0	1	1	1
44	25.00	0	1	1	1	1	1
45	25.00	0	1	1	1	1	1
46	25.00	0	1	1	1	1	1
47	35.00	1	1	1	1	1	1
48	37.50	0	1	1	1	1	1
49	50.00	1	1	1	1	1	1
50	75.00	0	1	1	1	1	1

Appendix B. First page of the published papers issued in the thesis

B.1. ThermoPoD: A reliability study on active infrared thermography for the inspection of composite materials

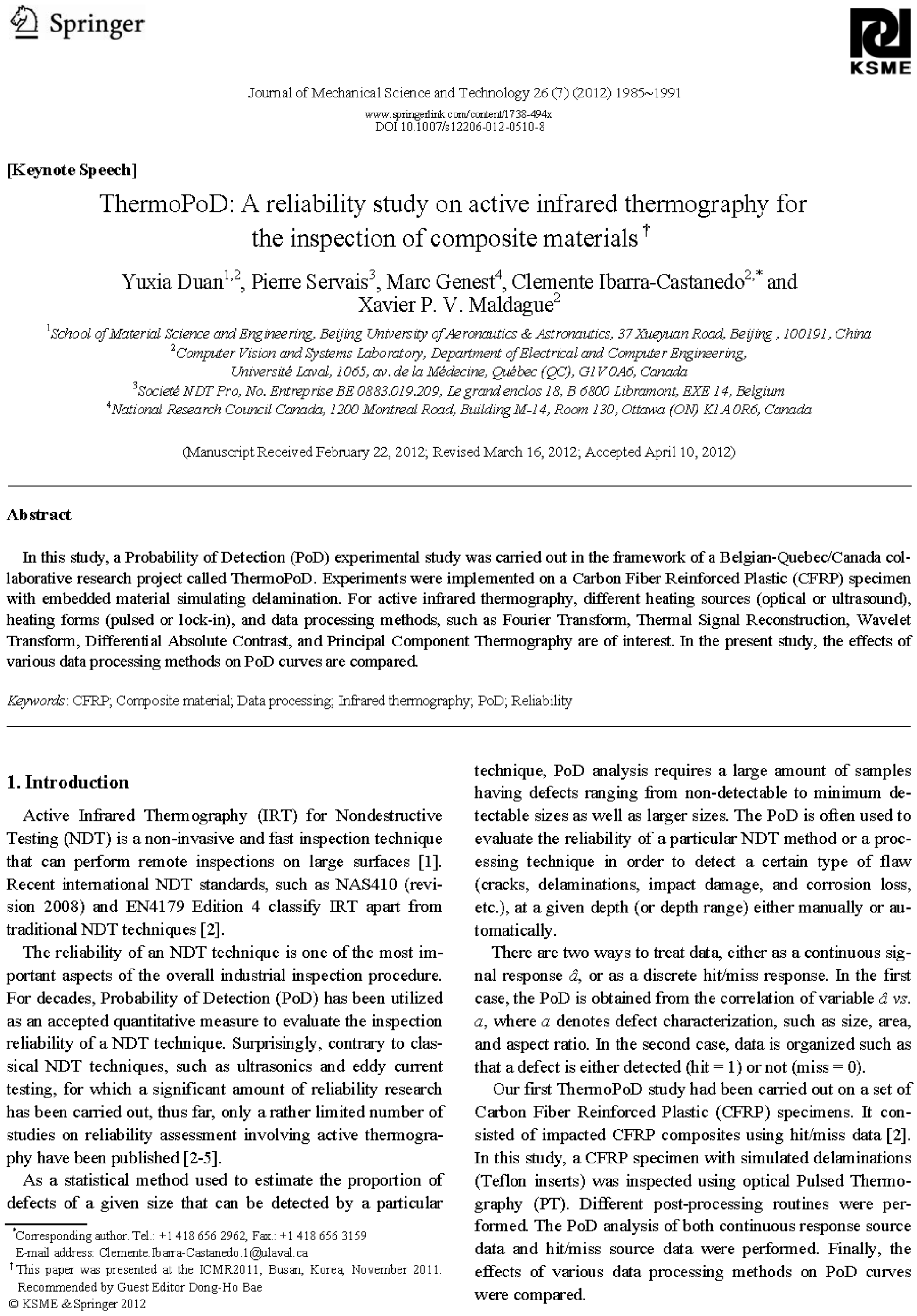

Journal of Mechanical Science and Technology 26 (7) (2012) 1985~1991
www.springerlink.com/content/1738-494x
DOI 10.1007/s12206-012-0510-8

[Keynote Speech]

ThermoPoD: A reliability study on active infrared thermography for the inspection of composite materials †

Yuxia Duan[1,2], Pierre Servais[3], Marc Genest[4], Clemente Ibarra-Castanedo[2,*] and Xavier P. V. Maldague[2]

[1] *School of Material Science and Engineering, Beijing University of Aeronautics & Astronautics, 37 Xueyuan Road, Beijing , 100191, China*
[2] *Computer Vision and Systems Laboratory, Department of Electrical and Computer Engineering, Université Laval, 1065, av. de la Médecine, Québec (QC), G1V 0A6, Canada*
[3] *Societé NDT Pro, No. Entreprise BE 0883.019.209, Le grand enclos 18, B 6800 Libramont, EXE 14, Belgium*
[4] *National Research Council Canada, 1200 Montreal Road, Building M-14, Room 130, Ottawa (ON) K1A 0R6, Canada*

(Manuscript Received February 22, 2012; Revised March 16, 2012; Accepted April 10, 2012)

Abstract

In this study, a Probability of Detection (PoD) experimental study was carried out in the framework of a Belgian-Quebec/Canada collaborative research project called ThermoPoD. Experiments were implemented on a Carbon Fiber Reinforced Plastic (CFRP) specimen with embedded material simulating delamination. For active infrared thermography, different heating sources (optical or ultrasound), heating forms (pulsed or lock-in), and data processing methods, such as Fourier Transform, Thermal Signal Reconstruction, Wavelet Transform, Differential Absolute Contrast, and Principal Component Thermography are of interest. In the present study, the effects of various data processing methods on PoD curves are compared.

Keywords: CFRP; Composite material; Data processing; Infrared thermography; PoD; Reliability

1. Introduction

Active Infrared Thermography (IRT) for Nondestructive Testing (NDT) is a non-invasive and fast inspection technique that can perform remote inspections on large surfaces [1]. Recent international NDT standards, such as NAS410 (revision 2008) and EN4179 Edition 4 classify IRT apart from traditional NDT techniques [2].

The reliability of an NDT technique is one of the most important aspects of the overall industrial inspection procedure. For decades, Probability of Detection (PoD) has been utilized as an accepted quantitative measure to evaluate the inspection reliability of a NDT technique. Surprisingly, contrary to classical NDT techniques, such as ultrasonics and eddy current testing, for which a significant amount of reliability research has been carried out, thus far, only a rather limited number of studies on reliability assessment involving active thermography have been published [2-5].

As a statistical method used to estimate the proportion of defects of a given size that can be detected by a particular technique, PoD analysis requires a large amount of samples having defects ranging from non-detectable to minimum detectable sizes as well as larger sizes. The PoD is often used to evaluate the reliability of a particular NDT method or a processing technique in order to detect a certain type of flaw (cracks, delaminations, impact damage, and corrosion loss, etc.), at a given depth (or depth range) either manually or automatically.

There are two ways to treat data, either as a continuous signal response $\hat{a}$, or as a discrete hit/miss response. In the first case, the PoD is obtained from the correlation of variable $\hat{a}$ *vs.* a, where a denotes defect characterization, such as size, area, and aspect ratio. In the second case, data is organized such as that a defect is either detected (hit = 1) or not (miss = 0).

Our first ThermoPoD study had been carried out on a set of Carbon Fiber Reinforced Plastic (CFRP) specimens. It consisted of impacted CFRP composites using hit/miss data [2]. In this study, a CFRP specimen with simulated delaminations (Teflon inserts) was inspected using optical Pulsed Thermography (PT). Different post-processing routines were performed. The PoD analysis of both continuous response source data and hit/miss source data were performed. Finally, the effects of various data processing methods on PoD curves were compared.

---

[*] Corresponding author. Tel.: +1 418 656 2962, Fax.: +1 418 656 3159
E-mail address: Clemente.Ibarra-Castanedo.1@ulaval.ca

[†] This paper was presented at the ICMR2011, Busan, Korea, November 2011. Recommended by Guest Editor Dong-Ho Bae

B.2. Quantitative evaluation of optical lock-in and pulsed thermography for aluminum foam material

Infrared Physics & Technology 60 (2013) 275–280

Contents lists available at SciVerse ScienceDirect

Infrared Physics & Technology

journal homepage: www.elsevier.com/locate/infrared

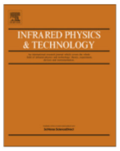

Quantitative evaluation of optical lock-in and pulsed thermography for aluminum foam material ☆

Yuxia Duan [a,b], Stefanie Huebner [c], Ulf Hassler [c], Ahmad Osman [c], Clemente Ibarra-Castanedo [b], Xavier P.V. Maldague [b,*]

[a] *School of Material Science and Engineering, Beijing University of Aeronautics & Astronautics, 37, Xueyuan Road, Beijing 100191, China*
[b] *Computer Vision and Systems Laboratory, Department of Electrical and Computer Engineering, Université Laval, 1065, av. de la Médecine, Québec, QC G1V 0A6, Canada*
[c] *Fraunhofer Development Center X-ray Technologies, A Cooperative Department of IZFP Saarbrücken and IIS Erlangen, 81, Dr-Mack-Street, Fürth 90762, Germany*

HIGHLIGHTS

- Probability of detection (POD) assessment.
- Pulsed and Lockin IRT approaches.
- Infrared thermographic image processing.
- Pulsed Phase Thermography (PPT).
- Thermographic Signal Reconstruction (TSR).

ARTICLE INFO

Article history:
Received 5 November 2012
Available online 10 June 2013

Keywords:
Lock-in
Pulsed
Thermography
Aluminum foam
PoD

ABSTRACT

In this article, quantitative evaluation of optical thermographic techniques relative to the non-destructive inspection of aluminum foam material is studied. For this purpose, a set of aluminum foam specimens with flat-bottom holes (FBH) was inspected by both optical lock-in thermography (LT) and pulsed thermography (PT). Probability of detection (PoD) analysis, as a quantitative method to estimate the capability and reliability of a particular inspection technique, was studied and compared for both optical LT and PT inspection results.

1. Introduction

Aluminum foam material combines the advantages of high strength and low weight. Structural efficiencies and relatively low cost makes this material of widespread use in aerospace, marine, and automotive structures [1]. Potential applications of such materials include sound and energy absorption appliances, cores for structural sandwich panels, and electromagnetic wave shields, among many others [2].

Non-destructive inspection (NDI) studies of aluminum foam material are rarely found in literature except from X-ray inspection [3,4]. The material has a low overall X-ray absorption because of the large amount of voids inside, which allows large specimens to be inspected by X-ray tomography. X-ray tomography has been proven to be a very powerful tool allowing characterizing the architecture or microstructure of cellular materials [4]. However, each NDI technique has its own strengths and weaknesses. Compared with X-ray tomography, the main advantages of optical excitation thermography are fast inspection rate, security (no harmful radiation involved) and single-side needed (stimulation and inspection on the same side) [5]. In this article, two classical optical thermographic techniques, including lock-in thermography (LT), also known as modulated thermography (MT), and pulsed thermography (PT) will be employed to inspect aluminum foam material.

Abbreviations: LT, lock-in thermography; PT, pulsed thermography; FBH, flat-bottom holes; PoD, probability of detection; NDI, non-destructive inspection; MT, modulated thermography; PPT, pulsed phase thermography; TSR, thermal signal reconstruction; PCT, principle component thermography; SVD, singular value decomposition; EOFs, empirical orthogonal functions; PCs, principal components.

* Corresponding author. Tel.: +1 418 656 2962; fax: +1 418 656 3594.
E-mail address: maldagx@gel.ulaval.ca (X.P.V. Maldague).

1350-4495/$ - see front matter © 2013 The Authors. Published by Elsevier B.V. All rights reserved.
http://dx.doi.org/10.1016/j.infrared.2013.05.009